LiftWEC

DEVELOPMENT OF A NEW CLASS OF WAVE ENERGY CONVERTER BASED ON HYDRODYNAMIC LIFT FORCES

Deliverable D3.3

Tool validation and extension

Deliverable Lead	Hamburg University of Technology
Delivery Date	18th January 2022
Dissemination Level	Public
Status	Final
Version	1.5

This project has received funding from the European Union's Horizon 2020 research and innovation programme under grant agreement No 851885. This output reflects the views only of the author(s), and the European Union cannot be held responsible for any use which may be made of the information contained therein.

Document Information

Project Acronym	LiftWEC
Project Title	Development of a new class of wave energy converter based on hydrodynamic lift forces
Grant Agreement Number	851885
Work Package	WP3
Related Task(s)	T3.2
Deliverable Number	D3.3
Deliverable Name	Tool validation and extension report
Due Date	31/05/2021
Date Delivered	17/01/2022
Primary Author(s)	Gerrit Olbert (TUHH)
Co-Author(s)	Louis Papillon (INN), Remy Pascal (INN), Andrei Ermakov (NUIM), Florent Thibaut (ECN)
Document Number	LW-D03-03

Version Control

Revision	Date	Description	Prepared By	Checked By
1.0	04/01/2022	Internal draft for comment	GO	MF
1.2	07/01/2022	Internal draft for comment	GO	FT
1.3+1.4	14/01/2022	Internal draft for comment	GO	RP
1.5	17/02/2022	Release for EU approval	GO	RP

EXECUTIVE SUMMARY

This document presents the results of a validation study of numerical tools used for hydrodynamic modelling of a cyclorotor-type wave energy converter in the scope of the LiftWEC project. The numerical tools assessed here consists of a high-fidelity tool, based on the Reynolds-Averaged Navier-Stokes (RANS) equation, and a 'global' model, based on linear potential flow theory.

According to their level of fidelity and corresponding computational effort, these tools are used for various purposes within the project, such as foil design and investigation of separation phenomena, as well as structural design and assessment of annual energy production (AEP).

Before these tools are applied to their respective purposes, a validation study is conducted to assess the associated level of uncertainty and potentially propose mitigation strategies. For this purpose a series of experimental model tests has been conducted in a quasi-two-dimensional setting in the wave flume of École Centrale de Nantes (ECN). Several of the model test scenarios are replicated numerically and results compared to experimental measurements.

In the first section of this document, a short introduction into the background of the LiftWEC project is given. The principle of lift-based wave energy conversion is explained and references for further reading are provided. In section 2, the fundamental theories which form the basis of the two employed hydrodynamic solvers are explained. This serves to provide an understanding of the source of potential modelling and discretization errors, which are discussed later in the document.

A description of the experimental model tests is given in section 3. Since more detailed descriptions were provided in corresponding reports written by those project partners conducting the experimental reports, only a fundamental overview on test setup and calibration is provided. References to the mentioned reports can be found in this section.

The global model, owing to simplicity, relies on a set of empirically defined coefficients which approximate the behaviour of the WEC hydrofoils in different inflow conditions. A procedure to derive these coefficients from reference data was specifically designed for this study and is presented, including a validation of the method, in section 4. In the subsequent part of this report, section 5, the model is then applied to replicate the physical tests and numerical results obtained for rotor operation in regular waves is compared to experimental measurements. The results indicate that the model is able to reproduce mean forces with relatively good accuracy for most cases. However, when comparing time series showing force fluctuations on a wave-by-wave basis, significant differences are found which require further investigation.

In section 6, a comparison of RANS-based results and experimental force measurements is presented for single and double-foil rotor operation in calm water and in regular waves. Radial and tangential forces are compared in form of time series, mean forces and fundamental amplitudes. Mean forces and fundamental amplitudes in most wave conditions are generally well met, although several exceptions are found. Due to the occurrence of considerable wave reflections in the experiment, it is unclear whether this reduced reliability is to be assigned to the numerical model or the available reference data. A comparison of force signals time series shows strong and high-frequent fluctuations in both experiment and simulation. Apart from reflections, this is likely due to the formation of vortices in the foil wake due to fluctuation of inflow velocity vector. When passing through or in vicinity of

This project has received funding from the European Union's Horizon 2020 research and innovation programme under grant agreement No 851885. This output reflects the views only of the author(s), and the European Union cannot be held responsible for any use which may be made of the information contained therein.

vortices, foil circulation shows strong fluctuation, while tangential forces remain largely unaffected for small angles of attack.

Finally, a set of conclusions regarding further improvements and consideration of global model and high-fidelity model is presented in section 7. These are extended by several observations made and recommendations drafted while analysing the experimental data, which might help to improve the quality of a 3D model test series on the LiftWEC concept, which is currently scheduled for late spring of 2022.

This project has received funding from the European Union's Horizon 2020 research and innovation programme under grant agreement No 851885. This output reflects the views only of the author(s), and the European Union cannot be held responsible for any use which may be made of the information contained therein.

TABLE OF CONTENTS

This project has received funding from the European Union's Horizon 2020 research and innovation programme under grant agreement No 851885. This output reflects the views only of the author(s), and the European Union cannot be held responsible for any use which may be made of the information contained therein.

This project has received funding from the European Union's Horizon 2020 research and innovation programme under grant agreement No 851885. This output reflects the views only of the author(s), and the European Union cannot be held responsible for any use which may be made of the information contained therein.

1 INTRODUCTION

This document constitutes Deliverable ‘D3.3 Tool Validation and Extension’ of the LiftWEC project. LiftWEC is a collaborative research project funded by the European Union’s Horizon 2020 Research and Innovation Programme under Grant Agreement No 851885.

1.1 PROJECT OUTLINE

The LiftWEC project focuses on the development of a novel type of Wave Energy Converter (WEC), called LiftWEC, which is intended to utilise hydrodynamic lift forces to incite device motion and extract wave energy using a rotating hydrofoil, as opposed to the more traditional approach of exploiting buoyancy and diffraction force regimes. This radically different approach to the design of wave energy converters offers the opportunity of making a step-change in the potential of wave energy, and thus lead the way for its commercialisation, where no commercially viable wave energy system currently exists.

1.2 PURPOSE OF DELIVERABLE

The installation and operation of an offshore device such as a wave energy converter is generally associated with high cost, due to the extreme environment in which these devices are installed. Therefore, the benefit of each installation should be determined to a high degree of certainty before engaging in any offshore activities. In the case of marine renewable energies, such as offshore wind, offshore solar and wave energy, advanced cost models exist. Using these, the cost incurred during a device life-time may be assessed to comparatively high degrees of certainty.

This cost should be exceeded by the price of energy generated by the energy devices. An estimation of the life-time generated energy can for example be drawn from previous installations in similar locations. This approach is restricted to field of energy generation with decades of experience, such as wind energy. Whenever a new technological advancement is introduced, this bears a certain amount of uncertainty, which has to be quantified in terms of impact on cost and energy produced. This can be done using either scaled model prototypes or using numerical models, which replicate the behaviour of devices in certain conditions in order to assess device performance, loads on the structure and the sensitivity of these quantities to variations in environmental conditions, such as wind, waves and currents.

Nowadays, due to the high cost of experimental modelling and the increased availability of computational power, numerical models are widely used for these purposes. In the case of wave energy, different types of numerical models exist, which assess the behaviour of wave energy devices at different levels of detail and different levels of reliability.

Computer-based hydrodynamic modelling of a body exposed to certain flow conditions is typically based on the concept of conservation of mass, momentum and energy. These principles, along with certain boundary conditions, are converted into equation systems which can be solved in order to determine certain quantities of the flow such as pressure and velocity. Herein, the result produced by the numerical model is likely to deviate from the real, physical quantity, due to certain errors introduced when representing the typically complex physical device with a set of equations.

Therefore, in order to obtain an understanding about the reliability of the numerical models when applying them for design purposes, a validation study shall be conducted. This study is based on an experimental test series, in which a cyclorotor device was operated in a range of conditions, while motion, forces and environment were monitored.

These settings are then replicated using the numerical models used in the scope of the LiftWEC project. A comparison of the measured quantities is then conducted in order to assess differences between numerical models and the experimental measurements.

1.3 STRUCTURE OF THE DOCUMENT

In the first section of this report, central elements of the theoretical background of the two numerical models validated in this study will be presented. Then, a brief overview of the design of the experimental test campaign will be given. In the subsequent section, the core hypothesis of the global model will be discussed and validated. Sections 4 and 5 present the results of the validation studies of global model and CFD model. In the last section of this report, a conclusion regarding the applicability of the numerical methods will be drawn and areas of future research will be highlighted.

2 THEORETICAL BACKGROUND OF NUMERICAL MODELS

A distinction will be made between two main classes of numerical models. The first class is based on potential flow theory, which is often employed for the design of Wave Energy Converters and lifting bodies due to the low computational resources required. The second is a field method-type approach, based on the RANS equation. This latter approach is computationally much more expensive but allows to directly consider the entire flow field characteristics including viscous boundary layers and turbulent effects at a potentially lower modelling error.

Both numerical approaches have advantages and disadvantages regarding the computational resources required and the obtainable accuracy. In order to allow an analysis of the comparison between numerical results and experimental references presented in this report, the theoretical background and the introduced modelling assumptions of both approaches shall be presented in the following sections.

2.1 GLOBAL MODEL

The so-called LiftWEC global model is implemented within the OrcaFlex numerical framework. The model is an evolution of the “demonstrator” model described in D3.1. Since this document, it has been decided to focus on the development of the demonstrator as the main model in order to benefit from the flexibility of the OrcaFlex framework to model the different types of support structures and moorings.

The objective of the global model is to model the global loads on the entire system in order to provide design inputs for the concepts, and potentially to get performance estimates of the concept in realistic conditions (irregular directional sea states). The model is composed of a rotor (shaft + hydrofoils + hydrofoil supports), a support structure, which depends on the configuration chosen, and moorings if the structure is floating (see Figure 1). Every part of the LiftWEC system is modelled using an appropriate theory.

This project has received funding from the European Union’s Horizon 2020 research and innovation programme under grant agreement No 851885. This output reflects the views only of the author(s), and the European Union cannot be held responsible for any use which may be made of the information contained therein.

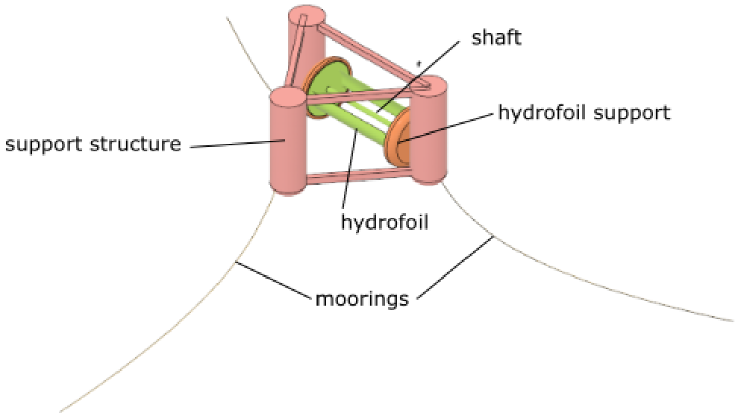

Figure 1: LiftWEC semi-sub configuration

The hydrodynamics loads on the hydrofoils are computed using the thin foil potential flow theory described in 2.1.3.1 and 2.1.3.1. The loads on the hydrofoil supports are computed similarly to hydrofoils but considering the drag effects only (the lift effects are not considered).

The hydrodynamics loads on the rotor shaft are computed through an analytical model in the potential flow theory framework (described in 2.1.3.2) or the Morison equation (described in 2.1.2), depending on whether the loads are mainly due to diffraction or viscous effects, respectively.

The hydrodynamic loads on the support structure are modelled directly within OrcaFlex, using the linear potential flow theory (described in 2.1.1.2) or the Morison equation (described in 2.1.2), depending on whether the loads are mainly due to diffraction or viscous effects, respectively.

The predominance of diffraction or viscous effects on a structure subjected to waves can be determined by computing the Keulegan-Carpenter number K_C,

$$K_C = \frac{V_o T_o}{L_b} \tag{1}$$

where V_o is the amplitude of the flow velocity oscillation, T_o is the period of the oscillation, and L_b is the characteristic length of the body, the diameter in the case of a cylinder. For K_C smaller than 5, it is assumed that diffraction effects are predominant, whereas viscous effects are considered significant for K_C greater than 5 (Molin, 2002).

The rotor, which includes the foils, the foil supports, and the rotor central axis (shaft) is modelled through an external function coded in python and added to the OrcaFlex model. The support structure and the mooring system are modelled in OrcaFlex for the relevant concepts.

The dynamics of the entire system is calculated by OrcaFlex, by integrating the loads on the support structure, the mooring loads, and the loads from the rotor. The following sections provide a theoretical background to the global model.

2.1.1 Potential flow theory

2.1.1.1 General equations

We consider the fixed right-handed coordinate system $(\boldsymbol{x}, \boldsymbol{y}, \boldsymbol{z})$, with positive z vertically upwards through the centre of gravity of the body and the origin in the plane of the undisturbed free surface. The displacements at the centre of gravity of the body in the x-, y-, and z-directions, with respect to the origin are x_G, y_G and z_G, respectively, so that x_G is surge, y_G is sway and z_G is the heave displacement. Let the angular displacements at the centre of gravity of the body of the rotational motion about the x-, y-, and z-axes be α_r, β_r, γ_r. Hence, to express the generalized body motion vector $\vec{\mathrm{X}}(\mathrm{t})$, we denote

$$\vec{X}(t) = \begin{vmatrix} x_G \\ y_G \\ z_G \\ \alpha_r \\ \beta_r \\ \gamma_r \end{vmatrix} \tag{2}$$

The assumptions of an incompressible, inviscid fluid and irrotational flow lead to a set of equations for potential flow theory, which, for a velocity potential ϕ and a free surface elevation η, leads to

- the Laplace equation in the entire fluid domain (D)

$$\Delta \phi = 0 \tag{3}$$

- a kinematic free-surface boundary condition (no material flux across the free-surface) (on $z = \eta$)

$$\frac{\partial \eta}{\partial t} - \frac{\partial \phi}{\partial z} + \vec{\nabla}\phi . \vec{\nabla}\eta = 0 \tag{4}$$

- a dynamic free-surface boundary condition (Euler's integral, pressure on the free-surface elevation equal to the atmospheric pressure, where P_{atm}= 0 without loss in generality) (on $z = \eta$)

$$g\eta + \frac{\partial \phi}{\partial t} + \frac{1}{2}\left|\vec{\nabla}\phi\right|^2 = 0 \tag{5}$$

- an impermeability condition on the seabed, with a unit normal vector to the surface n

$$\frac{\partial \phi}{\partial n} = 0 \tag{6}$$

- a body boundary condition (impermeability condition) for a body moving at a speed $\vec{V}$, with a normal $\vec{n}$

$$\frac{\partial \phi}{\partial n}(M, t) = \vec{V}.\vec{n}(M, t) \tag{7}$$

This project has received funding from the European Union's Horizon 2020 research and innovation programme under grant agreement No 851885. This output reflects the views only of the author(s), and the European Union cannot be held responsible for any use which may be made of the information contained therein.

- a radiation condition, where the perturbed potential ϕ_p tends to 0 moving away from the body, the total potential ϕ is equal to the sum of an incident potential ϕ_0 and a perturbed potential ϕ_p

$$\phi = \phi_0 + \phi_p \tag{8}$$

with Δ the Laplace operator, ∇ the gradient operator, ∂ the partial operator, g the acceleration due to gravity, and M any point in the fluid domain.

Assuming incompressible and inviscid fluid, the governing Navier–Stokes equations evolve into Euler's equation. Progressively applying the assumption of irrotational flow leads to Euler's integral, giving access, knowing the velocity potential, to the pressure p:

$$p = -\rho g z - \rho \frac{\partial \phi}{\partial t} - \frac{1}{2}\rho \left|\vec{\nabla}\phi\right|^2 \tag{9}$$

where ρ is the water density. The integration of the pressure gives the resulting hydrodynamic and hydrostatic forces (and moments) F_{hydro} acting on a surface (S) of normal $\vec{n}$

$$\overrightarrow{F_{hydro}} = -\iint_S p\vec{n}\, ds \tag{10}$$

with the generalized normal vector $\vec{n}$

$$\vec{n} = \begin{vmatrix} n_1 \\ n_2 \\ n_3 \\ \boldsymbol{y}n_3 - \boldsymbol{z}n_2 \\ \boldsymbol{z}n_1 - \boldsymbol{x}n_3 \\ \boldsymbol{x}n_2 - \boldsymbol{y}n_1 \end{vmatrix} \tag{11}$$

Thus, applying Newton's second law, the equations of motion for a floating body can be expressed as

$$M\ddot{\vec{X}} = \overrightarrow{F_{hydro}} - \overrightarrow{\mathrm{F_g}} + \overrightarrow{F_{ext}} \tag{12}$$

With

$$F_{g3} = \boldsymbol{m}g \tag{13}$$

with $\boldsymbol{m}$ the mass of the body, M its mass matrix, g the gravity, $\overrightarrow{F_{ext}}$ represents additional forces (due to mooring, PTO, lift/drag...).

This project has received funding from the European Union's Horizon 2020 research and innovation programme under grant agreement No 851885. This output reflects the views only of the author(s), and the European Union cannot be held responsible for any use which may be made of the information contained therein.

2.1.1.2 Linear potential flow theory

Under the assumption of small wave steepness and small body motion amplitudes, the set of equations can be simplified, and the potential ϕ can be divided into an incident ϕ_0, diffracted ϕ_D and radiated ϕ_R potential

$$\phi = \phi_0 + \phi_D + \phi_R \tag{14}$$

The incident and diffraction potentials correspond, respectively, to the potential created by the incident wave and the resulting wave, when the body is considered fixed. The radiation potential corresponds to the waves created by the motion of the body itself in the absence of the incoming waves. The linearized kinematic and dynamic free surface boundary condition lead to

$$\frac{\partial^2 \phi}{\partial t^2} + g\frac{\partial \phi}{\partial z} = 0 \tag{15}$$

The body boundary condition can be written as

$$\frac{\partial \phi_{Ri}}{\partial n_i} = \sum_{i=1}^{6} n_i \tag{16}$$

$$\frac{\partial \phi_D}{\partial n} = -\frac{\partial \phi_0}{\partial n} \tag{17}$$

The hydrodynamic forces on a body are expressed as

$$\overrightarrow{\mathrm{F_{hydro}}} = \overrightarrow{\mathrm{F_S}} + \overrightarrow{\mathrm{F_{ex}}} + \overrightarrow{\mathrm{F_R}} \tag{18}$$

With

$$\overrightarrow{\mathrm{F_S}} = \iint_{\mathrm{S}} \rho g z \vec{n}\, \mathrm{ds} = \mathrm{K}\vec{\mathrm{X}} \tag{19}$$

$$\vec{\mathrm{F}}_{\mathrm{ex}} = \iint_{\mathrm{S}} \rho \left(\frac{\partial \phi_0}{\partial \mathrm{t}} + \frac{\partial \phi_{\mathrm{D}}}{\partial \mathrm{t}} \right) \vec{\mathrm{n}}\mathrm{ds} \tag{20}$$

where F_S is the hydrostatic force, K the hydrostatic matric, F_{ex} is the excitation force, itself divided into a Froude-Krylov force F_{FK}, which is the force exerted by the pressure of the incident wave, and a diffraction force F_D. F_R is the radiation force, expressed by an added mass term μ, and a radiation damping term λ

$$\overrightarrow{\mathrm{F_R}} = -\mu\ddot{\vec{\mathrm{X}}} - \lambda\dot{\vec{\mathrm{X}}} \tag{21}$$

In the frequency domain, the equation of motion becomes then:

$$\mathrm{F_{ex}} = [-\omega^2(\mathrm{M}+\mu) \mp i\omega\lambda + \mathrm{K}]\mathrm{X} + \mathrm{F_g} + \mathrm{F_{ext}} \tag{22}$$

2.1.2 Morison equation

Morison equation has been formulated by (Morison, Johnson, & Schaaf, 1950) to estimate the wave loads acting on a structure at high Keulegan-Carpenter numbers, i.e. when the characteristic length of the body (the diameter for a cylinder) is much smaller compared to the wavelength. The hydrodynamic loads $\overrightarrow{F_M}$ given by the Morison equation can be written

$$\overrightarrow{\mathrm{F_M}} = \mathrm{V_f}(\overrightarrow{\mathrm{a_f}} + \mathrm{C_a}\overrightarrow{\mathrm{a_r}}) + \frac{1}{2}\rho\mathrm{C_d}\mathrm{A}\mid \mathrm{v_r} \mid \vec{\mathrm{v}}_\mathrm{r} \tag{23}$$

$$\overrightarrow{\mathrm{a_r}} = \overrightarrow{\mathrm{a_f}} - \overrightarrow{\mathrm{a_b}} \tag{24}$$

where V_f is the mass of fluid displaced by the body, $\overrightarrow{a_f}$ is the fluid acceleration, C_a is the added mass coefficient of the body, $\overrightarrow{a_r}$ the fluid acceleration relative to the body, $\overrightarrow{a_r}$ is the body acceleration, ρ is the water density, A is the drag area, and $\overrightarrow{v_r}$ is the fluid velocity relative to the body. The first term is the inertia part of the hydrodynamic loads, the second term is related to the drag force.

The added mass coefficient can also be written as an inertia coefficient C_m, as followed

$$\mathrm{C_m} = 1 + \mathrm{C_a} \tag{25}$$

The added mass and drag coefficients are determined empirically. Axial and normal C_a and C_d of cylinders are computed using formulas from (DNVGL, 2017), detailed in Section 6.7 and 6.9 of the document, respectively.

2.1.3 Model

The global model aims at estimating the loads acting on the foils, the foil supports, the rotor shaft, the support structure, and the possible mooring lines of the LiftWEC concept. At the current stage of the project, only the foils, foil supports, and the rotor shaft are implemented and validated in the global model.

2.1.3.1 Foils

Foils modelling uses the thin airfoil theory, based on the potential flow theory, adding the following assumptions

- the potential flow is bidimensional
- the foil is thin (thickness/length<0.1, camber<5%)

When a foil is surrounded by a moving fluid, two hydrodynamic forces act on the foil, a lift force, perpendicular to the relative inflow fluid velocity, and a drag force, in the same direction as inflow, respectively F_L and F_D, defined by

This project has received funding from the European Union's Horizon 2020 research and innovation programme under grant agreement No 851885. This output reflects the views only of the author(s), and the European Union cannot be held responsible for any use which may be made of the information contained therein.

$$F_L = \frac{1}{2}\rho w^2 S C_L \tag{26}$$

$$F_D = \frac{1}{2}\rho w^2 S C_D \tag{27}$$

with ρ the density of the fluid, w the relative fluid velocity, S the projected foil surface area, C_L and C_D the lift and drag coefficients. The relative fluid velocity is the result of the foil velocity u and the fluid velocity v.

$$\vec{w} = \vec{u} + \vec{v} \tag{28}$$

For the tank test 2D experiments, foil profiles of constant chord are used. Hence, the projected foil surface area can be expressed as the foil spanwise length l multiplied by the chord c.

$$S = l.c \tag{29}$$

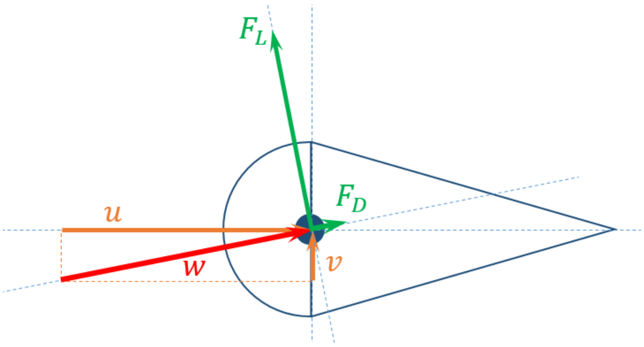

Figure 2: Velocity and force components on a foil

The C_L and C_D coefficients depend on the angle between the relative fluid velocity and the foil chord, called angle of attack (AoA). The foil profile used for the 2D tank tests experiments is a NACA0015. Lift and drag coefficients have previously been measured experimentally by (Sheldahl & Klimas, 1981), however, it has been found during post-processing of tank tests data that C_L and C_D did not match tank test results. Therefore, the corrected C_L and $C_D$have been estimated from the test experiments. The correction process is described in Section 4.1.

Hydrodynamic loads on the foil and the angle of attack are computed at the hydrodynamic centre of the foil, located at ¼ chord length, measured from the leading edge. Several investigations of basic foil hydrodynamics have shown that the centre of circulation induced by a hydrofoil can be approximated using this location. The validation process of hydrodynamic loads estimation on the foil for the global model are presented in Section 5.1.

This project has received funding from the European Union's Horizon 2020 research and innovation programme under grant agreement No 851885. This output reflects the views only of the author(s), and the European Union cannot be held responsible for any use which may be made of the information contained therein.

2.1.3.2 Rotor shaft

2.1.3.2.1 Potential flow theory

(Ogilvie, 1963) studied the 2D behaviour of a horizontal cylinder beneath a free surface subject to waves within linear potential flow framework detailed in Section 2.1.1.2. Ogilvie computed analytically the linear first and second-order forces acting on a fixed cylinder, cylinder undergoing prescribed motion, and free-floating cylinder. Due to the free surface, the cylinder behaviour greatly changes depending on its submergence and radius. Hydrodynamic loads on the rotor shaft are computed based on Ogilvie's works. The validation process of hydrodynamic loads estimation on the rotor shaft for the global model are presented in Section 5.2.

The hydrodynamic parameters are saved into a WAMIT format and the hydrodynamic database (excitation force magnitude and phase, drift force, added mass and radiation damping) is directly imported in OrcaFlex.

2.1.3.2.2 Morison equation

The hydrodynamic loads are composed of an inertia force and a drag force. The corresponding coefficients are computed using DNVGL-RP-C205.

2.1.3.3 Support structure

2.1.3.3.1 Potential flow theory

The hydrodynamic parameters of the structure are computed using the 3D BEM code OrcaWave. The hydrodynamic database (excitation force magnitude and phase, drift force, added mass and radiation damping) is then directly imported in OrcaFlex.

2.1.3.3.2 Morison equation

The hydrodynamic loads are composed of an inertia force and a drag force. The corresponding coefficients are computed using DNVGL-RP-C205.

This project has received funding from the European Union's Horizon 2020 research and innovation programme under grant agreement No 851885. This output reflects the views only of the author(s), and the European Union cannot be held responsible for any use which may be made of the information contained therein.

2.2 RANS METHOD

2.2.1 Principle of Conservation

The RANS method, similar to Potential Flow Theory, is also based on the principles of conservation of mass and momentum. These are expressed in the continuity equation:

$$\frac{\delta \rho}{\delta t}+\frac{\delta \rho \boldsymbol{u}}{\delta x}=0 \tag{30}$$

and in the Navier Stokes, or momentum equation:

$$\frac{\delta \rho \boldsymbol{u}}{\delta t}+\frac{\delta \rho \boldsymbol{u}\boldsymbol{u}}{\delta \boldsymbol{x}}=2\mu D-\frac{\delta p}{\delta \boldsymbol{x}}+f \tag{31}$$

With $D=\frac{1}{2}[\nabla \boldsymbol{u}+(\nabla \boldsymbol{u})^{\boldsymbol{T}}]$.

Equations (30) and (31) express that neither mass nor momentum can be created or destroyed in a continuous fluid. Assuming the fluid as incompressible with a constant density ρ, the remaining two unknowns contained in these equations are the velocity vector $\boldsymbol{u}$ and the pressure p.

2.2.2 Finite Volume Approach

In order to bring the differential equations (30) and (31) into a numerically solvable form, the investigated domain is divided into a finite number of control volumes V_C with respective control boundaries S_C. These volumes are also referred to as cells. The equations are brought into integral form for each cell, which is shown in equations (32) and (33) in the formulation for an incompressible fluid.

$$\rho \int_{S_C} \frac{\delta \boldsymbol{u}}{\delta \boldsymbol{x}} dS_C=0 \tag{32}$$

$$\rho \int_{V_C} \frac{\delta \boldsymbol{u}}{\delta t} dV_C+\rho \boldsymbol{u} \int_{S_C} \frac{\delta \boldsymbol{u}}{\delta \boldsymbol{x}} dS_C=\int_{S_C} 2\mu D\, dS_C-\int_{S_C} \frac{\delta p}{\delta \boldsymbol{x}} dS_C+\int_{V_C} f\, dV_C \tag{33}$$

As these partial differential equations cannot be solved explicitly, they are then transferred into linear form and solved iteratively.

In the RANS-based simulations presented in this document, a second order upwind approach is used to approximate the convection term and a second order central-differencing scheme is used for the diffusion term. 12 inner iterations are used to allow the solution to converge in each time step.

This project has received funding from the European Union's Horizon 2020 research and innovation programme under grant agreement No 851885. This output reflects the views only of the author(s), and the European Union cannot be held responsible for any use which may be made of the information contained therein.

2.2.3 Multi-Phase Modelling

Wave energy devices usually operate in the vicinity of the free surface interface since the extractable energy in the water column decreases with increasing depth. As a consequence, two phases – air and water – need to be modelled instead of one. Due to the shape and oscillatory nature of free surface waves, it is cumbersome to continuously adjust the cell structure of the domain in order to maintain a distinct cell-wise separation of the two phases.

The cell structure, called grid or mesh, is therefore defined statically, and both phases are allowed to enter a discrete control volume. As this violates the assumption of a constant density, an additional transport variable, the volume fraction γ_w is introduced. This variable is employed to indicate the ratio of water volume and total volume of a cell, with a value of 1 indicating a cell completely filled with water and a value of 0 indicating a cell entirely filled with air. The phase properties such as density and viscosity are then averaged for a cell described in equation (34).

$$\rho = \gamma_w \rho_{water} + (1 - \gamma_w)\rho_{air} \tag{34}$$

This approach is referred to as a Volume-Of-Fluid method and was developed by Hirt and Nichols. More information on the background of this approach can be found e.g. in (Ferziger & Peric, 2002; Hirt & Nichols, 1981).

2.2.4 Turbulence and Transition

Most wave energy systems can be assessed while neglecting viscous effects, since relative velocities between fluid and body and hence friction forces are often small. Instead, wave-body interaction is dominated by inertial or diffraction forces, which allows to employ accordingly simplified numerical models. Lifting-type wave energy converters by contrast are dominated by the lift and drag induced by the hydrofoils. For a cyclorotor WEC, as investigated in the LiftWEC project, their contributions in tangential direction tend to be of similar order.

The drag forces of the device, operating at Reynolds numbers of the order $10^5 - 10^6$, are dominated by friction forces which potential flow based methods cannot model explicitly due to their underlying assumption of an inviscid flow. In field methods based on the Navier-Stokes equation, friction forces can be modelled, as the flow velocity in the vicinity of the boundary is computed and hence the induced shear stresses can be derived.

One phenomenon which is often encountered in viscous flows is turbulence. The term turbulence refers to fluctuations of the flow field, which are small compared to the mean values for velocity and pressure. In order to neglect these fluctuations, considered to occur on time scales which are negligible for the investigated flow field, a time-averaging of transport variables is introduced, separating each value into a mean and a fluctuating part: $\phi = \bar{\phi} + \phi'$. By introducing this into equation (31) and averaging over time, the Reynolds-Averaged Navier-Stokes equation is obtained (with $\overline{\phi'} = 0$).

The closure problem, resulting from the fact that the average product of two fluctuating values, as obtained from the convection term, is not zero, is solved by introducing an additional pair of transport equations. These equations are referred to as a two-equation turbulence model. In this work, the $k\omega - SST$ turbulence model developed by Menter is employed (Menter, 1994). Further background information on the closure problem and the implementation of turbulence models can be found in literature, e.g. by Ferziger or Wilcox (Ferziger & Peric, 2002; Wilcox, 2006).

In this work, the CFD turbulence model has been extended by two limiters of the production term in the turbulent kinetic energy (TKE) transport equation. The first limiter is introduced in order to prevent an overprediction of TKE production in the vicinity of stagnation points, which may occur when using the $k\omega - SST$ model. This model is sometimes referred to as the realizable $k\omega SST$-model (Durbin, 1996).

The second model is used to prevent an unphysical, steady increase in turbulent kinetic energy when modelling free surface waves. This effect is inevitable when using standard two-equation eddy viscosity turbulence models, as has been shown by Larsen and Fuhrman (Larsen & Fuhrman, 2018). The limiter proposed in their publication has been applied in this work.

2.2.5 Mesh Motion and Boundary Conditions

Domain Definition

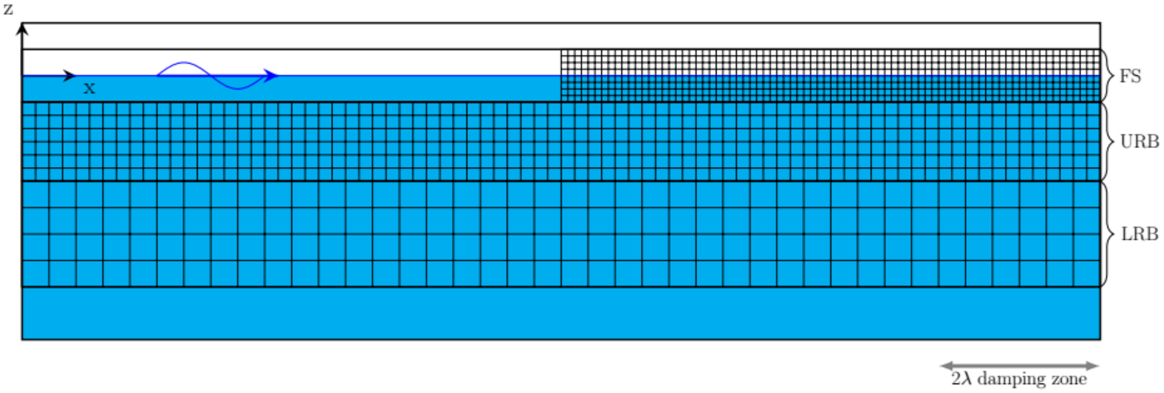

Figure 3: Definition of backrgound domain mesh indicating refinement zones to resolve wave propagation and location of global coordinate system.

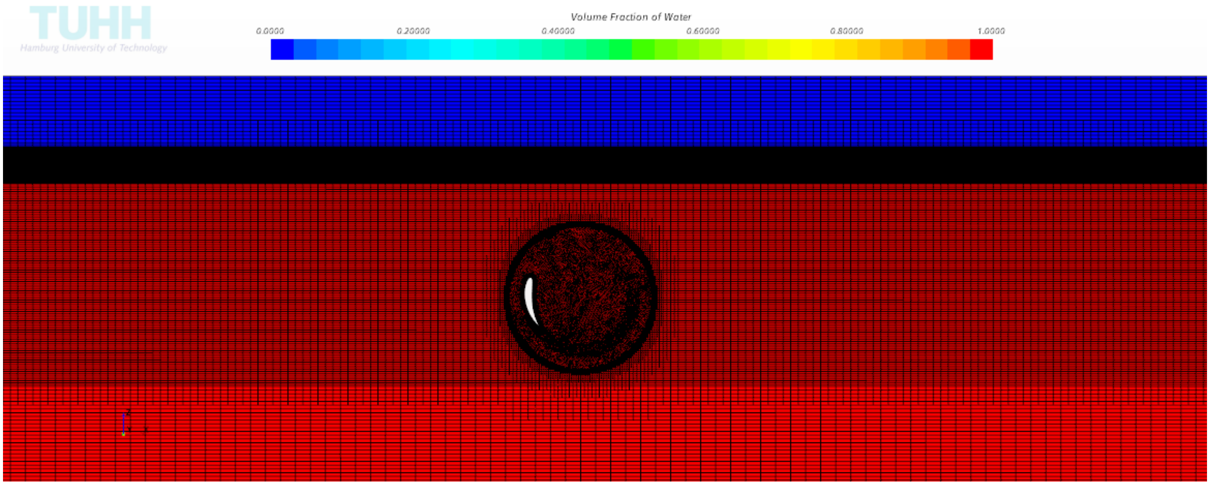

Figure 4: Side view of 2D mesh for single foil rotor below free surface showing free surface refinement zones, rotor overset mesh and foil wake refinement after $t = 0.5T$ *simulation time.*

The length of the numerical domain used during the validation study is adjusted for each run based on the incident wave length to a total length of 8λ. The rotor is placed at a distance 4λ from the domain inlet. The depth of the numerical tank is 3m, which corresponds to the depth of the physical wave tank. In lateral direction, the domain has a width of $0.01c$, with $c = 0.3m$ referring to the chord length of the foils used during the validation. The free surface is resolved using 120 cells per wave length and 15 cells per wave height. The resolution is reduced step wise by a factor of 2 in the upper refinement box (URB), starting at a depth of $z = -H$, and lower refinement box (LRB), starting at a depth of $z = -0.2\lambda$ (see Figure 3).

An overset mesh is used to simulate the motion of the foils through the earth-fixed background domain. The approach uses two independent grid structures: one cylindrical overset grid, which is fixed to the body and which resolves the flow field in the immediate vicinity of that body and one background grid which is inactive in the region of the body and active in the rest of the domain (Figure 4). On the outer edges of the overset region, active cells overlap and flow information is exchanged between grids using interpolation.

The overset interface between foil and background is using a distance weighted interpolation scheme of transport variables. While only considering the four nearest neighbours and a linear interpolation scheme, results have not indicated any visible influence on the flow field in the interface region. More information on the employed overset technique can be found in (Hadzic, 2005).

The foil is resolved using 120 cells per chord length. The trailing edge is truncated at $x = 0.99c$ and the remaining blunt edge resolved using 5 cells. The truncation is done in order to account for the limited realizability of an infinitely thin trailing edge in the physical model. The wake zone along the circular path is refined, as indicated in Figure 4, using a target cell size of $\Delta x = 0.015c$. The rest of the overset domain, including the corresponding area in the background grid, is discretized with a cell size of $\Delta x = 0.025c$.

Boundary Conditions

A quasi-2D domain is defined. The initial discretization of the numerical domain is defined for one of the side walls and then extruded in lateral direction. The length of the domain in lateral direction is defined as 1% of the chord length. Only one cell is used to discretize the domain in lateral direction. A three-dimensional definition is required when using StarCCM+, as the definition of free surface waves and the employment of the VoF interface tracking is only available for three-dimensional considerations.

Inlet

The inlet is defined with a prescribed profile of velocity and volume fraction. In simulation runs with external waves, these values are defined based on Stokes' fifth order wave theory (Fenton, 1985). In calm-water conditions, velocity is set to zero and the free surface interface is defined at the calm water line.

Bottom

The domain bottom is modelled as a rigid wall with a no-slip boundary condition. As flow velocities close to this boundary are expected to be low, no additional measures to resolve boundary flow were taken. The depth of the tank corresponds to the depth of the physical wave tank.

Outlet

The outlet used in this test series is defined with prescribed pressure and volume fraction profiles. For all test cases presented in this document, a flat free surface with a corresponding hydrostatic pressure profile and distribution of volume fraction is enforced.

Top

The upper boundary of the numerical domain is defined as a pressure outlet. The pressure is prescribed at atmospheric pressure levels.

Side Walls

The side walls of the numerical domain are defined as symmetry planes.

Source terms used in flow field

In addition to the standard set-up of StarCCM+, for which the theoretical background can be found in the corresponding manual (Siemens PLM Software, 2016), two additional user-implemented functions are used in the simulations presented in this document. The first is the Larsen-turbulence limiter described previously. The second is a source term added to the transport equations of momentum and volume fraction.

Specific damping/forcing zones are defined starting at the out- and inlet. In these zones, the free-stream values of the transport variables are compared to analytically derived values, i.e. the distribution of volume fraction and momentum in the vicinity of the inlet is compared to the analytical solution of a wave profile. The field solution is then gradually forced towards the analytical solution with decreasing distance to the boundary. If the analytical values of the velocity has a non-zero value, this approach is usually referred to as forcing, whereas a pure destruction of momentum is called damping. The forcing/damping approach used in this work is based on (Perić & Abdel-Maksoud, 2016). The lengths of the zones was 2λ. All other values were computed based on the analytical procedure proposed by Peric.

This project has received funding from the European Union's Horizon 2020 research and innovation programme under grant agreement No 851885. This output reflects the views only of the author(s), and the European Union cannot be held responsible for any use which may be made of the information contained therein.

3 EXPERIMENTAL SETUP

A detailed description of the experimental setup including aspects of model design construction and operation has been published in several previous, publicly available project Deliverables:

Deliverable D4.1: Design of the 2D scale model describes the conceptual background of the 2D test series and the design process of the components which per specifically constructed for this test campaign.

Deliverable D4.2: 2D scale model expands on the additional adjustments which were made to the tests based on first test runs.

Deliverable D4.4: Report on physical modelling of 2D LiftWEC concepts describes the results and lessons learned during testing, as well as the final configurations used during testing.

All data sets generated during the test campaign have been published. A description of how to access and interpret the data has been documented in *Deliverable D4.3: Open access experimental data from 2D scale model.*

In this section, only a brief summary of the experimental setup will be given. For further information the reader is encouraged to refer to the documents listed above.

3.1 DESCRIPTION OF EXPERIMENTAL TESTS

The 2D test campaign of the LiftWEC device was conducted in the wave flume of École Centrale de Nantes in Nantes, France. The flume has a total length of 140m, a width of 5m and a depth of 3m. In order to obtain a quasi-two-dimensional set-up of experimental tests, a subchannel was inserted into the wave flume. This subchannel was constructed using formworks, which are typically employed in construction when erecting concrete walls.

The walls of the subchannel were aligned parallel to the direction of wave propagation along the main axis of the flume. They extended from the bottom of the tank to a height of approximately 0.5m above the calm water surface, over a distance of 17m along the tank. The distance between the two channel walls was 0.49m. An image of the subchannel installed in the tank is shown in Figure 5. Figure 6 shows a CAD drawing of the setup, showing the position of the rotor model close to the subchannel centre. Figure 7 shows a top view of the experimental setup, indicating dimensions, tank coordinate system and locations of wave elevation gauges relative to the rotor position.

In order to install the rotor model, a gap was left in the channel centre and a frame fitted into the gap as a substructure for the rotor. The lateral distance between the side walls of the substructure equals the distance between channel walls, so that a smooth surface is maintained. The rotor itself is embedded in an aluminium top frame which could be lowered onto the substructure and removed between runs in order to adjust rotor settings or access the measuring equipment.

This project has received funding from the European Union's Horizon 2020 research and innovation programme under grant agreement No 851885. This output reflects the views only of the author(s), and the European Union cannot be held responsible for any use which may be made of the information contained therein.

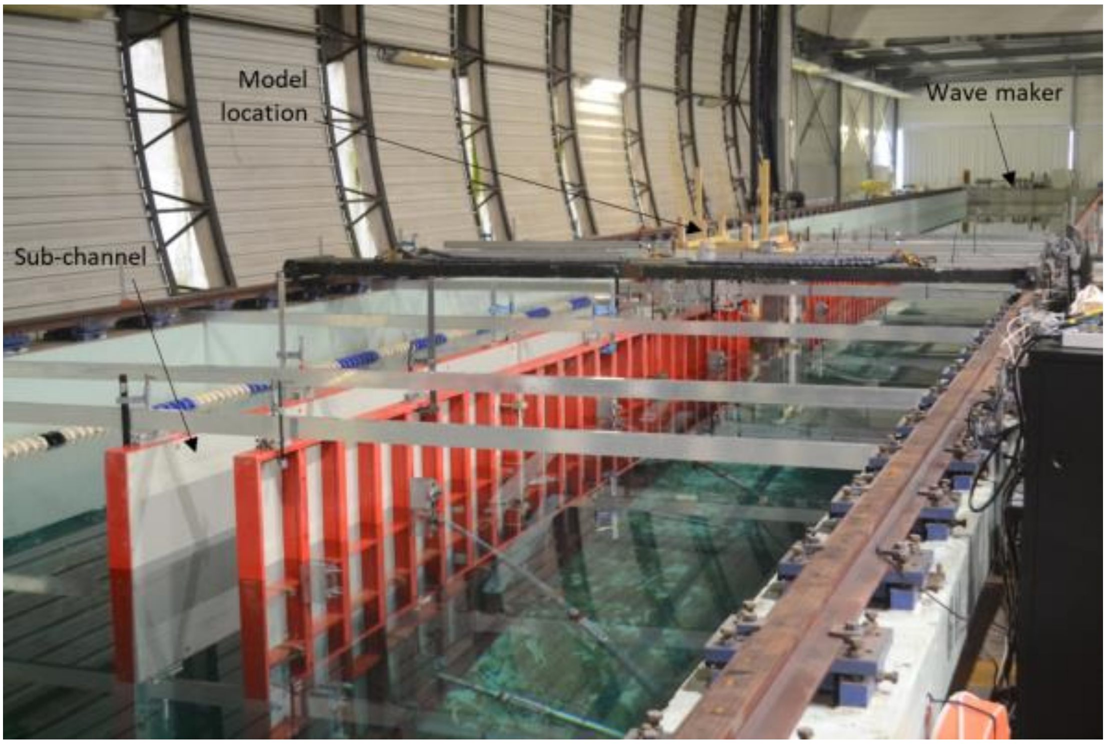

Figure 5: Wave flume at ECN with subchannel and cross-bars used to constrain channel wall displacement. Courtesy of ECN.

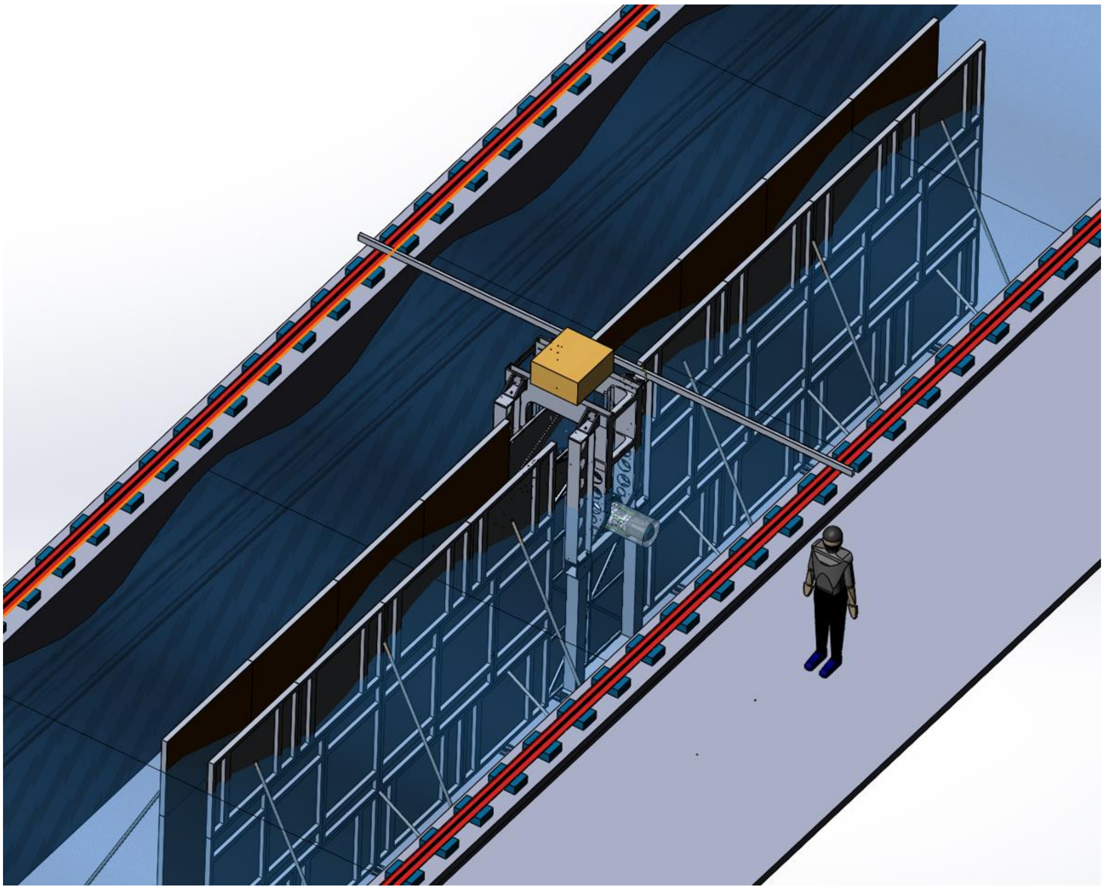

Figure 6: CAD drawing of subchannel scale showing placement of rotor model. Courtesy of ECN.

This project has received funding from the European Union's Horizon 2020 research and innovation programme under grant agreement No 851885. This output reflects the views only of the author(s), and the European Union cannot be held responsible for any use which may be made of the information contained therein.

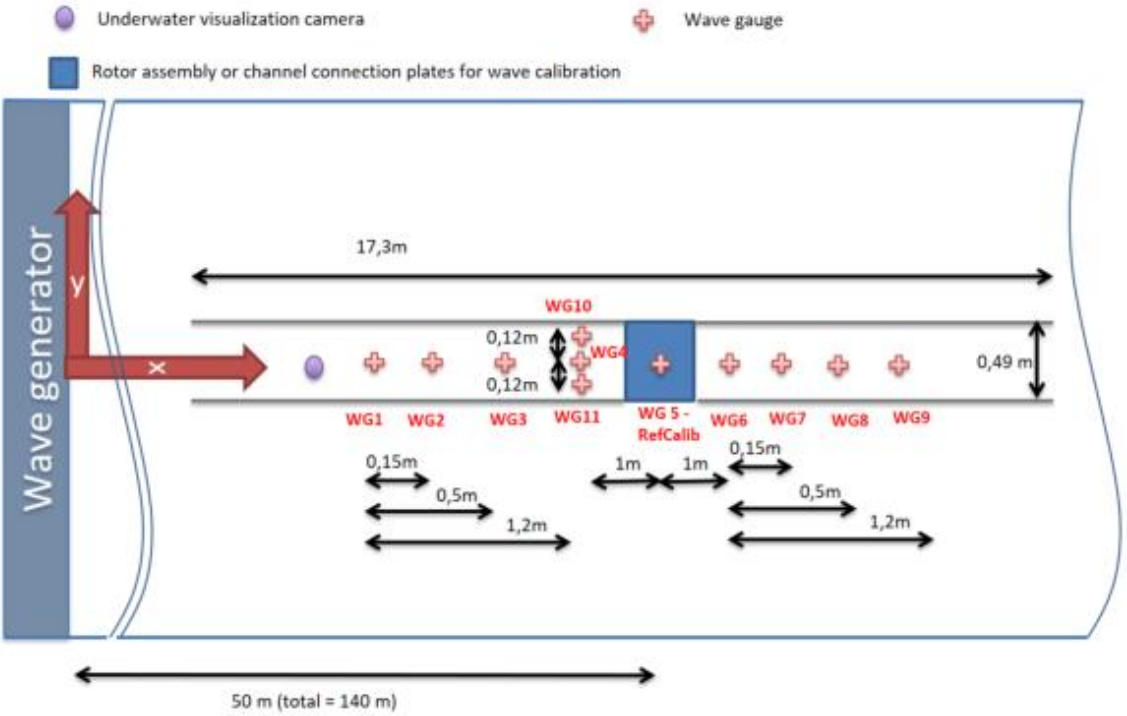

Figure 7: Sketch of experimental setup indicating location of rotor, position of wave gauges and orientation of tank-fixed coordinate system. Courtesy of ECN

Figure 8 shows the rotor top-piece, which was inserted into the subchannel gap. As can be seen, torque transducer and encoder, used to drive the rotor and measure its motion, are located outside of the subchannel in order to prevent disturbance of the rotor inflow. A central shaft is used to drive the rotor. Depending on the respective test run, zero, one or two foils are attached to the rotor. The struts, which support the foils in their excentrical position, are embedded in cylindrical disks made out of foam. Also embedded in these disks are the load sensors attached to the end of each strut. Two force sensors, one oriented in tangential direction at mid-chord and the other oriented in radial direction at mid-chord, are implemented for each strut, giving a total of 4 load sensors per foil.

Figure 9 shows an image of one of the foils employed during the test campaign. The foil models were milled out of a single piece of foam material. The profile shape was based on a NACA0015 geometry. As can be seen, the foils are curved. This was achieved by projecting the 0.3m chord line of the original NACA0015 profile to a circular path using a radius of $r = 0.3m$ in order to reduce the drag of the foils in circular motion. The span of the foils is $s = 0.49m$. The gap between fairings and foils is in the order of a few millimeters and will be considered negligible. The trailing edge was truncated at a thickness of 2mm to avoid breaking during trials.

During each test run, the pitch of the foil was fixed. The static pitch angles could be varied between $\varphi = [-12, -8, -4, 0, 4, 8, 12]^\circ$ inbetween test runs.

This project has received funding from the European Union's Horizon 2020 research and innovation programme under grant agreement No 851885. This output reflects the views only of the author(s), and the European Union cannot be held responsible for any use which may be made of the information contained therein.

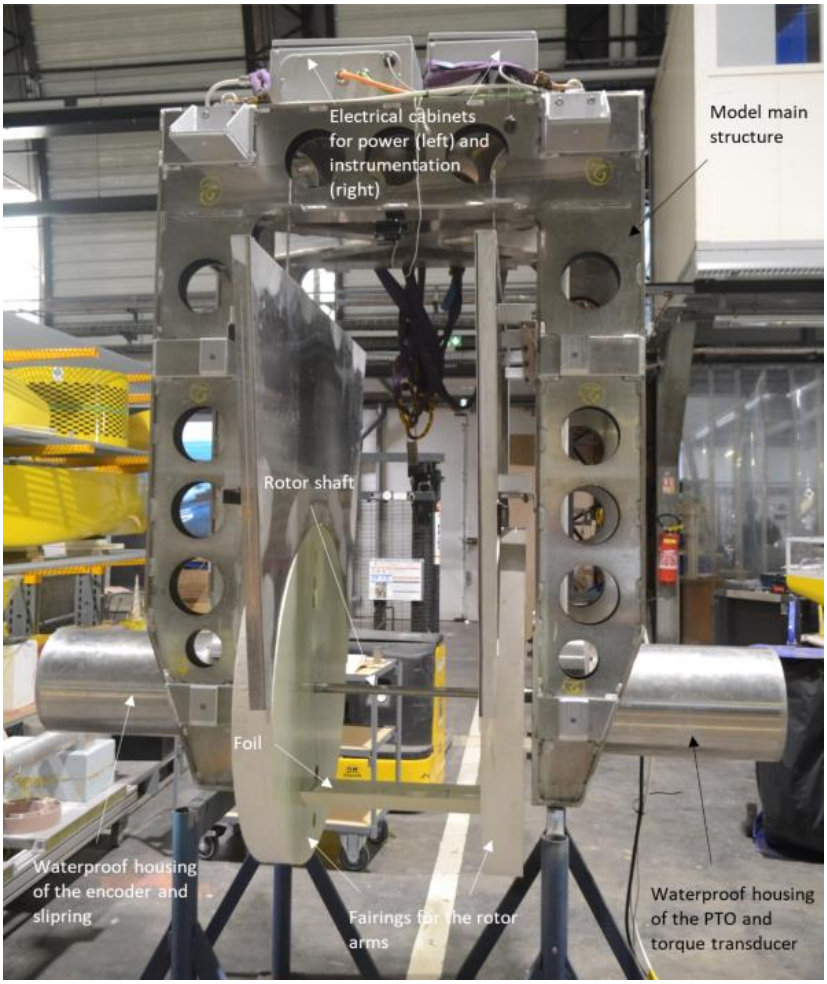

Figure 8: Removable aluminium rotor top structure with rotor fairings and housing for torque transducer and encoder. Courtesy of ECN.

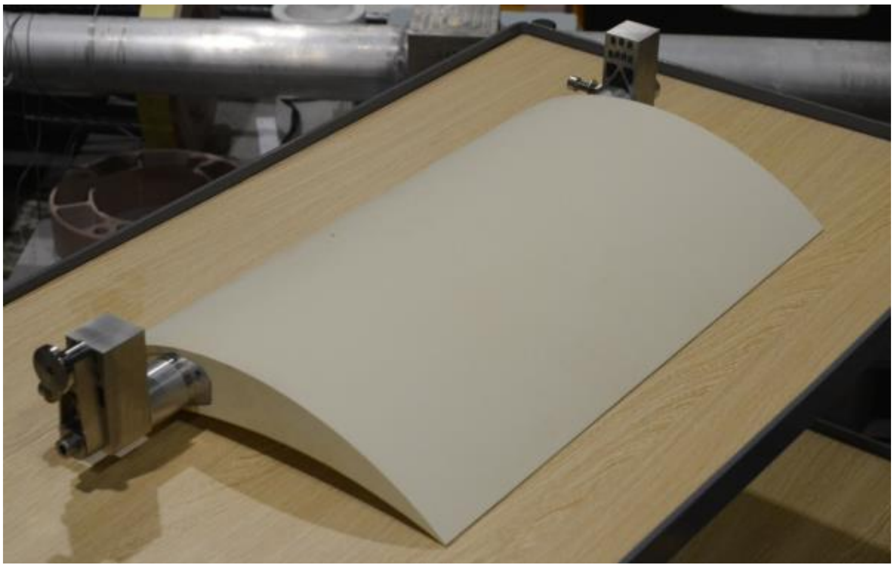

Figure 9: Curved foam foil used during campaign, including strut connectors which are later embedded in the foam fairings. Courtesy of ECN.

This project has received funding from the European Union's Horizon 2020 research and innovation programme under grant agreement No 851885. This output reflects the views only of the author(s), and the European Union cannot be held responsible for any use which may be made of the information contained therein.

3.2 POST-PROCESSING OF EXPERIMENTAL DATA

The raw data generated during experimental testing was pre-processed at ECN and then distributed to LiftWEC project partners working in numerical modelling of the device. While the measurement of free surface elevation using wave gauges has been treated in a number of publications, information on the experimental measurement of forces on a cyclorotor-type wave energy converter is not readily available. Therefore, a brief insight into the post-processing of force sensor measurement data shall be given here. Figure 10 shows the definition of the foil-fixed coordinate system, as well as definition of pivot point and the sign of the torque signal.

In tests with regular waves and bi-chromatic waves, the phase between rotor and wave was defined with 90° unless defined otherwise, meaning that Foil No°1 is at the top position of its motion cycle at zero-downcrossing of the wave. This case is also shown in Figure 10.

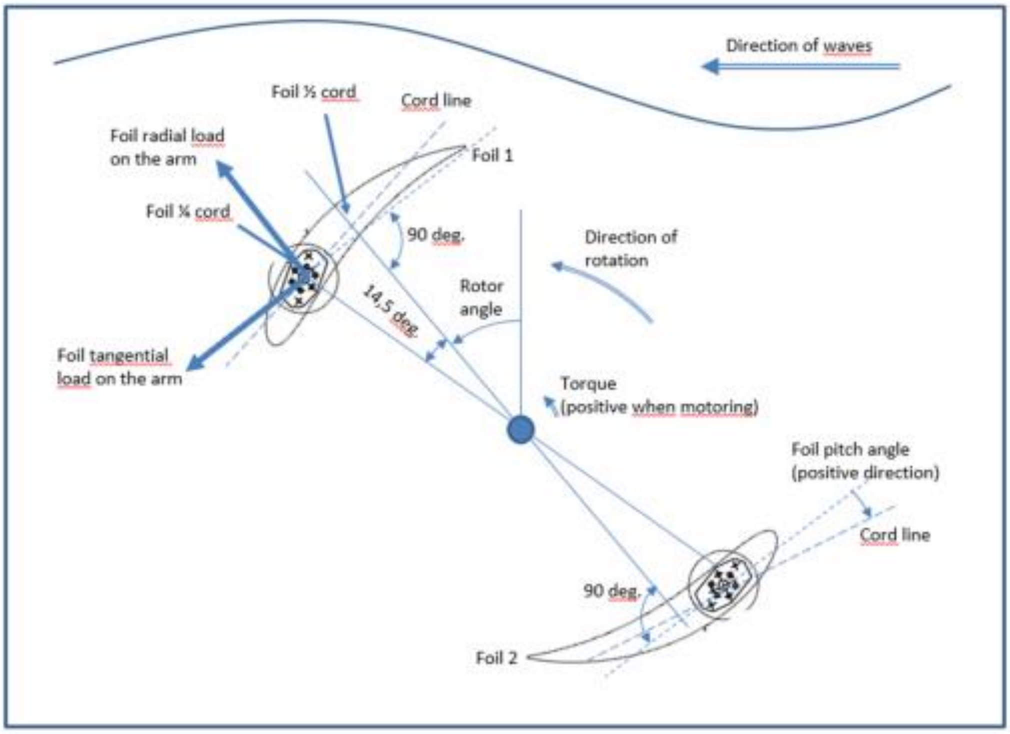

Figure 10: Definition of experimental coordinate systems and sign convention. Courtesy of ECN.

Force sensor data

Each foil attached to the rotor is supported by two struts, one on each side of the foil and embedded in the cylindrical rotor fairing to reduce its influence on the channel flow. On each side, two one-directional force sensors, oriented orthogonal to each other, are situated between strut and foil. In order to obtain the total force acting on the foil, the measurements of the two sensors for each respective direction have to be added. In most cases, good agreement between the forces measured on both sides is found. For some cases, distinct spikes, especially in the tangential force sensor measurements, can be found for one sensor, leading to strong deviation of the two measurements.

This project has received funding from the European Union's Horizon 2020 research and innovation programme under grant agreement No 851885. This output reflects the views only of the author(s), and the European Union cannot be held responsible for any use which may be made of the information contained therein.

This effect was found to be related to the flexibility of the cylindrical fairings, which in some runs were displaced in lateral direction due to pressure differences between sub-channel and main flume. This effect led to a contact between foil trailing edge and fairing, which caused the spikes in force sensor measurement. Since this effect was only found in a limited number of runs and within these runs for relatively short intervals, this will be neglected.

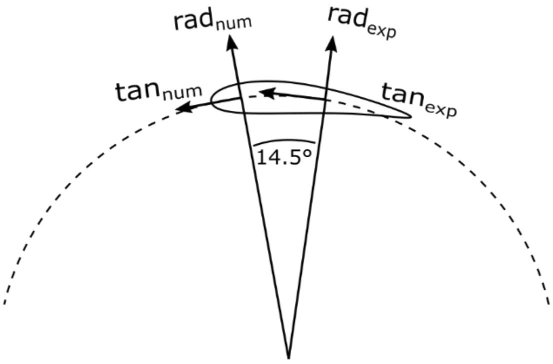

Figure 11: Relative position and orientation of numerical coordinate system at quarter chord and experimental coordinate system at mid-chord.

As previously stated, force sensors are oriented in radial and tangential direction at foil mid-chord. They are fixed to the struts supporting the foil and thus move with rotor motion. Forces are thus measured in a local, foil-fixed reference frame. This definition does not coincide with the orientation of the numerical coordinate system, which is located at quarter-chord. The reasoning behind this definition is the location of the centre of circulation, which is typically close to the quarter-chord position for small angles of attack. All results provided in this document will therefore be given in numerical reference frame unless stated otherwise. Experimental force results are therefore transformed (rotated) in the direction of rotation by $14.5°$.

Force correction

The main target of the numerical models validation in this report is the assessment of hydrodynamic forces acting on the LiftWEC device. Since during experimental testing not only hydrodynamic effects might be measured by the load sensors, a number of corrections is applied to the force sensor data before comparing them to the numerical simulation results.

Hydrostatic force correction

Despite aiming to build the foils as neutrally buoyant, small deviations might occur, e.g. due to uncertainties in construction material. This results in a non-zero hydrostatic force, which will act in the direction of gravitational acceleration if the mean density of the body is larger than the density of water and against it, if it is lower. Due to the rotor rotation, the direction of the hydrostatic force will constantly change when it is considered in a local reference frame. In order to assess these forces, a calibration run is conducted during which the rotor is rotated at very low angular velocity ($\omega = 0.1 rad/s$). This allows to maintain dynamic forces in negligible magnitudes and derive corrections for the hydrostatic force for each angular position of the rotor.

Centrifugal force correction

The foils and their suspension have a non-zero mass m. During rotation, this will result in a centrifugal force $F_c = mr\omega^2$, acting in radial direction at the assembly's centre of gravity (CoG). Due to iterations of the design and in order to maintain a certain flexibility during construction, the origin of the foil-fixed coordinate system in which forces are measured beforehand and thus deviates from the actual CoG-position. As a result, the centrifugal force will have an effect on both radial and tangential force measurements at half-chord position.

In order to derive a correction which is independent of rotation rate, the rotor is spun in air at several different rotation velocities. In all runs, the pitch angle is set to $\varphi = 0°$. Due to the relatively large mass of the rotor and the low drag and lift of the foils in air at zero-pitch, dynamic forces can be assumed negligible. Then for each run, the mass-equivalent of the centrifugal force in radial and tangential direction can be computed. The results of this procedure are shown in Table 1. As can be seen, a convergence of the mass can be observed with increasing velocity, with all rotational velocities larger than $\omega \geq 2rad/s$ giving similar results. The results obtained for the lowest rotational velocity are neglected since these are assumed to be most susceptible to measurement error.

For each run, the force sensor measurements are corrected using these mass values and the respective rotational velocity of the rotor.

Table 1: Mass equivalent values for centrifugal force correction in radial and tangential direction at mid-chord position. Courtesy of ECN.

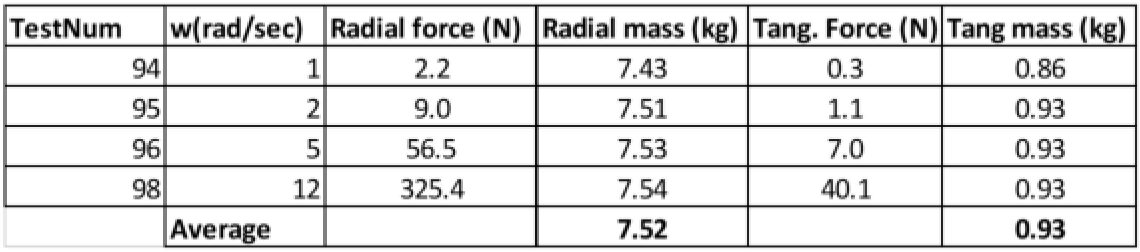

TestNum	w(rad/sec)	Radial force (N)	Radial mass (kg)	Tang. Force (N)	Tang mass (kg)
94	1	2.2	7.43	0.3	0.86
95	2	9.0	7.51	1.1	0.93
96	5	56.5	7.53	7.0	0.93
98	12	325.4	7.54	40.1	0.93
	Average		**7.52**		**0.93**

Synchronization of experimental and numerical results

In the wave tank, the central shaft of the model is located over $50m$ from the wave maker. This means, that after starting the wave generator, some time is required until the first wave crest reaches the rotor position. In order to obtain the desired phase shift between rotor motion, the wave is first generated without rotor motion and the time for the wave to reach the rotor position is measured. In a second test, the time required by the rotor to reach the target rotational velocity is evaluated. In the actual test, the rotor is started with a delay, calibrated so that it reaches its full rotational velocity at the same time the waves reach the rotor. Due to slight deviations of acceleration times, small deviations between pre-defined and actual rotor-wave phase shift are found. These are typically $< 5°$. This is further discussed on a case by case basis in the validation section of this report.

The numerical definition of phase shift between rotor and wave is straightforward, since both can be initialized with non-zero velocities. For tests without external waves, the encoder-measurement of rotor angle is used to synchronize all experimental and numerical time series.

In tests with externally generated waves, the wave elevation measurement at WG4 (see Figure 7) is used to synchronize experimental and numerical results. The recording of rotor angle from both is then compared to check for possible deviations in phase shift.

3.3 WAVE CALIBRATION

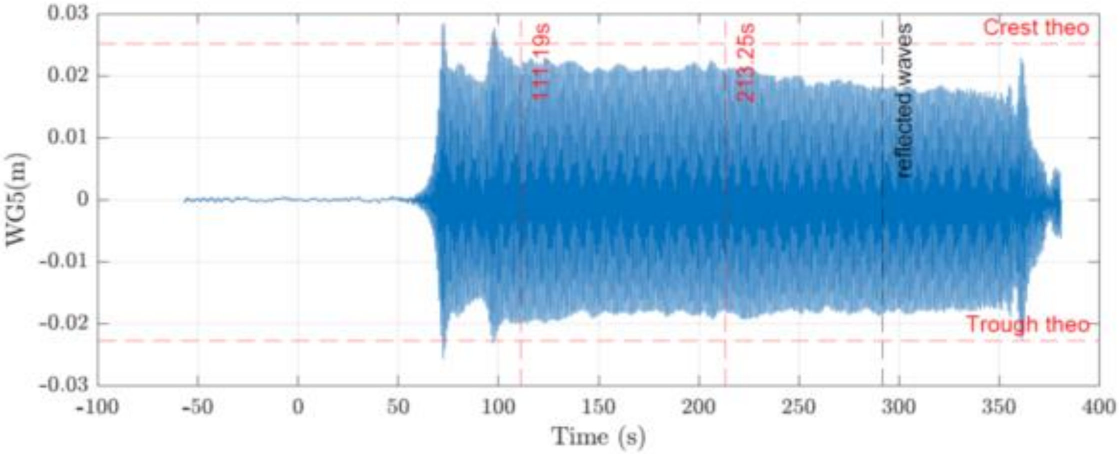

Figure 12: Free surface elevation measurement at WG5 over time during calibration of wave generation, showing target wave height and actual wave heights, as well as first wave front ($t \approx 70s$) and first peak due to subchannel reflections ($t \approx 100s$)

The presence of the sub-channel had an unforeseen impact on the wave conditions in the tank in that it led to a difference in propagation velocity of the wave between the sub-channel and the outer tank regions. As a result, a difference in wave phase is obtained at the channel outlet, which leads to refraction of the wave around the channel outlet region and the formation of further waves inside the channel. These waves are then reflected of the walls inside the channel, leading to an inhomogeneous wave field. The occurrence of this effect can be observed in Figure 12 around $t = 95s$, where a sudden change in wave height is visible.

3.3.1 Analysis of reflection

An analysis of the reflection mentioned above can be conducted using the wave calibration runs. 16 regular waves were measured without the device.

The analysis is conducted following the standard Mansard and Funke analysis (see (Mansard, & Funke, 1980). The method specifies a list of constraints for the placement of wave probes as a function of distance between wave probes relative to wave length. To respect these constraints, different sets of 3 probes are selected for the different regular waves. The waves and selected probes are presented in Table 2.

Table 2: Regular calibrated waves and wave gauge selection for reflection analysis

Wave ID	Amp nominal [m]	T nominal [s]	Wave gauge 1	Wave gauge 2	Wave gauge 3
2	0.024	1.0000	1	2	3
3	0.045	1.4222	2	3	4
4	0.035	1.2075	1	2	3
5	0.04	1.0000	1	2	3
6	0.075	1.8286	1	3	4
7	0.06	1.6000	2	3	4
8	0.0765	1.4222	2	3	4
9	0.0565	1.2075	1	2	3

This project has received funding from the European Union's Horizon 2020 research and innovation programme under grant agreement No 851885. This output reflects the views only of the author(s), and the European Union cannot be held responsible for any use which may be made of the information contained therein.

10	0.093	2.4615	4	5	6
11	0.093	2.2069	3	4	5
12	0.093	2.0000	3	4	5
13	0.1265	1.8286	1	3	4
14	0.1	1.6000	2	3	4
15	0.155	2.4615	4	5	6
16	0.155	2.2069	3	4	5
17	0.155	2.0000	3	4	5

The results of the analysis are presented in Table 3. *ampI* and *ampR* corresponds to the amplitude of the incident and reflected components respectively. *phiI* and *phiR* are the phases of the incident and reflected components, optimised so that the recomposed wave elevation is best matched to the record at the four first wave gauges, and *rCoef* is the reflection coefficient, i.e. the ratio between *ampR* and *ampI*, in %.

Table 3: Results of reflection analysis

calibWave	ampI [m]	ampR [m]	phiI [deg]	phiR[deg]	rCoef
2	0.024	0.007	360.00	100.17	26.8%
3	0.046	0.018	318.07	242.41	39.1%
4	0.036	0.010	292.61	360.00	27.4%
5	0.039	0.010	232.22	136.40	24.9%
6	0.080	0.024	334.70	292.94	30.1%
7	0.064	0.023	41.05	0.43	35.2%
8	0.077	0.033	360.00	287.55	43.2%
9	0.057	0.015	88.67	-85.56	26.6%
10	0.096	0.020	332.55	58.83	20.8%
11	0.100	0.019	-83.43	238.40	18.9%
12	0.098	0.025	156.27	293.93	25.9%
13	0.132	0.040	360.00	327.87	30.1%
14	0.099	0.042	83.64	40.02	42.8%
15	0.164	0.026	339.64	57.99	16.0%
16	0.168	0.031	-70.09	249.80	18.8%
17	0.169	0.035	194.87	329.54	20.9%

Figure 13 shows the incident and nominal wave amplitudes for the different wave periods. The incident wave amplitude is relatively well calibrated, with values slightly above target for the longest and highest waves.

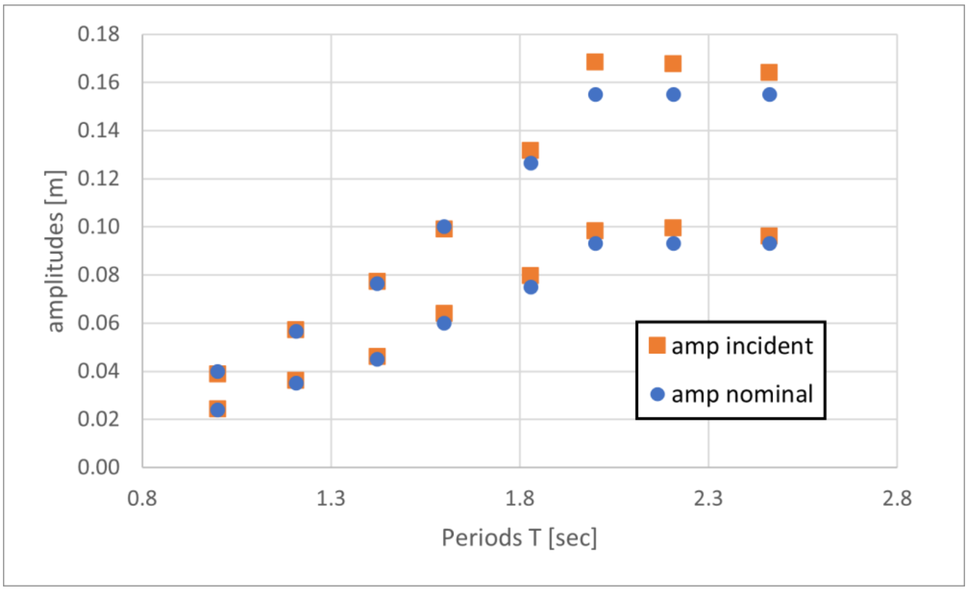

Figure 13: incident and nominal wave amplitudes as a function of the wave periods, calibration waves.

Figure 14 shows the reflection for 2 series of regular waves, with and high and low amplitudes, as a function of the wave period. In later investigations, only the higher wave amplitudes were used due to time constraints of the test campaign. Whereas the reflection coefficient varies as a function of the period, the values are above >15% for the full range of periods, which can be considered high (values under 10% would be expected in most wave energy basin tests). It is therefore recommended to focus the validation of numerical results on the part of the record before the reflection are present when it is possible.

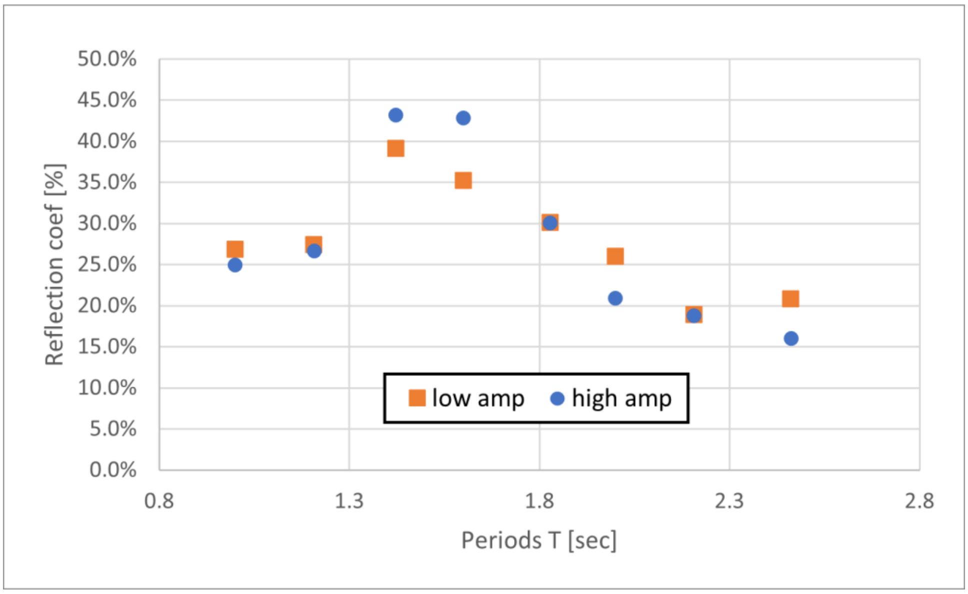

Figure 14: reflection coefficients as a function of the wave periods, calibration waves.

This project has received funding from the European Union's Horizon 2020 research and innovation programme under grant agreement No 851885. This output reflects the views only of the author(s), and the European Union cannot be held responsible for any use which may be made of the information contained therein.

3.3.2 Wave definition for RANS model

The definition of the wave height and period used in the RANS simulations is based on the mean wave height and period analysed for the time window between the first occurrence of subchannel reflections and the occurrence of reflections from the beach at the end of the wave tank. An exemplary evaluation window can be found marked in red in Figure 12. An evaluation of target and actual wave characteristics is shown in Table 4.

Table 4: Comparison of target and actual wave properties evaluated after wave calibration for monochromatic waves

Calibration Case ID	14	13	17	16	15
Target Wave Period [s]	1.60	1.80	2.00	2.20	2.40
Actual Wave Period [s]	1.60	1.83	2.0	2.21	2.46
Target Wave Height [m]	0.200	0.253	0.310	0.310	0.310
Actual Wave Height [m]	0.231	0.305	0.263	0.380	0.314

The initial phase of wave-device interaction, during which no reflection affects force measurements, was found to be around 2 wave periods in length, depending on the respective wave conditions. This was deemed too short for a comparison of integral values such as mean forces and mean cyclic responses to wave and free surface interaction, especially since a longer convergence time of forces was required in this model due to the consideration of wake effects. As a consequence, the uncertainty of the experimental comparison data is somewhat higher than initially desired, as will be shown in the result section of the RANS model.

This project has received funding from the European Union's Horizon 2020 research and innovation programme under grant agreement No 851885. This output reflects the views only of the author(s), and the European Union cannot be held responsible for any use which may be made of the information contained therein.

4 VALIDATION OF FUNDAMENTAL HYPOTHESIS FOR GLOBAL MODEL

The global model, and some of the models used for the control definition and structural design, relies on the hypothesis that the hydrodynamic loads on the foil can be estimated through a lift and drag forces, which is predictable based on the estimated foil angle of attack and Reynolds number.

It is therefore critical to use the experimental data gathered in the tank to validate the underlining hypothesis of these models. The hypothesis would be validated if it is possible to extract stable lift and drag coefficients across a range of angles of attack and Reynolds numbers from different test conditions. A further step of validation will be to show that the coefficients which can be obtained from the experimental testing match the tabulated coefficient available in the literature. This would allow the tools to efficiently experiment with different foil shapes.

4.1 METHODOLOGY:

The tank tests provide measures of radial and tangential forces on the foils. The methodology presented below is set to use these values to get back to the lift and drag forces and the lift and drag coefficients. The methodology however requires an estimation of the angle of attack (AoA) at each time step, as it cannot be measured during the experiment.

4.1.1 Hypothesis

Underlying hypothesis:

- The lift and drag coefficient can be defined deterministically from the AoA and Reynolds number
- The AoA at each time step can be defined: The flow variations at the vicinity of the foil are small enough and can be neglected, i.e. the flow relative to the foil can be regarded as uniform at each time step.
- The previous condition can be translated based on the fact that there is a constant point of the foil independent of the conditions where the relative fluid velocity can be defined.
- The incident fluid velocity is solely induced by the waves (wave reflection can be considered) and the foil motion induces negligible fluid motion itself.

4.1.2 Coordinate systems:

The coordinate systems are defined in Figure 15 for the analysis. It is closely matched with the system defined for the tank tests (indicated in Figure 10).

2D cases are considered only. 3 coordinate systems are defined:

- one fixed $\overrightarrow{x_0}O\overrightarrow{z_0}$ located at the free surface
- a second $\overrightarrow{x_0}O'\overrightarrow{z_0}$, same orientation as the first one, located at the centre of the rotor axis
- a rotating coordinate system $\overrightarrow{x_1}A\overrightarrow{z_1}$, located at the fixation point of the foil (1/4 chord length) along the foil path, with $\overrightarrow{x_1}$ tangent to the foil path, and $\overrightarrow{x_1}$ = $\overrightarrow{x_0}$ at t=0, and $\overrightarrow{z_1}$ = $\overrightarrow{z_0}$ at t=0
- θ is the rotor angle, positive anti-clockwise.
- α is the foil pitch angle, counted positive from $\overrightarrow{x_1}$ to $\overrightarrow{z_1}$

Following the definition of the coordinate systems, we have the following relations.

This project has received funding from the European Union's Horizon 2020 research and innovation programme under grant agreement No 851885. This output reflects the views only of the author(s), and the European Union cannot be held responsible for any use which may be made of the information contained therein.

$$\overrightarrow{x_1} = \cos\theta\overrightarrow{x_0} - \sin\theta\,\overrightarrow{z_0}$$
$$\overrightarrow{z_1} = \sin\theta\overrightarrow{x_0} + \cos\theta\,\overrightarrow{z_0}$$
$$\overrightarrow{x_0} = \cos\theta\overrightarrow{x_1} + \sin\theta\,\overrightarrow{z_1}$$
$$\overrightarrow{z_0} = -\sin\theta\,\overrightarrow{x_1} + \cos\theta\,\overrightarrow{z_1}$$

Some definitions: Incident wave propagation along x, following the Stokes second order wave theory, see **(DNVGL, 2017)**

- Incident fluid velocity at instant t: $\overrightarrow{V_I} = V_{Ix}\,\overrightarrow{x_0} + V_{Iz}\,\overrightarrow{z_0}$.
  V_{Ix} and V_{Iz} are defined from Stokes second order theory.
- Foil velocity at instant t: $\overrightarrow{V_f} = R\omega_R\overrightarrow{x_1}$ with $\omega_R = \dot{\theta}$
- The relative fluid velocity $\overrightarrow{V_{rI}}$ in the $\overrightarrow{x_1}A\overrightarrow{z_1}$ coordinate system is:

$$\overrightarrow{V_{rI}} = \overrightarrow{V_I} - \overrightarrow{V_f} = \begin{bmatrix} V_{rI,x} \\ V_{rI,z} \end{bmatrix} = \begin{bmatrix} -R\omega_R + V_{Ix}\cos\theta - V_{Iz}\sin\theta \\ V_{Ix}\sin\theta + V_{Iz}\cos\theta \end{bmatrix}$$

- In $\overrightarrow{x_1}A\overrightarrow{z_1}$, the angle β of $\overrightarrow{V_{rI}}$ is obtained as:

$$\beta = arccos\left(\frac{-V_{rI,x}}{\left\|\overrightarrow{V_{rI}}\right\|}\right)\cdot\left(\frac{-V_{rI,z}}{\left|V_{rI,z}\right|}\right)$$

with β defined as in Figure 16 and Figure 17.

- The foil angle of attack (AoA) is defined as $AoA = \alpha - \beta$
- The lift, drag, radial and tangential forces are named $\overrightarrow{F_L}, \overrightarrow{F_D}, \overrightarrow{F_R}, \overrightarrow{F_T}$. They are defined for different cases in Figure 16 and Figure 17.

This project has received funding from the European Union's Horizon 2020 research and innovation programme under grant agreement No 851885. This output reflects the views only of the author(s), and the European Union cannot be held responsible for any use which may be made of the information contained therein.

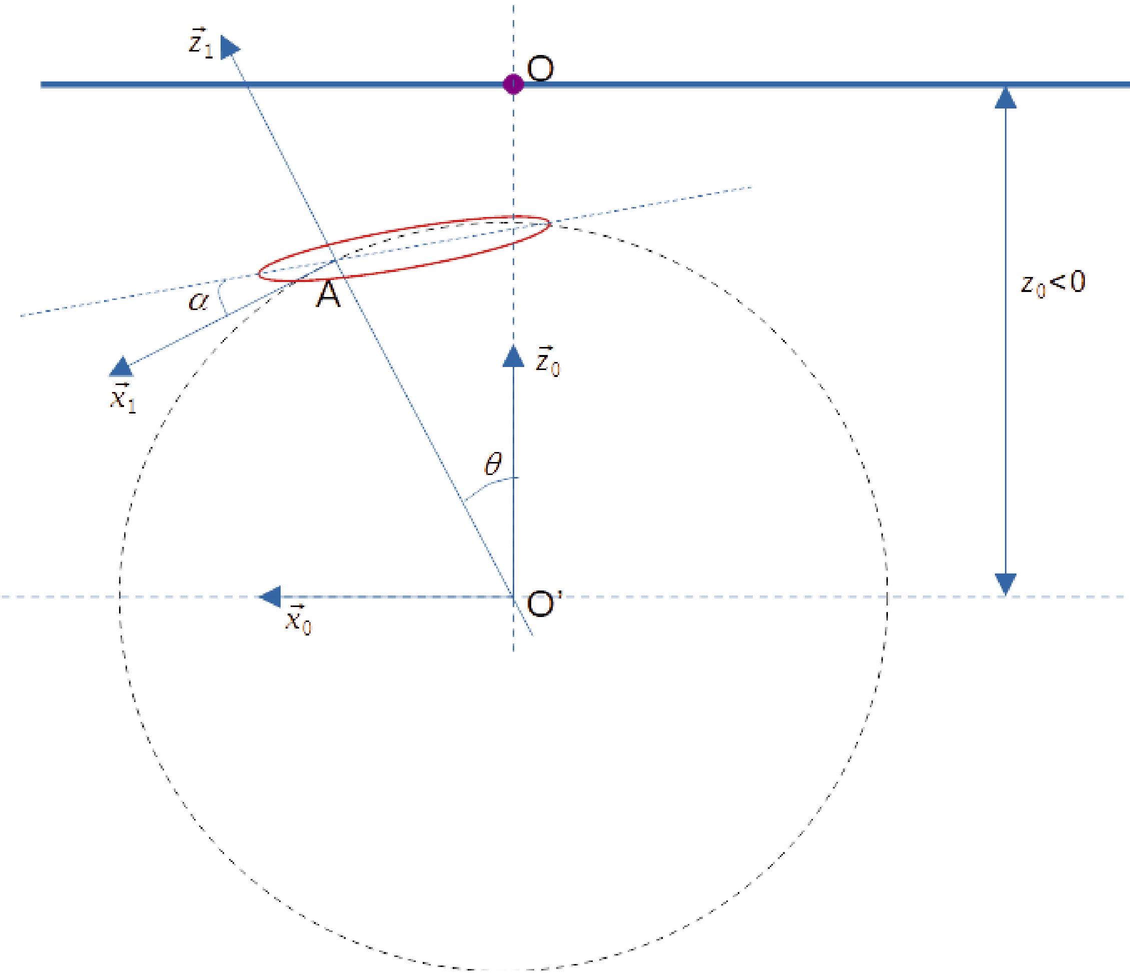

Figure 15: Coordinates systems of global model

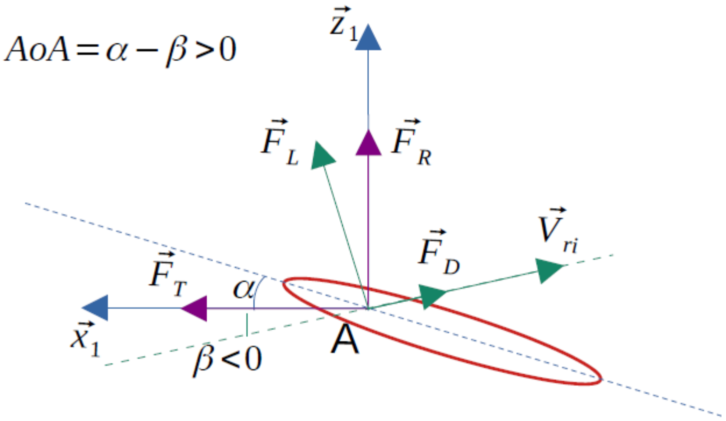

Figure 16: Definition of forces and angles for global model, case AoA > 0

This project has received funding from the European Union's Horizon 2020 research and innovation programme under grant agreement No 851885. This output reflects the views only of the author(s), and the European Union cannot be held responsible for any use which may be made of the information contained therein.

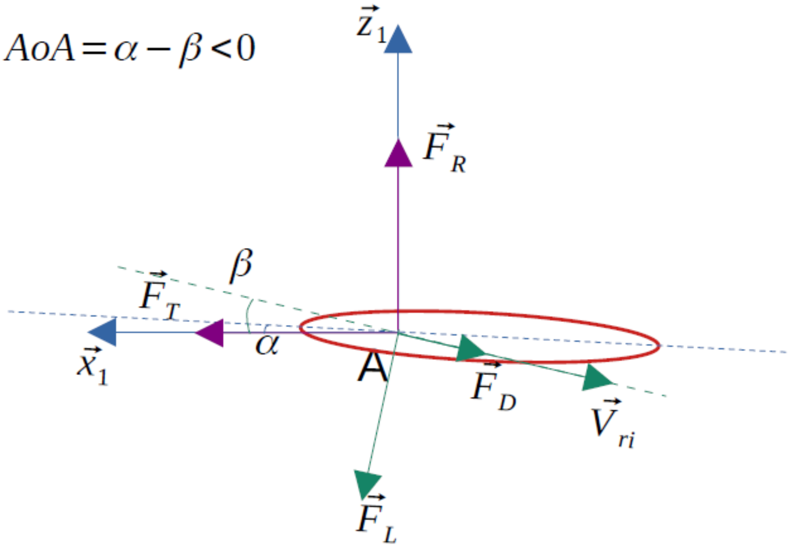

Figure 17: Definition of forces and angles for global model, case AoA < 0

4.1.3 Estimation of the AoA

As seen in the previous section, the correct estimation of β is crucial for the evaluation of the lift and drag coefficients. β depends on the foil velocity and position, which is measured during the experiment, but also depends on the estimation of the incident particle velocity (which is a function of the actual waves and the position at which the AoA is considered) which cannot be measured directly. The incident particle velocity must therefore be inferred from a propagation wave model: a second order Stokes wave model is selected in this study. Within this model, the required information is the wave height, wave period, depth of the tank and the phase of the wave.

As small differences in the wave model are critical to ensure the synchronisation of the rotor and the waves, it is preferred not to use the nominal wave data, but to use wave measurement in the tank.

Based on the observations of strong reflections during the tests, it is thought that a possible solution for this problem will be to use the data parts of the tests before the arrival of reflection where the measured radial and tangential forces are already stable.

Once the part of the record to analyse is selected, the amplitude, period and phase of the modelled incident wave is obtained by optimising those parameters through a least squares method: the second order surface elevation is matched with the record of the wave gauge number 4 (see Figure 7).

Using this incident wave, the velocity vector $\vec{V_I}$ can be estimated in the vicinity of the foil. In this study, the point of interest is defined at the ¼ chord point of the foil. The angle β and the AoA can then be obtained from $\vec{V_I}$ and the foil velocity $\vec{V_f}$.

4.1.4 Resolution of Cd and Cl:

- Case AoA>0
    a. Drawing hypothesis

$$\beta < 0 \;\Rightarrow\; \sin\beta < 0$$
$$|\beta| < \frac{\pi}{2} \Rightarrow\; \cos\beta > 0$$

This project has received funding from the European Union's Horizon 2020 research and innovation programme under grant agreement No 851885. This output reflects the views only of the author(s), and the European Union cannot be held responsible for any use which may be made of the information contained therein.

   b. Expression of F_T and F_R

$$\begin{cases} F_T = -\left\|\overrightarrow{F_L}\right\|\sin\beta - \left\|\overrightarrow{F_D}\right\|\cos\beta \\ F_R = \left\|\overrightarrow{F_L}\right\|\cos\beta - \left\|\overrightarrow{F_D}\right\|\sin\beta \end{cases}$$

- Case AoA < 0
   a. Drawing hypothesis

$$\beta > 0 \;\Rightarrow\; \sin\beta > 0$$
$$|\beta| < \frac{\pi}{2} \Rightarrow \; \cos\beta > 0$$

   b. Expression of F_T and F_R

$$\begin{cases} F_T = \left\|\overrightarrow{F_L}\right\|\sin\beta - \left\|\overrightarrow{F_D}\right\|\cos\beta \\ F_R = -\left\|\overrightarrow{F_L}\right\|\cos\beta - \left\|\overrightarrow{F_D}\right\|\sin\beta \end{cases}$$

Def:

$$c = \frac{1}{2}\cdot S\cdot C\cdot\rho\cdot\left\|\overrightarrow{V_{rI}}\right\|^2 > 0$$
$$\left\|\overrightarrow{F_L}\right\| = cC_L \; and \; \left\|\overrightarrow{F_D}\right\| = cC_D$$

In the case AoA>0, the equation of the radial and tangential force can be written as:

$$\begin{cases} F_T = -\,cC_L\sin\beta - cC_D\cos\beta \\ F_R = cC_L\cos\beta - cC_D\sin\beta \end{cases}$$
$$\begin{cases} C_L = \dfrac{-1}{c\sin\beta}(F_T + cC_D\cos\beta) \\ F_R = cC_L\cos\beta - cC_D\sin\beta \end{cases}$$
$$\begin{cases} C_L = \dfrac{-1}{c\sin\beta}(F_T + cC_D\cos\beta) \\ F_R = \dfrac{-\cos\beta}{\sin\beta}(F_T + cC_D\cos\beta) - cC_D\sin\beta \end{cases}$$
$$\begin{cases} C_L = \dfrac{-1}{c\sin\beta}(F_T + cC_D\cos\beta) \\ -C_D c\left(\dfrac{\cos\beta^2}{\sin\beta} + \sin\beta\right) = F_R + \dfrac{\cos\beta}{\sin\beta}F_T \end{cases}$$
$$\begin{cases} C_L = \dfrac{-1}{c\sin\beta}(F_T + cC_D\cos\beta) \\ C_D = -\dfrac{\sin\beta}{c}\left(F_R + \dfrac{\cos\beta}{\sin\beta}F_T\right) \end{cases}$$

A similar derivation in the AoA<0 yield:

$$\begin{cases} F_T = cC_L\sin\beta - cC_D\cos\beta \\ F_R = -cC_L\cos\beta - cC_D\sin\beta \end{cases}$$

$$\begin{cases} C_L = \dfrac{1}{c\sin\beta}(F_T + cC_D\cos\beta) \\ F_R = -cC_L\cos\beta - cC_D\sin\beta \end{cases}$$

$$\begin{cases} C_L = \dfrac{1}{c\sin\beta}(F_T + cC_D\cos\beta) \\ F_R = \dfrac{-\cos\beta}{\sin\beta}(F_T + cC_D\cos\beta) - cC_D\sin\beta \end{cases}$$

$$\begin{cases} C_L = \dfrac{1}{c\sin\beta}(F_T + cC_D\cos\beta) \\ -C_D c\left(\dfrac{\cos\beta^2}{\sin\beta} + \sin\beta\right) = F_R + \dfrac{\cos\beta}{\sin\beta}F_T \end{cases}$$

$$\begin{cases} C_L = \dfrac{1}{c\sin\beta}(F_T + cC_D\cos\beta) \\ C_D = -\dfrac{\sin\beta}{c}\left(F_R + \dfrac{\cos\beta}{\sin\beta}F_T\right) \end{cases}$$

4.1.5 Data correction from the tank:

The point at which the force and rotor angle are provided from the tank test do not match the defined coordinate system presented in this document. The following correction are taken:

$$\begin{aligned} F_R &= F_{R,ECN}\cos\delta + F_{T,ECN}\sin\delta \\ F_T &= -F_{R,ECN}\sin\delta + F_{T,ECN}\cos\delta \\ \theta &= \theta_{ECN} + \delta \end{aligned}$$

with $\delta = 14.5\ deg$.

4.1.6 Potential sources of errors

The estimation of β and the AoA is crucial to the estimation of the coefficient. The following event can induce issues with this:

- The point at which the incident velocity is taken is somewhat arbitrary. It is taken at the ¼ chord position but there is no absolute definition or justification for it.
- The direction of the lift force can change completely for small changes of the angle of attack around 0 deg. Any error on the actual pitch angle of the foil, even of 1 or 2 degrees will compromise the estimation of the coefficients at low angle of attack.
- The incident velocity vector is estimated from a modelled, idealised second order waves. It is fitted on the 4th wave gauge. Another choice of gauge would yield slightly different values of phase and amplitude.
- The model assuming that all the forces on the foil are due to lift and drag proportional to the relative velocity squared is simplistic.

4.2 RESULTS

4.2.1 Data used from experiments

The extraction of the coefficient focuses on the 0 degree pitch angle with regular waves, and the tests with no waves and different pitch angles. This is slightly arbitrary, but it limits the risk of errors associated with the elements shown in the previous section: it is anticipated that the 0 degree position is easier to measure accurately, and running the foil at 0 deg pitch should generate less induced loads which will disturb the incident wave field.

Tests with a single foil are also preferred as these will also limit the generation of flow disturbance from the rotor itself. One could therefore expect to have lower uncertainty in the results used to characterise the foil.

Table 5: tests used and limits of record associated.

Test number	108	109	110	112	113	114
Start [sec]	54	50.5	43	39	60	60
End [sec]	62	55	50	45	80	80

Figure 24 shows the start of the record for test 110. One can observe that from t=43 to t=50sec, the radial and tangential forces are rather constant, and the signal from all the wave gauge is consistent (to ease the visualisation, a phase shift based on the position of the wave gauge relative to WG5 has been applied on each wave signal to synchronise them with the wave elevation at the position of the device). Past t=50sec, the wave gauge signals diverge, which is due to the reflection arriving, and the forces signals are less stable, with the apparition of the “double” oscillations signal. It was therefore decided to only use the nearly periodic part of the signal for this analysis. The window selected for each test is based on a similar analysis. For tests 113 and 114, such window cannot be identified, and therefore a later part of the signal is considered. In these cases, an analysis of incident and reflected analysis is done, and the incident wave particle velocity considered to determine the AoA is considered as the sum of both waves.

This project has received funding from the European Union’s Horizon 2020 research and innovation programme under grant agreement No 851885. This output reflects the views only of the author(s), and the European Union cannot be held responsible for any use which may be made of the information contained therein.

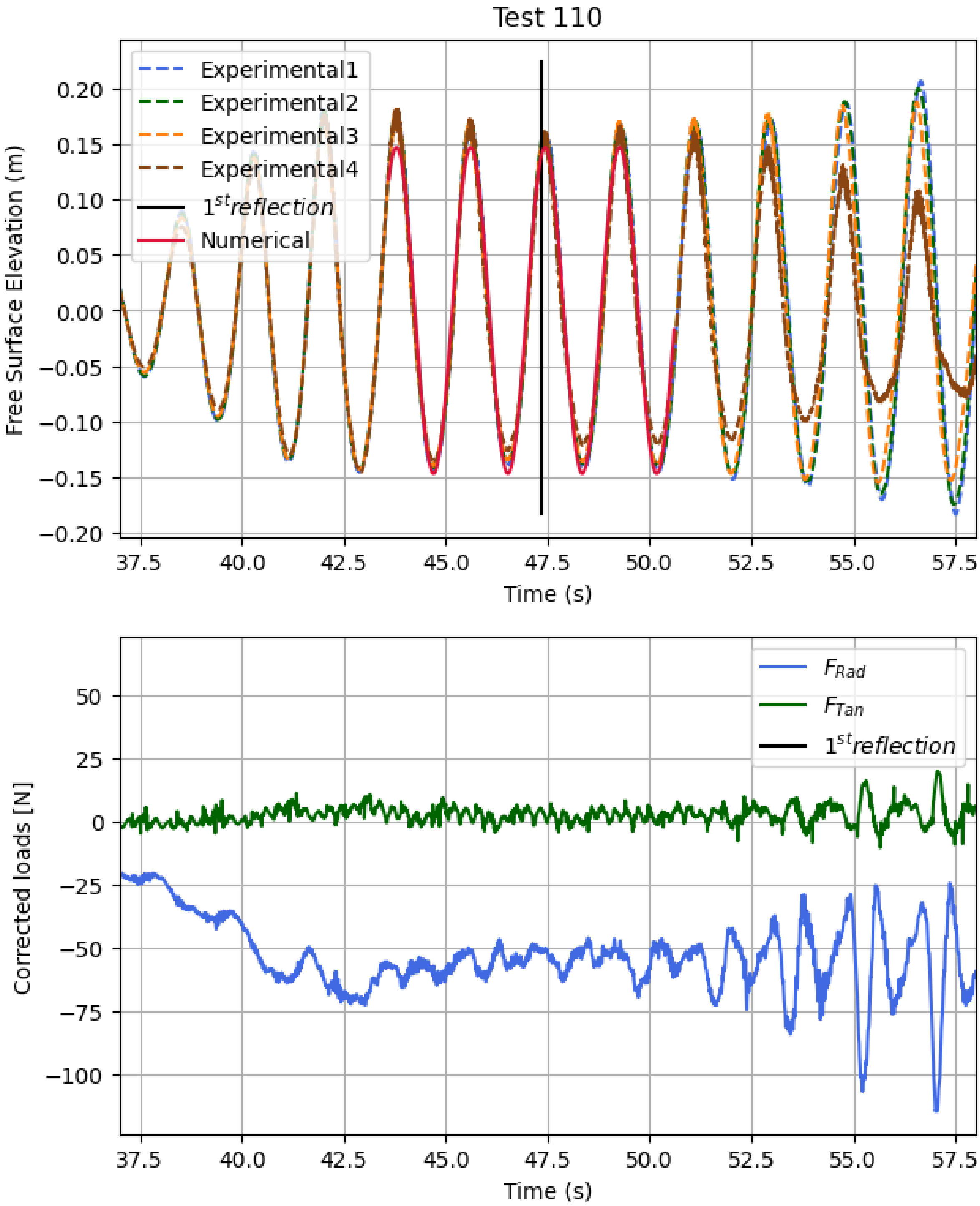

Figure 18: Test 110, wave records 1 to 4 and measured forces

4.2.2 Reflection coefficients

For tests where a stable window before the reflection cannot be identified, it is necessary to conduct and incident and reflection wave analysis.

This project has received funding from the European Union's Horizon 2020 research and innovation programme under grant agreement No 851885. This output reflects the views only of the author(s), and the European Union cannot be held responsible for any use which may be made of the information contained therein.

For the utilised tests to derive the coefficients, only tests 113 and 114 are in the situation defined above. The reflection coefficients obtained for these tests are the ones corresponding the calibration wave 16 and 15 respectively of Table 2.

This project has received funding from the European Union's Horizon 2020 research and innovation programme under grant agreement No 851885. This output reflects the views only of the author(s), and the European Union cannot be held responsible for any use which may be made of the information contained therein.

4.2.3 Individual test results

4.2.3.1 Test 109

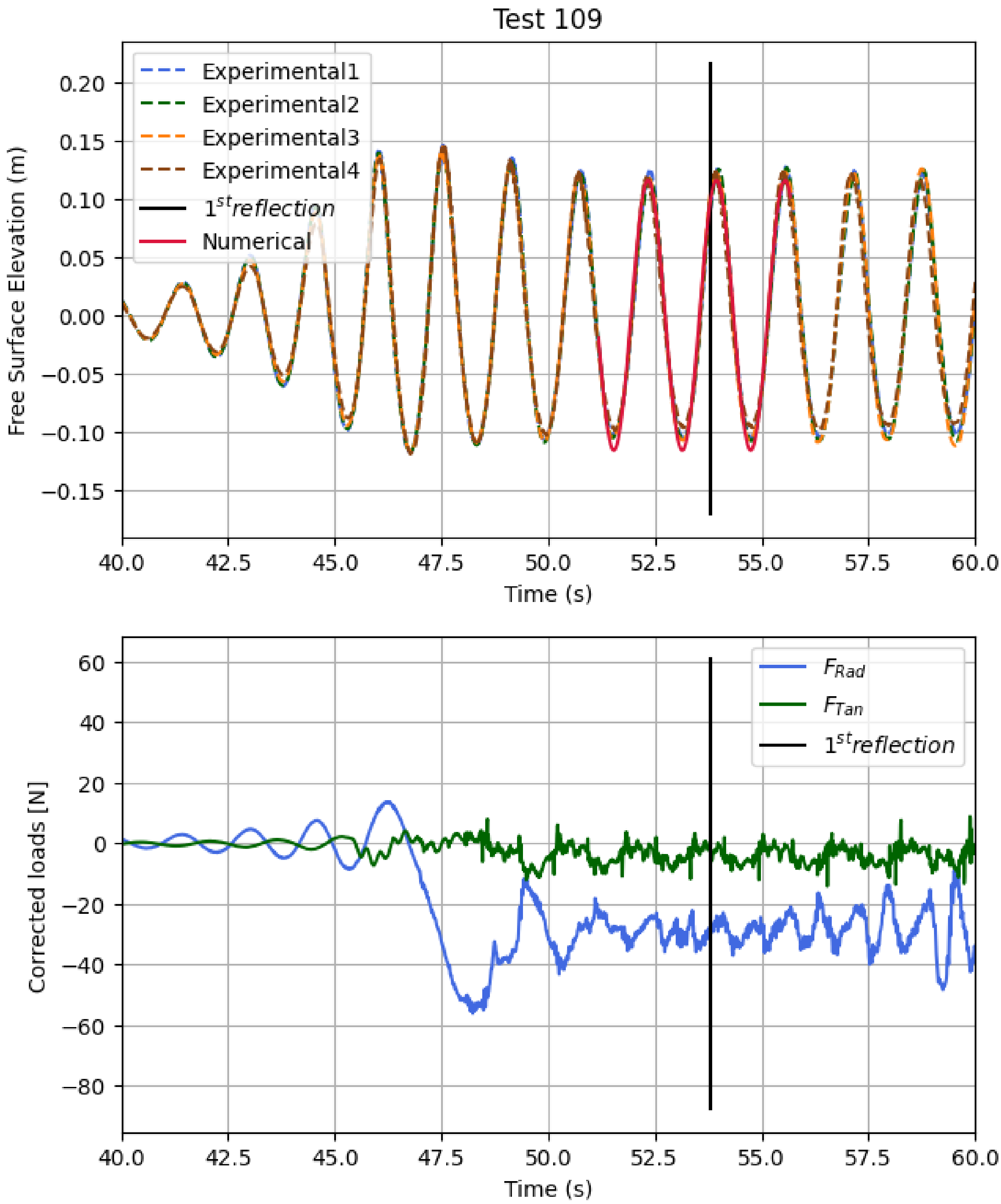

Figure 19: Base data for test 109, between 40 and 60 seconds of record. A phase shift is introduced in the wave record to synchronize signals based on the position of wave gauge 5 (located at the device position).

For test 109, the record is analysed before the reflection, where the radial and tangential forces are the most stable. It can be observed on Figure 19 that after the arrival of the wave train and the ramp

This project has received funding from the European Union's Horizon 2020 research and innovation programme under grant agreement No 851885. This output reflects the views only of the author(s), and the European Union cannot be held responsible for any use which may be made of the information contained therein.

up of the motor speed (around 47.5 sec on the record), the loads measured are rather stable for a few oscillations. However, shortly after the estimated time for the first reflection, the variability of the loads increases significantly.

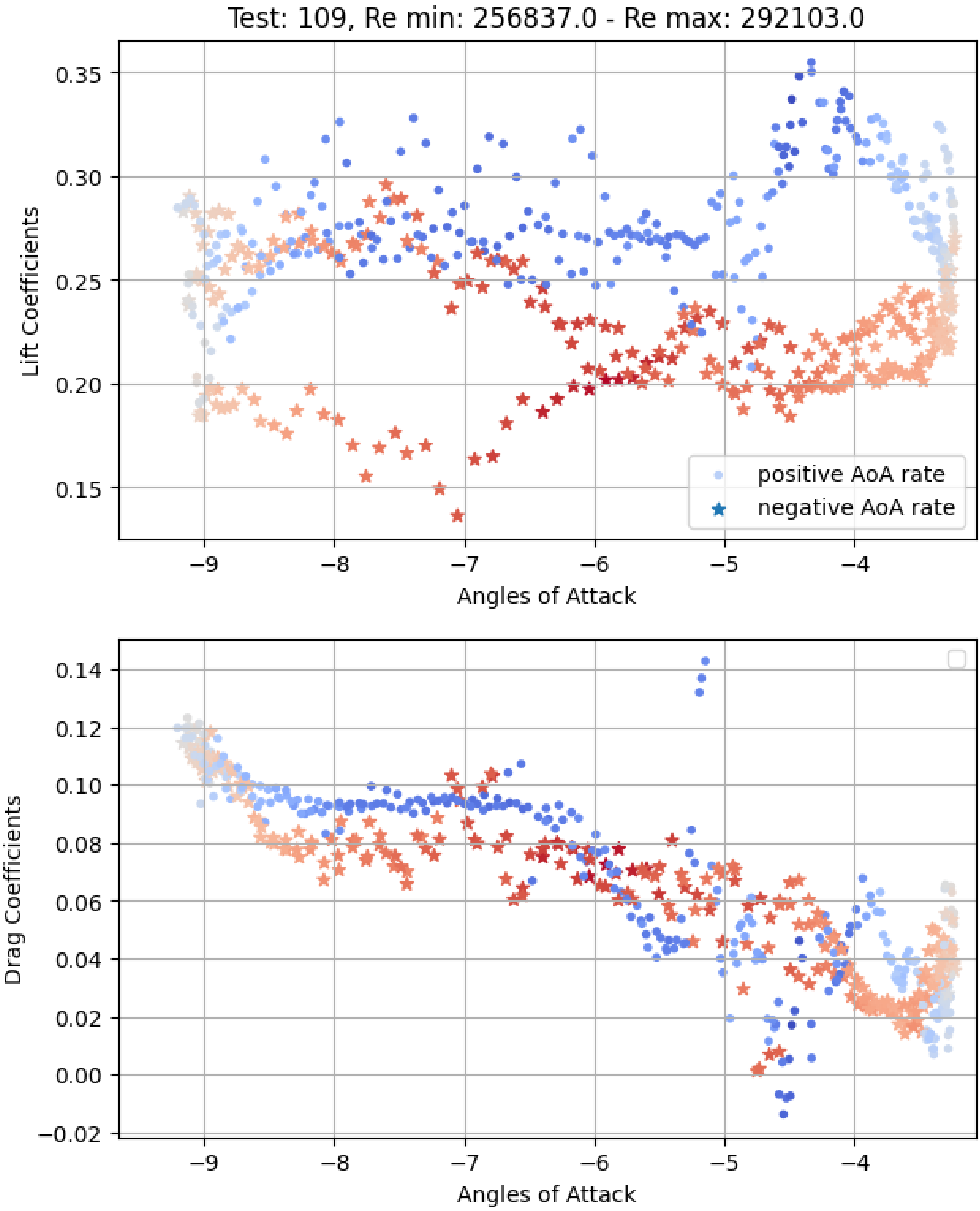

Figure 20 : Estimated C_L and C_D coefficients for test 109

This project has received funding from the European Union's Horizon 2020 research and innovation programme under grant agreement No 851885. This output reflects the views only of the author(s), and the European Union cannot be held responsible for any use which may be made of the information contained therein.

Figure 20 shows the resulting C_D and C_L coefficients from test 109 as a function of the estimated AoA. The coefficients are rather stable. The observations are differentiated between positive AoA and negative AoA rate, i.e. points for which the rate of change of the AoA is positive or negative. The colour of the points is linked to the estimated Reynolds number, which varies from $\approx$257000 to $\approx$292000. In particular, for the C_L coefficient, the AoA rate of change appears to have an impact on the estimated coefficient values, but it could also be potentially linked to the Reynolds number only.

4.2.3.2 Test 113

For Test 113, it is not possible to identify a part of the record with stable loads measurement before the arrival of the reflections. It is therefore necessary to conduct the analysis with incident and reflected analysis.

Figure 21 shows the data used for the analysis around the window selected in the record. The lift and drag composition are less stable than in test 109.

Figure 22 shows the wave gauge records for test 113, including the measures during the corresponding tank calibration run, the modelled second order wave without counting the reflection (“base numerical”) and the modelled wave elevation with the incident and reflection wave analysis (“ref numerical”). It can be observed that the “ref numerical” signal provides an acceptable approximation of the calibration signals for the wave gauge 1 to 5, the ones for which the phases have been optimised.

Figure 23 shows the resulting C_D and C_L coefficients from test 113 as a function of the estimated AoA. The coefficients are rather stable from wave cycle to wave cycle. The observations are differentiated between positive AoA and negative AoA rate, i.e. points for which the rate of change of the AoA is positive or negative. The colour of the points is linked to the estimated Reynolds number, which varies from $\approx$169000 to $\approx$203000. As for test 109, for the C_L coefficient, the AoA rate of change appears to have an impact on the estimated coefficient values.

This project has received funding from the European Union’s Horizon 2020 research and innovation programme under grant agreement No 851885. This output reflects the views only of the author(s), and the European Union cannot be held responsible for any use which may be made of the information contained therein.

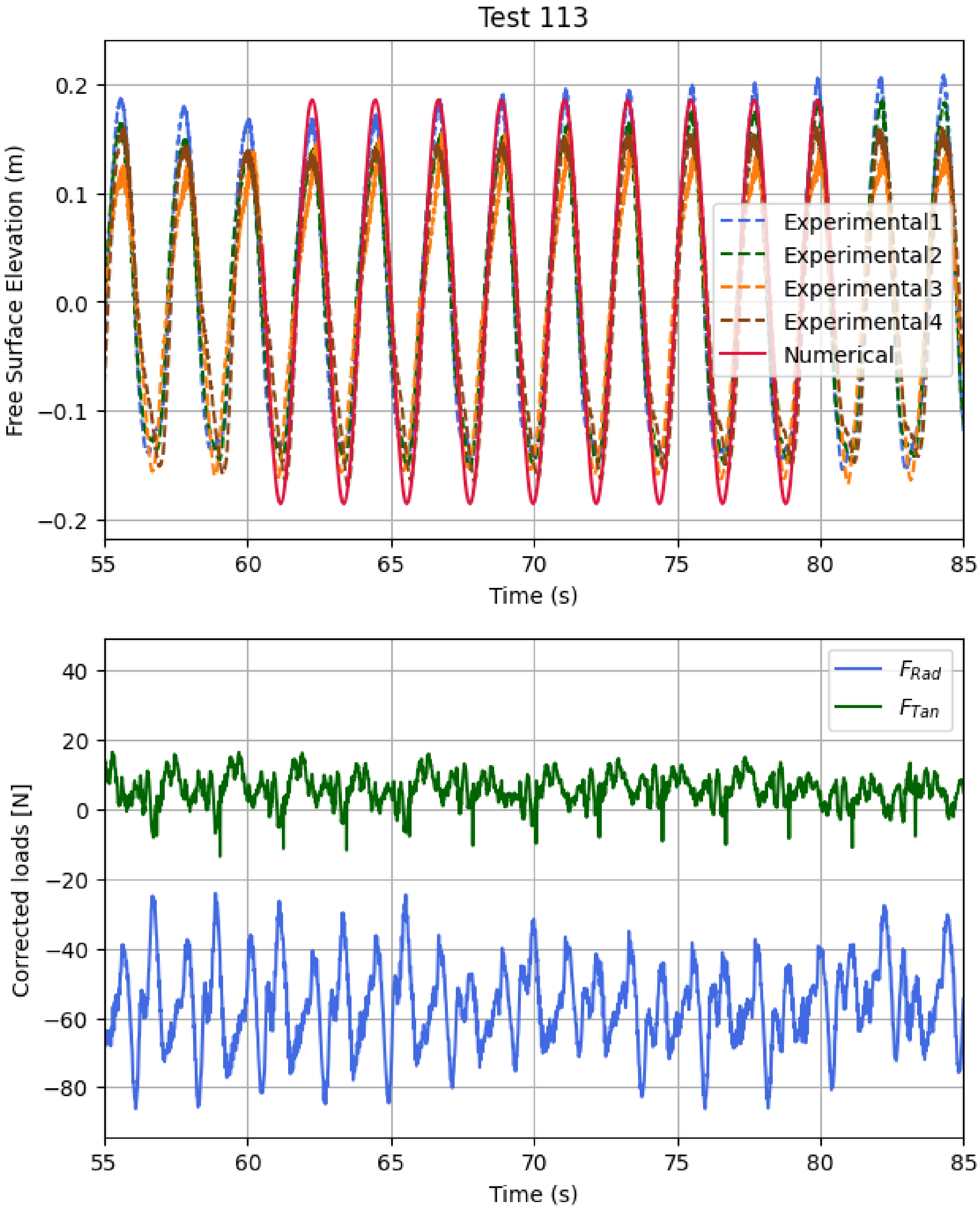

Figure 21: Base data for test 113, between 55 and 85 seconds of record. A phase shift is introduced in the wave record to synchronised them all at the position of wave gauge 5 (located at the device position).

This project has received funding from the European Union's Horizon 2020 research and innovation programme under grant agreement No 851885. This output reflects the views only of the author(s), and the European Union cannot be held responsible for any use which may be made of the information contained therein.

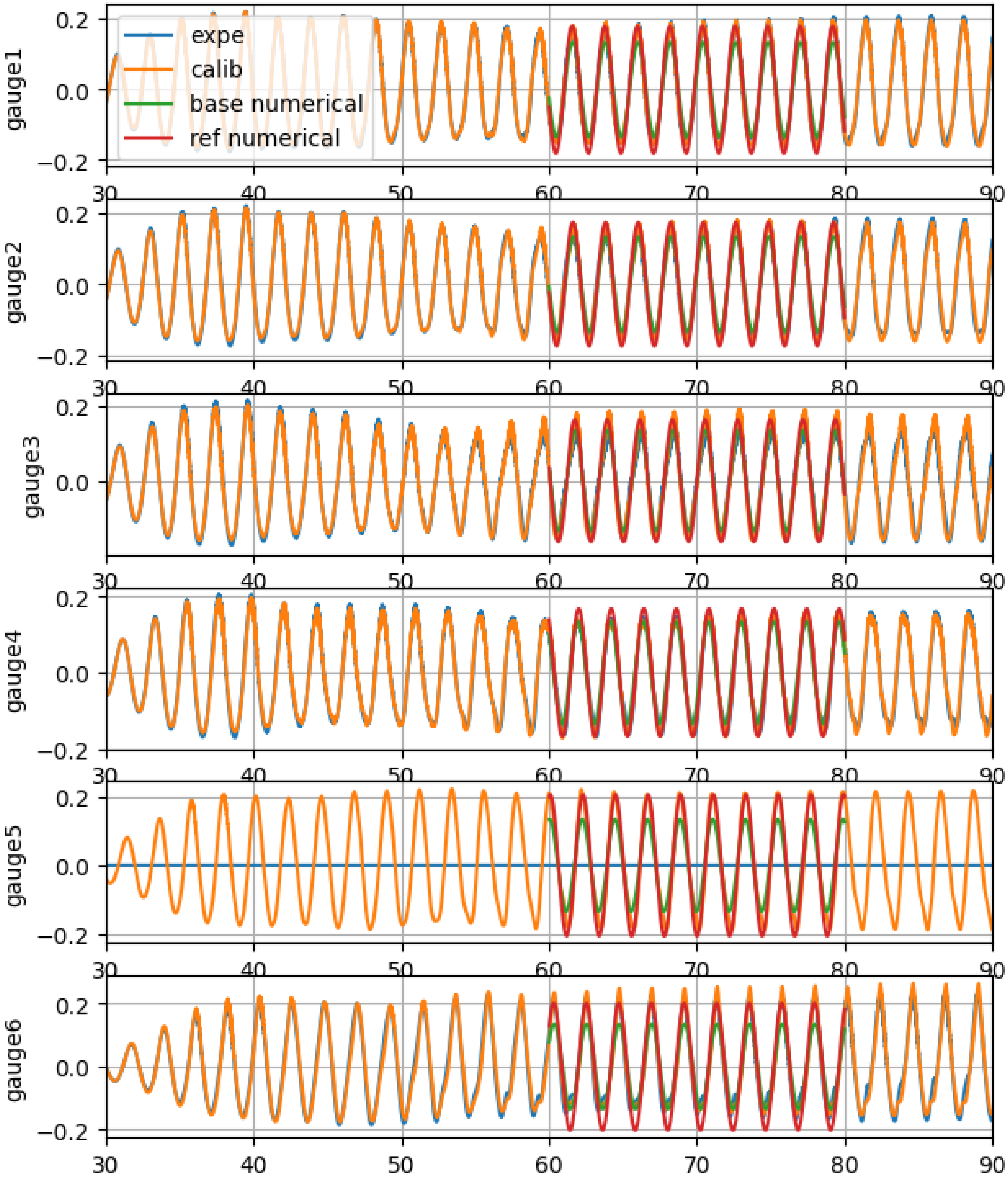

Figure 22 : Wave gauge 1 to 6, test 113. The "ref numerical" is the modelled wave elevation assuming the incident and reflected waves.

This project has received funding from the European Union's Horizon 2020 research and innovation programme under grant agreement No 851885. This output reflects the views only of the author(s), and the European Union cannot be held responsible for any use which may be made of the information contained therein.

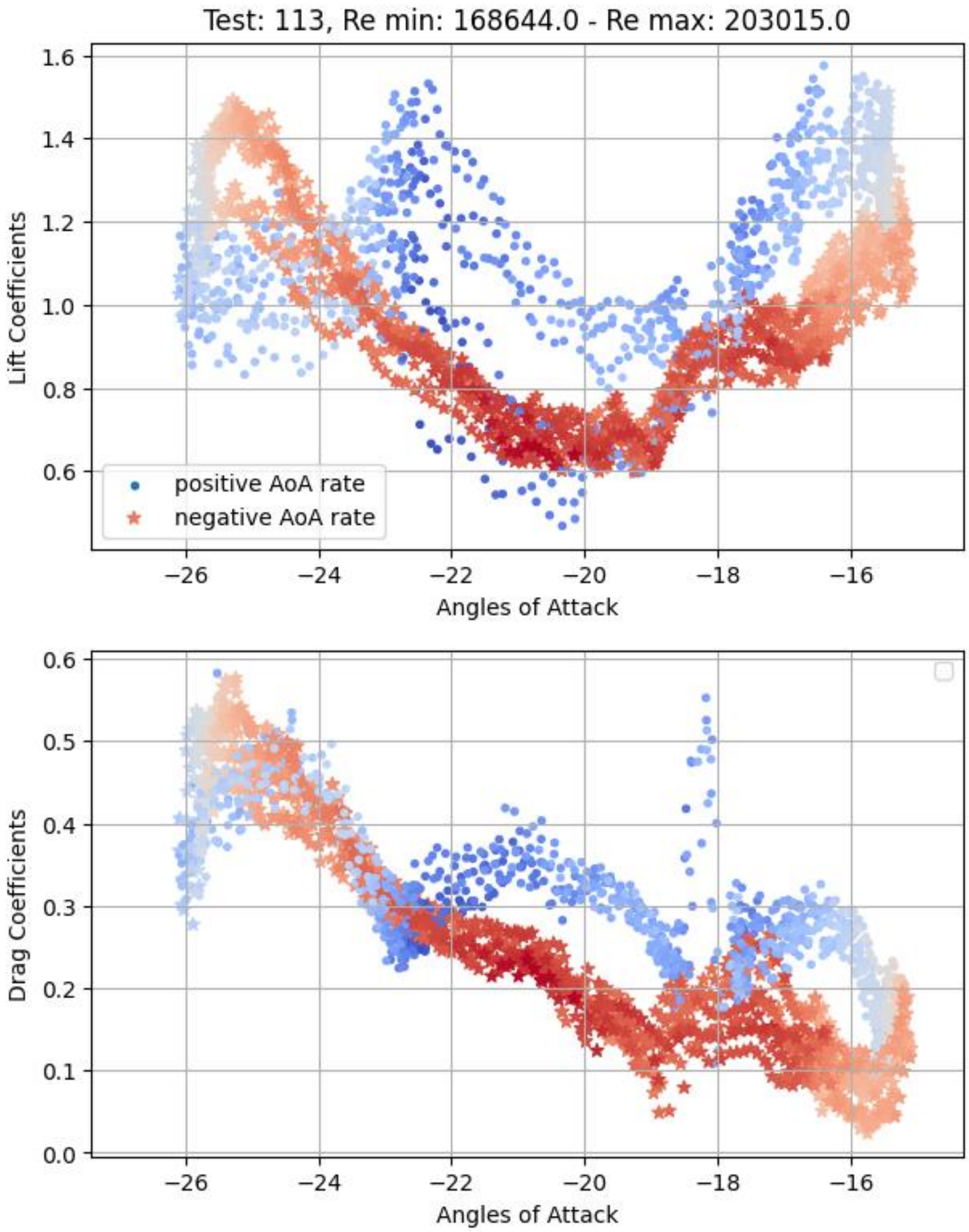

Figure 23: estimated CL and CD coefficients for test 113.

4.2.4 Multiple test results

The Figure 24 shows the results for the tests 108 to 114 (1 foil, 0 deg pitch, regular waves) and for the tests in still water ([60, 134, 135, 165, 173, 174]) with different pitch angles. In those later cases, the AoA is always equal to the pitch angle. Each of the dots is coloured according to the estimated

Reynolds numbers. The black curves (solid and dashed) provide the tabulated coefficient value for the NACA0015 as a reference, for different Reynolds number.

One can observe that the estimated coefficients are roughly following a curve in the [-25 – 0] degree range. However, this curve does not match what could be expected from the tabulated values of the NACA0015. In particular, the lift coefficient do not go down after -10 deg as it could be expected, whereas the drag observed in the experiment is much higher than expected in the [-15 : 0] degree.

The other observation is that there is a large range of Reynolds number, but it is unfortunately correlated with the variation of AoA. It is therefore not possible at this stage to differentiate the variation of coefficients as a function of Reynolds number.

As it is clear from the wave tank data that the tabulated coefficients cannot be applied directly, models are fitted to the data to provide representative values for the global model. For the lift coefficients, the value at 0 deg AoA should be 0, therefore a polynomial model without offset is applied. For the drag coefficients, a polynomial model with an offset is selected. After investigation of different combinations, a third-degree polynomial is chosen for the lift coefficient and a second-degree polynomial for the drag. The models' coefficients are presented on the figure itself. The coefficients are defined from the tests with waves only, but for the offset of the drag polynomial model: a value of 0.0265 was enforced to provide a better match with the values obtained in the still water tests.

It is interesting to see that the coefficients estimated from the still water tests are more or less in adequation with the polynomials obtained from the regular wave results. This provides some degree of validation of the coefficient's models obtained.

4.3 CONCLUSION

The analysis of the coefficients from the 2D tests permits to partially validate the hypothesis underlying the models relying on these coefficients. It appears indeed possible to extract values of C_D and C_L depending on the AoA across a range of test, that will allow to approximate the hydrodynamic loads on the foils. However, these values are not correlated with the tabulated values, and there is a large amount of spread of the values, which will lead to a significant level of errors in the models. The observations of the single test results suggests that some additional phenomena, which are not considered, have a considerable influence, linked to the unsteady nature of the flow (different C_L for positive and negative AoA rate of change for example). Additionally, it remains unclear if the polynomials drawn for the coefficients are valid in other settings, with similar foils but different chord lengths or at different scales.

This project has received funding from the European Union's Horizon 2020 research and innovation programme under grant agreement No 851885. This output reflects the views only of the author(s), and the European Union cannot be held responsible for any use which may be made of the information contained therein.

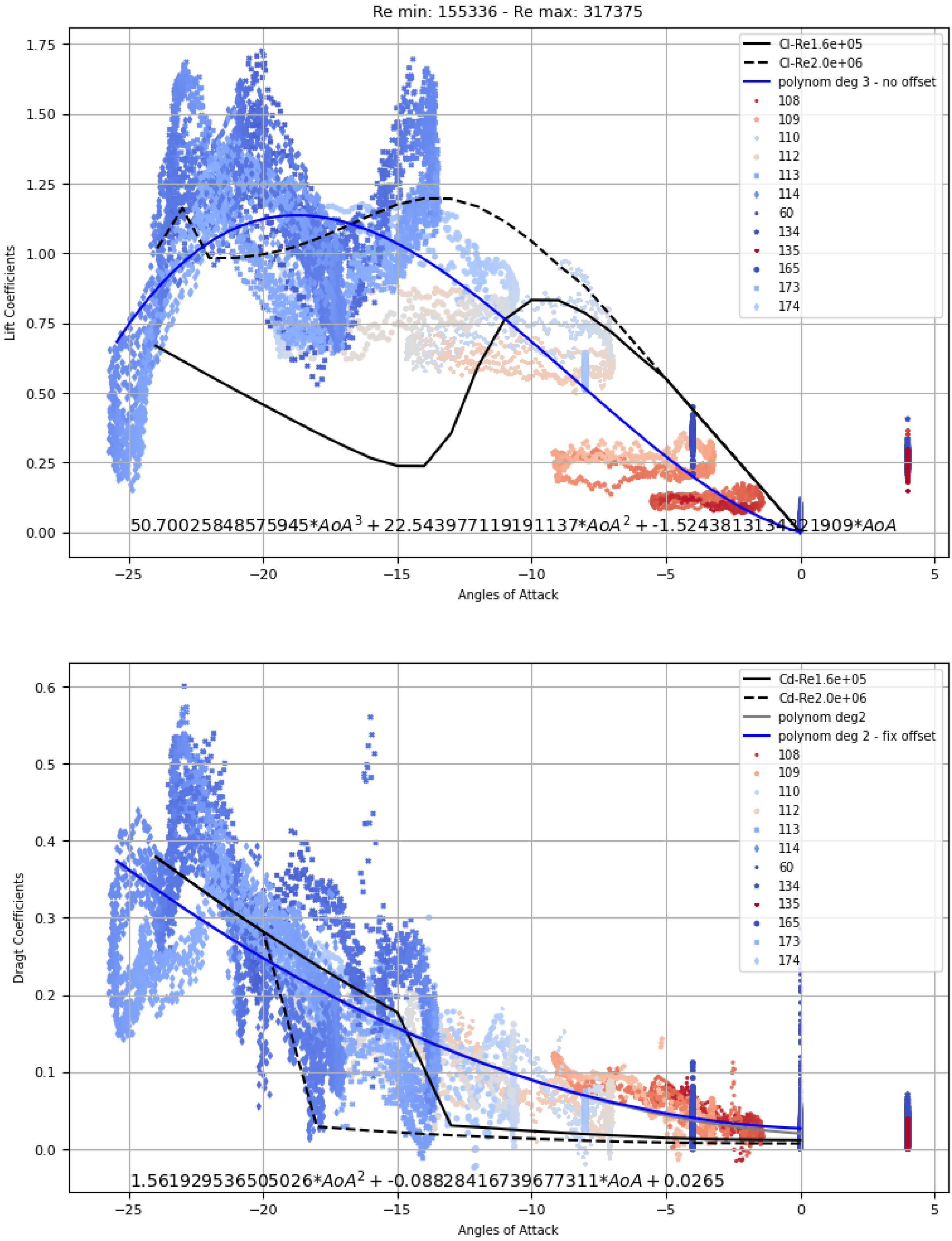

Figure 24 : Cl and CD coefficients extracted from 2D tests

This project has received funding from the European Union's Horizon 2020 research and innovation programme under grant agreement No 851885. This output reflects the views only of the author(s), and the European Union cannot be held responsible for any use which may be made of the information contained therein.

5 VALIDATION OF GLOBAL MODEL

Once the lift and drag coefficients curves characterized, it is therefore possible to estimate the hydrodynamic loads acting on each foil of the rotor. Loads acting on the rotor are also taken into account in the global model, however the rotor shaft size is negligible for the 2D tank tests (see Figure 8), hence it has not been modelled in the validation of the foil modelling.

5.1 HYDRODYNAMIC LOADS ON FOILS

Still water and regular wave tests data realized in ECN are used to validate the hydrodynamic loads acting on the foils. For the moment, the model does not take into account the waves radiated by the foil itself, only drag and lift forces are computed at the 1/4 chord length of the foil.

5.1.1 Model

The LiftWEC configuration and the environmental condition used in the tank tests is reproduced in the OrcaFlex global model.

5.1.1.1 Waves

The incident wave computed in the global model is directly taken from the wave elevation time history of wave gauge number 4 (WG4). When imported in OrcaFlex, the wave elevation is given at a single point. A fast Fourier transform (FFT) is then applied to transform the wave elevation data into several frequency components. Each component is represented by a single Airy wave, and these Airy waves are then combined to give the wave elevation and kinematics at all points (Orcina, OrcaFlex manual).

5.1.1.2 Foils

The foil position and the rotor induced velocity at the foils are respectively deduced from the angular position of the rotor and the rotor speed time history data of the tank tests. The fluid velocity, rotor induced velocity and position of the foil give access to the foil angle of attack. The lift and drag coefficients estimated in Section 4.1 lead then to the lift and drag forces, converted into radial and tangential forces to match the tank test convention (see Figures Figure 10 and Figure 16).

5.1.2 Validation

5.1.2.1 Still water

Tests without incident waves with 0° pitch angle are used to validate the lift and drag coefficients at 0° AoA. Different tests are run with increasing rotor speeds, detailed in Table 6. Radial and tangential forces time series for the different still water tests are given in Figures Figure 25 and Figure 26.

Table 6: Rotor periods for still water tank tests

Test ID	**58**	**59**	**60**	**61**
Period [s]	62,8	6,28	3,14	1,25

This project has received funding from the European Union's Horizon 2020 research and innovation programme under grant agreement No 851885. This output reflects the views only of the author(s), and the European Union cannot be held responsible for any use which may be made of the information contained therein.

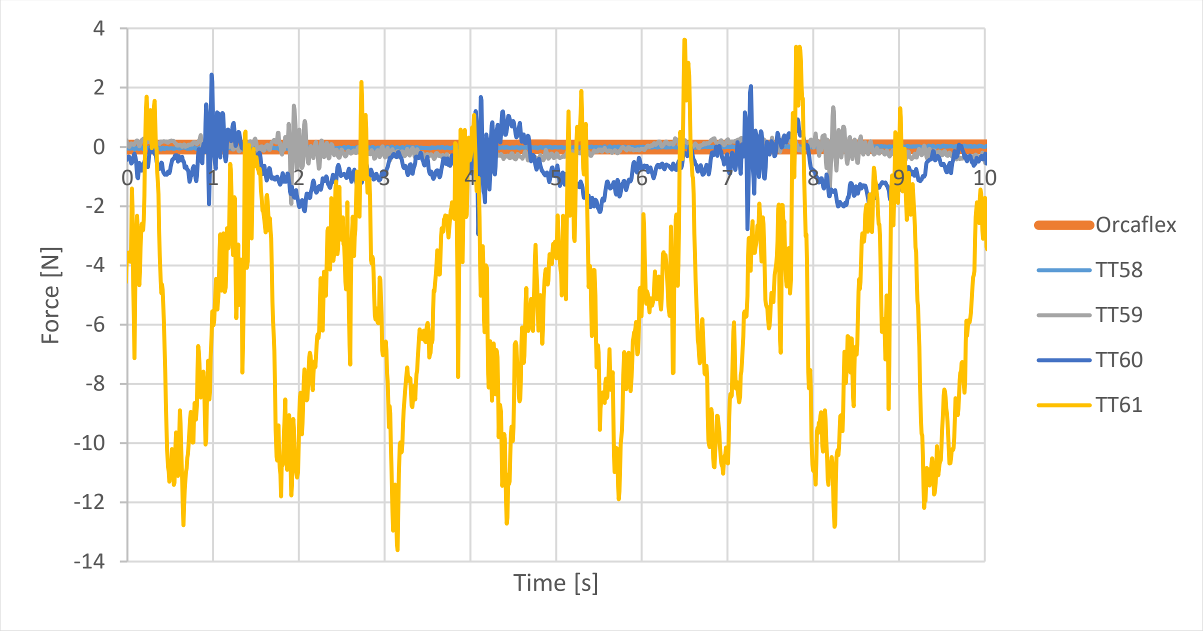

Figure 25: Radial force - still water tests. "TTXX" are the different tank tests ID time series. A single plot of the numerical tests is shown as the 4 tests show similar results (zero radial force)

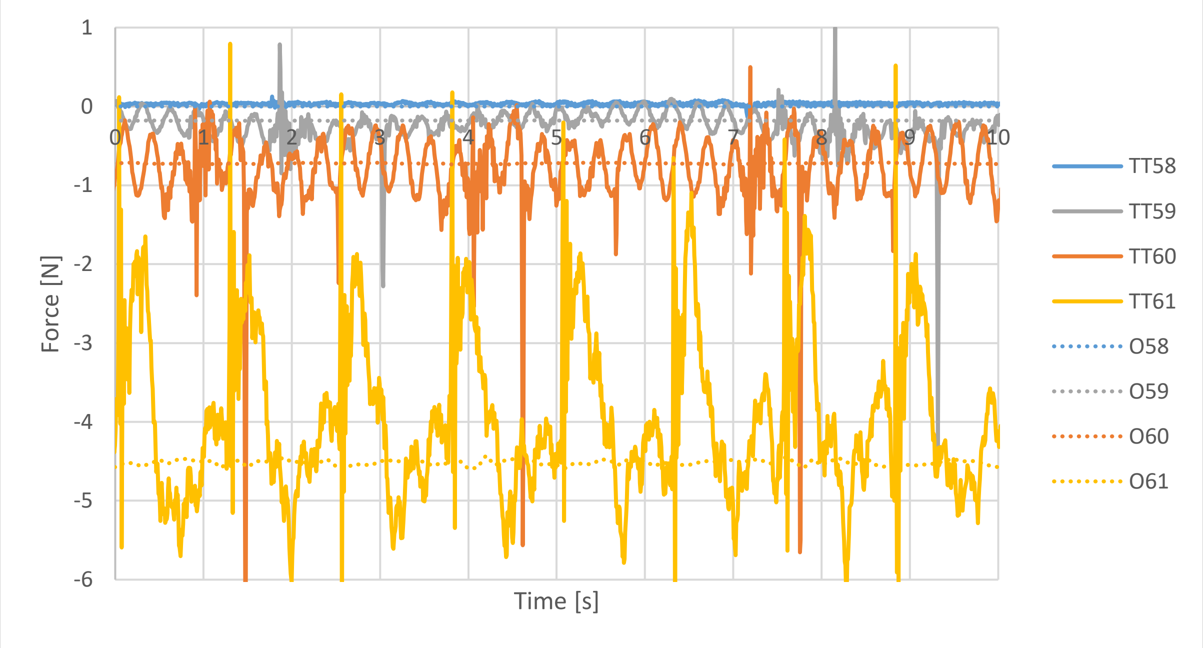

Figure 26: Tangential force - still water tests. "TTXX" are the different tank tests ID time series. "OXX" are the corresponding OrcaFlex global model numerical simulations

Numerical simulations show a zero-radial force, independently from the rotor speed, which is not the case for experimental tests 60 and 61. Big oscillations in the latter two cases might be a consequence of vibrations that becomes not negligible as the rotor rotates at higher speeds. The fact of increasing rotor speed might also increase foil induced waves that are not reproduced in the global model yet.

This project has received funding from the European Union's Horizon 2020 research and innovation programme under grant agreement No 851885. This output reflects the views only of the author(s), and the European Union cannot be held responsible for any use which may be made of the information contained therein.

Tangential force shows also higher oscillations as the rotor speed increases, however, for all the 4 cases the mean tangential force of the numerical is consistent with the experimental mean tangential force.

5.1.2.2 Regular waves

Regular waves tests with a single foil, Foil n°1, are first analysed. The time window analysed starts from the end of the transient step until wave radiation appears. The data duration and wave condition and mean experienced AoA are presented Table 7. In regular waves conditions, the rotor period is equal to the wave period. All the simulations are set to present a phase shift of 90° between the wave crest and the foil 1 (foil 1 phase being advanced of 90°), except cases 108 and 111,.

Test ID	AoA [°]	Wave height [m]	Wave period [s]	Start [s]	End [s]
108	0	0,153	1,42	54	62
111	0	0,31	2	40	60
142	3,5	0,2	1,6	48	56
109	4	0,2	1,6	50	60
110	7	0,253	1,829	43	50
143	7	0,253	1,829	70	80
113	14,2	0,31	2,207	60	70
112	15	0,31	2	39	45
144	15	0,31	2	38	44
114	19,4	0,31	2,462	60	70

Table 7: Regular waves simulations, sorted according to the mean AoA

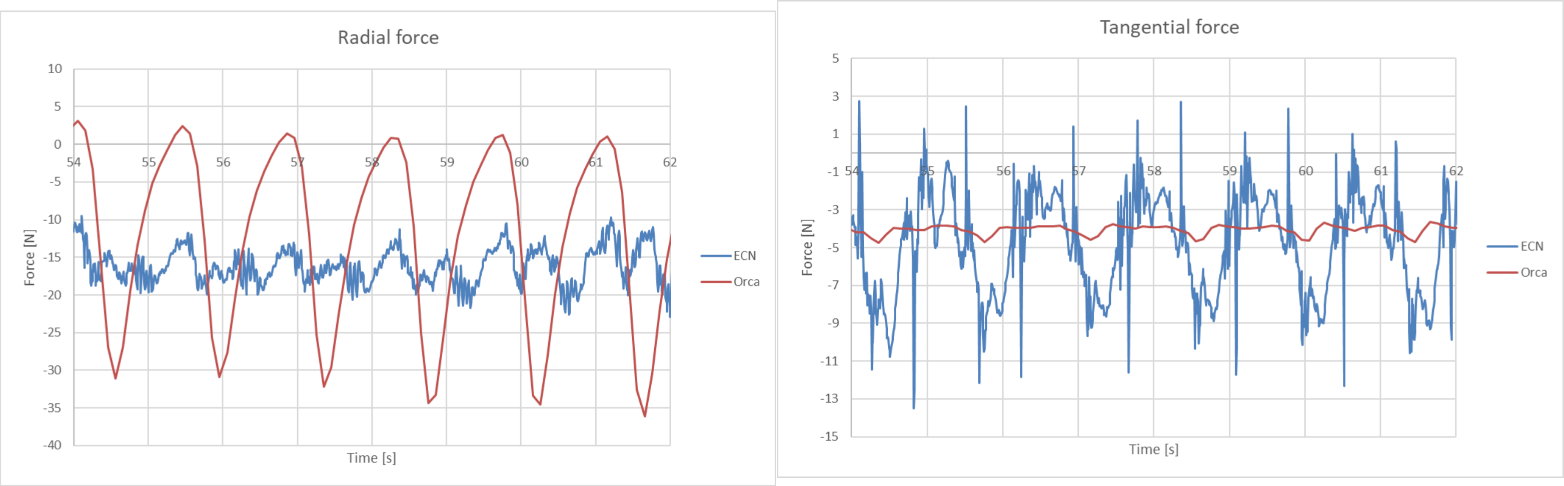

Figure 27: Test 108 – mean AoA 0° - In blue, experimental data, in red numerical global model

This project has received funding from the European Union's Horizon 2020 research and innovation programme under grant agreement No 851885. This output reflects the views only of the author(s), and the European Union cannot be held responsible for any use which may be made of the information contained therein.

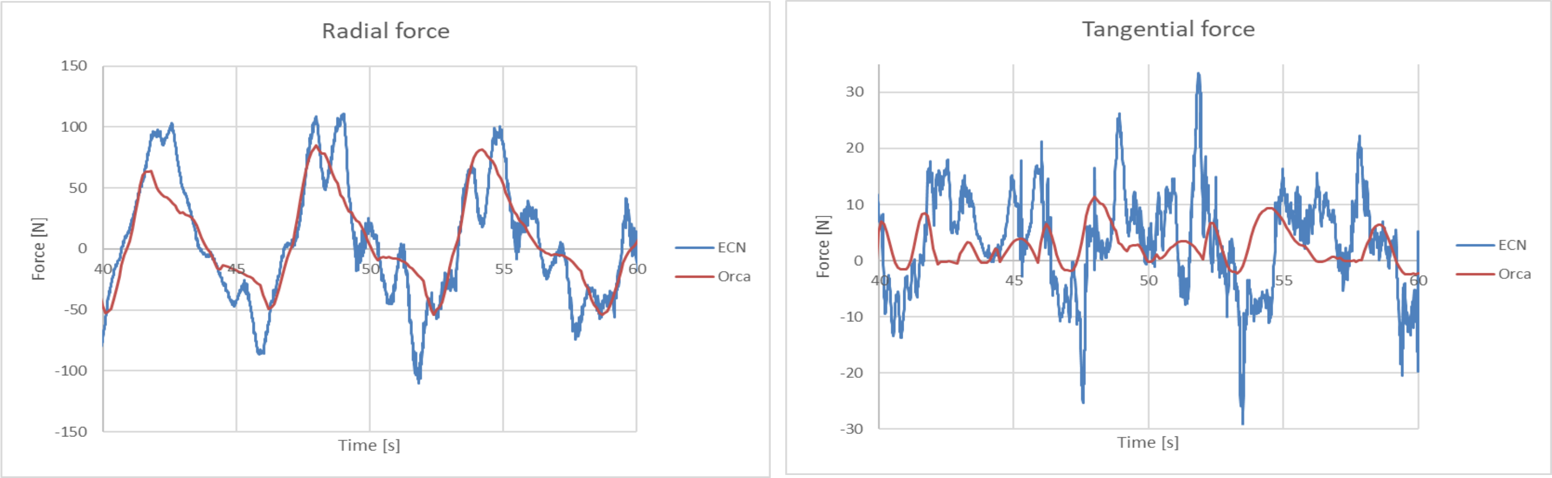

Figure 28: Test 111 - AoA 0° - In blue, experimental data, in red numerical global model

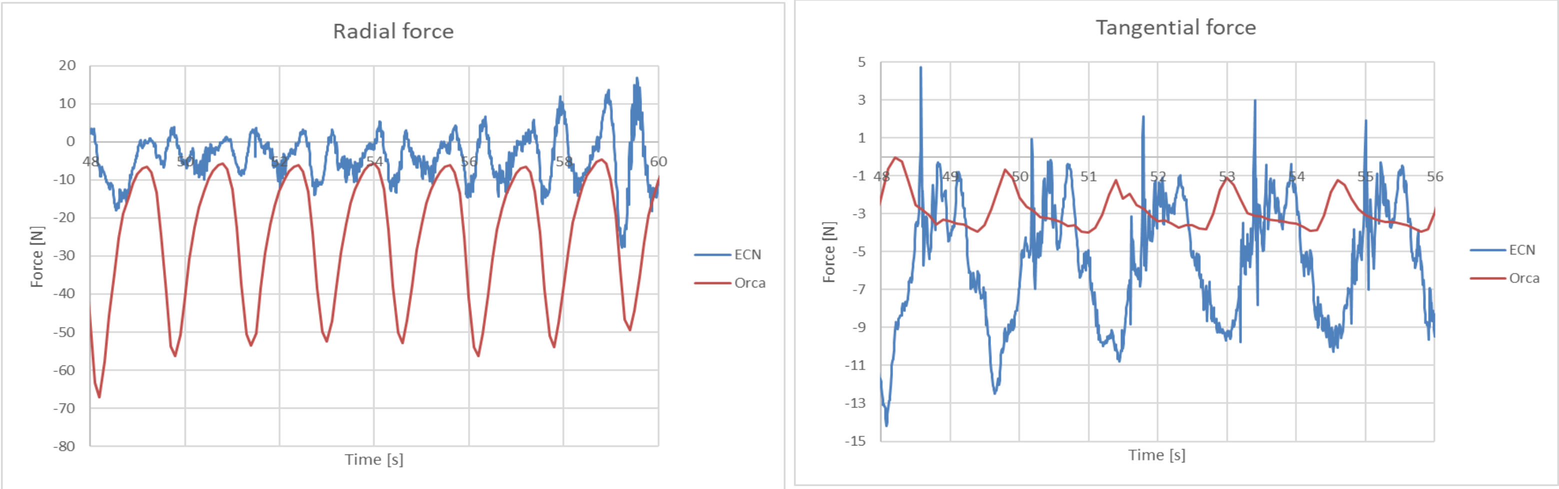

Figure 30: Test 142 - AoA 3.5° - In blue, experimental data, in red numerical global model

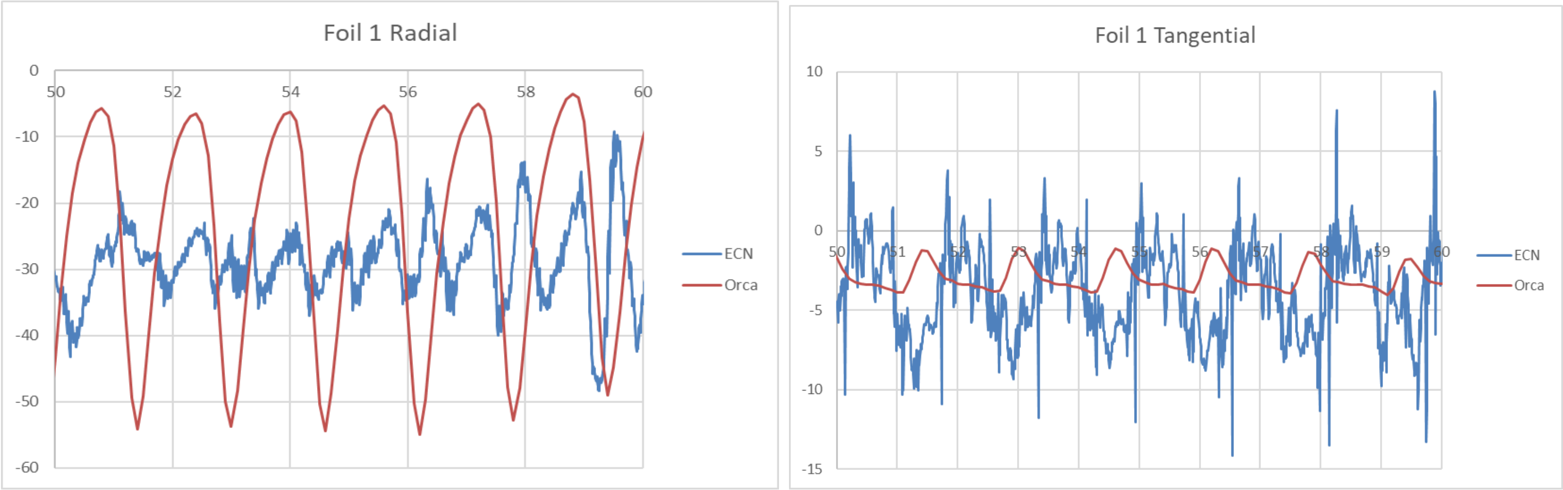

Figure 29: Test 109 - AoA 4° - In blue, experimental data, in red numerical global model

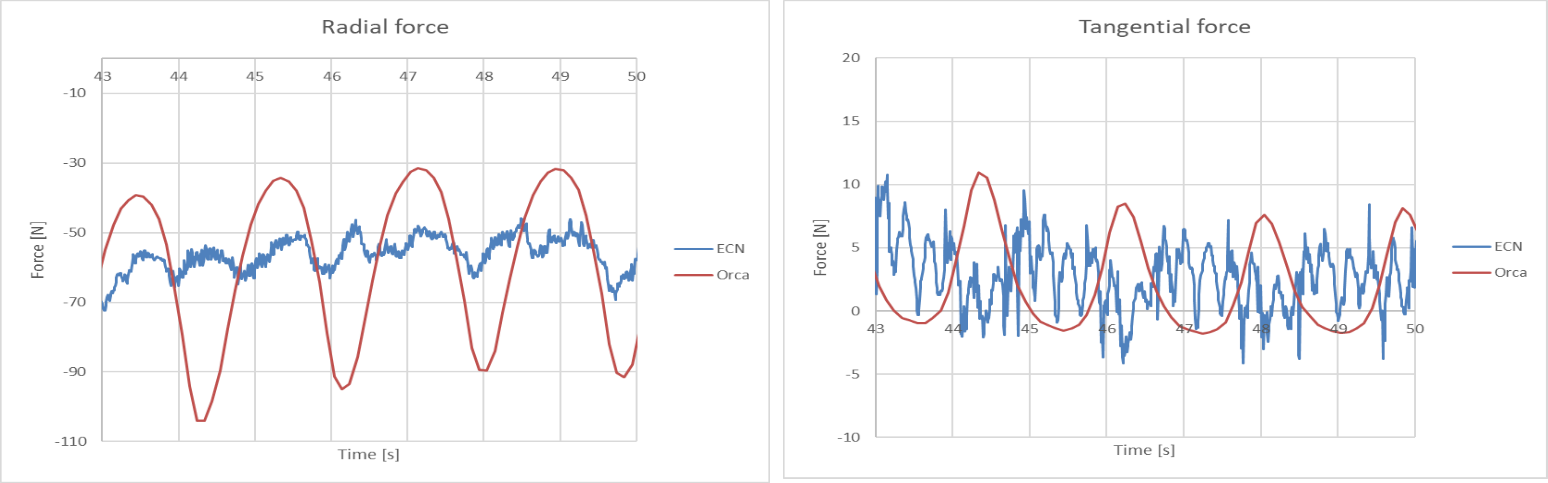

Figure 32: Test 109 - AoA 7° - In blue, experimental data, in red numerical global model

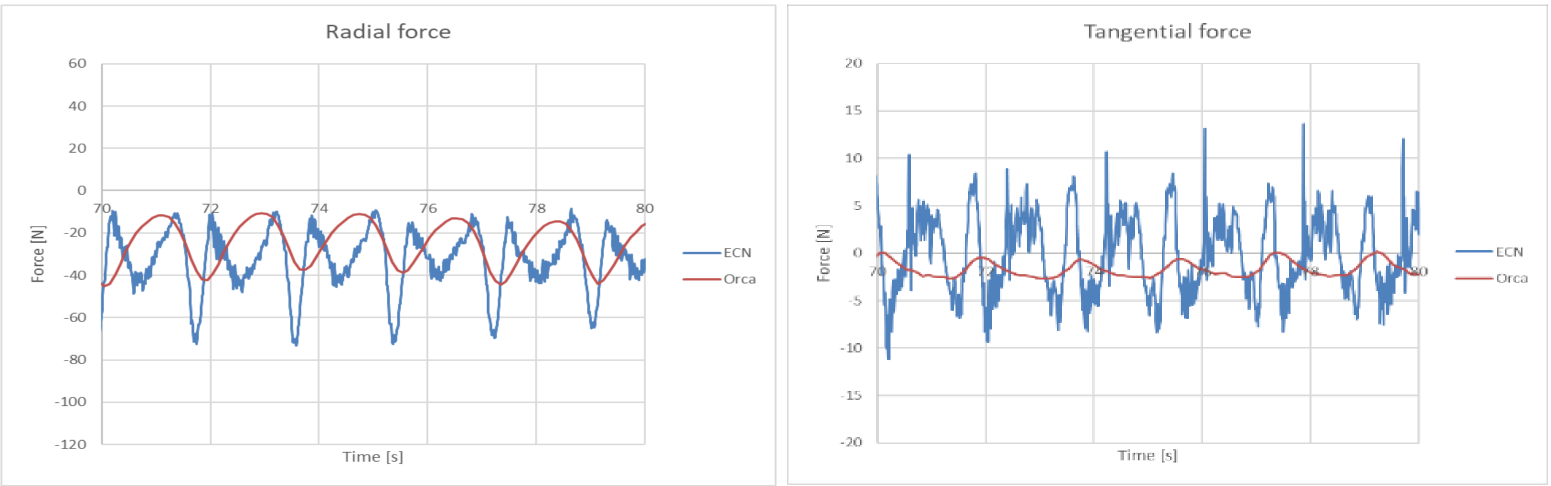

Figure 31: Test 143 - AoA 7° - In blue, experimental data, in red numerical global model

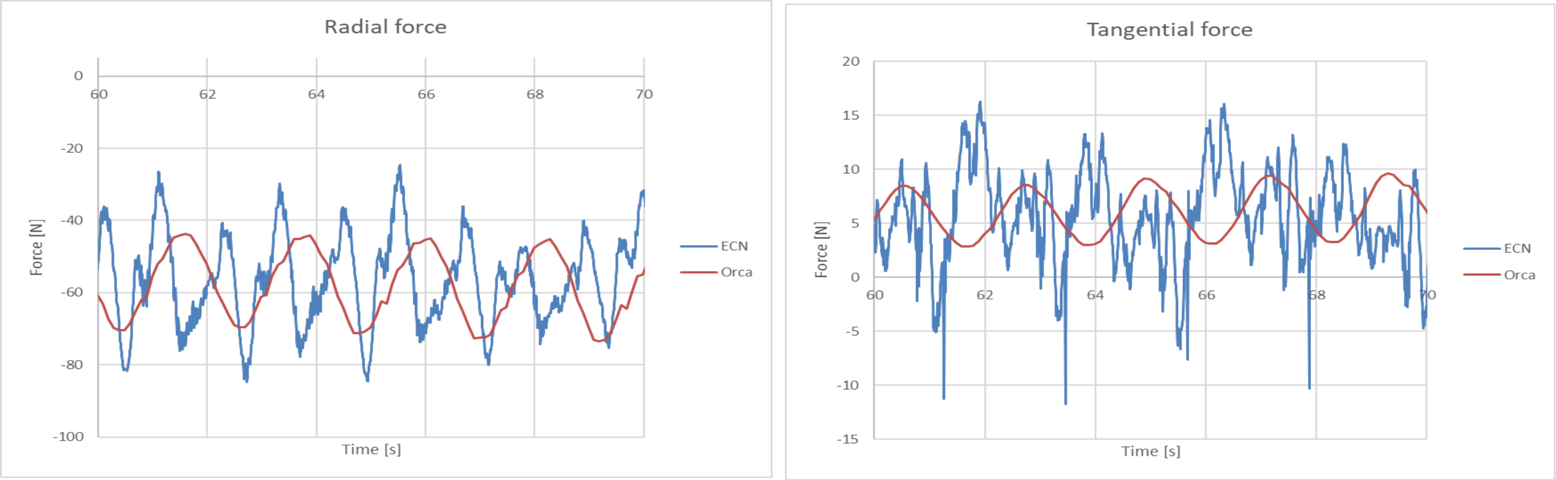

Figure 33: Test 113 - AoA 14.2° - In blue, experimental data, in red numerical global model

This project has received funding from the European Union's Horizon 2020 research and innovation programme under grant agreement No 851885. This output reflects the views only of the author(s), and the European Union cannot be held responsible for any use which may be made of the information contained therein.

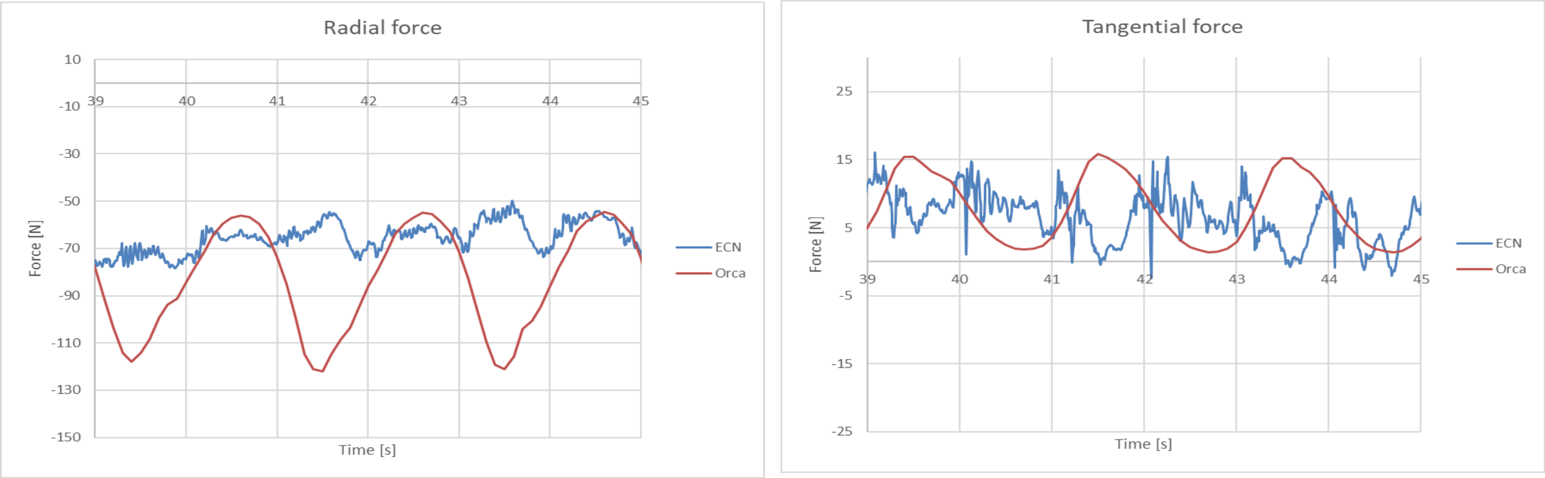

Figure 36: Test 112 - AoA 15° - In blue, experimental data, in red numerical global model

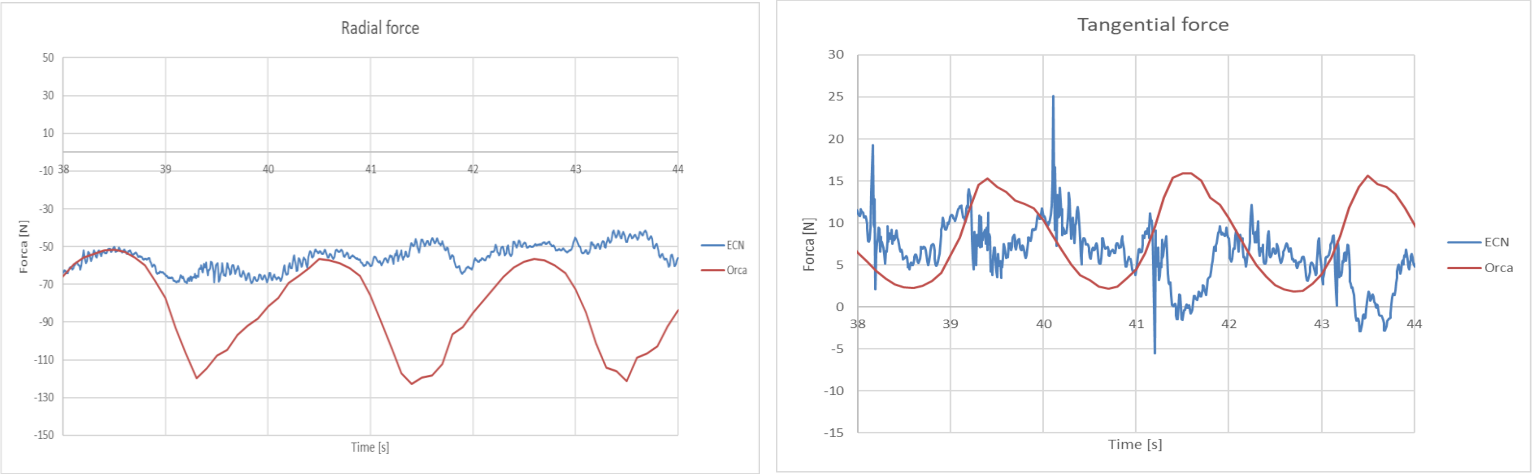

Figure 35: Test 144 - AoA 15° - In blue, experimental data, in red numerical global model

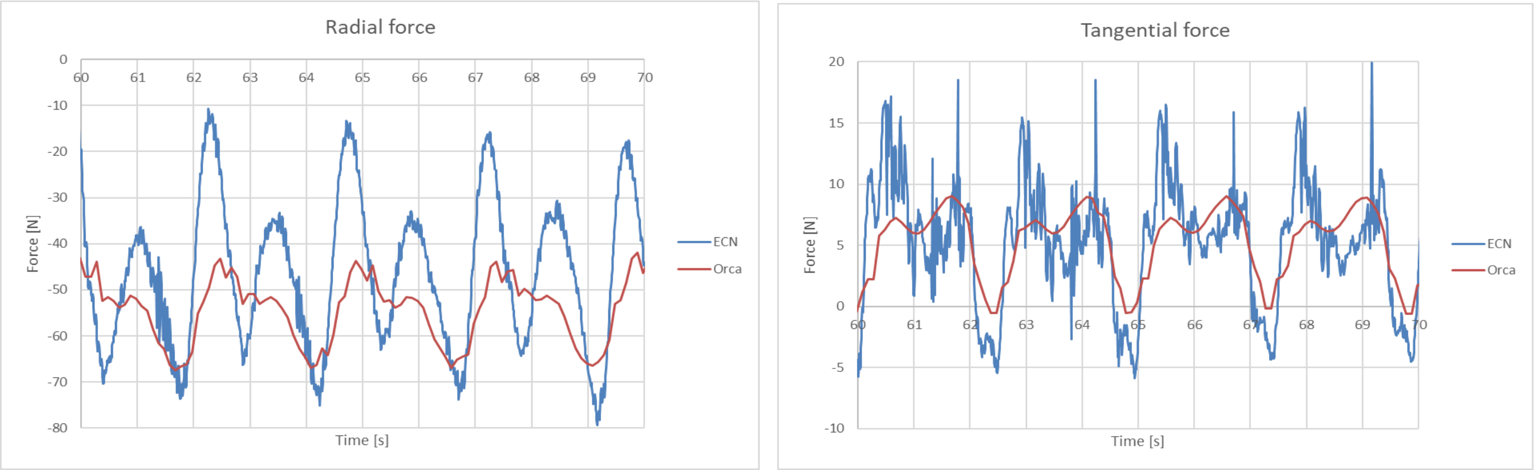

Figure 34: Test 114 - AoA 19.4° - In blue, experimental data, in red numerical global model

This project has received funding from the European Union's Horizon 2020 research and innovation programme under grant agreement No 851885. This output reflects the views only of the author(s), and the European Union cannot be held responsible for any use which may be made of the information contained therein.

Figure 27 to Figure 36 show the radial and tangential forces for a single foil experiencing mean angle of attacks from 0 to 20 degrees. One can see that for the whole range of AoA, the mean radial and tangential fits relatively well to the experimental data; however, the instantaneous peaks are not well represented. This might be explained by the fact the foil induced radiated waves are not taken into account yet in the global model, or by wake effects and vortices that the potential flow theory assumptions neglects. Moreover, the thin airfoil theory is based on static unidirectional flow. The fact of facing a highly dynamic orbital flow environment might not be suitable to catch with accuracy hydrodynamic loads on the foil.

Simulations where the mean AoA is above 15 degrees are producing positive torque most of the time. The global model reproduces better the foil loads behaviour for AoA around 20 degrees, even though the amplitudes of the peaks are lower. This can be explained by the limited range of lift and drag coefficient used for the identification in Section 4.1, the AoA being bounded between [0°; 25°]. The Cl and Cd for AoA above 25° are set equal to the Cl and Cd the 25° AoA.

5.2 HYDRODYNAMIC LOADS ON THE ROTOR SHAFT

5.2.1 Model

We assume the rotor geometry being a horizontal cylinder submerged beneath the free surface, oriented perpendicularly to the waves. The potential spinning effect is not considered in the computation. Hydrodynamic loads on the shaft are computed using Ogilvie's 2D analytical potential flow model (Ogilvie, 1963) and computes the excitation force amplitude and phase, mean drift force, added mass and radiation damping. The hydrodynamic parameters are then directly imported in the OrcaFlex global model.

To validate the model, hydrodynamic parameters of the rotor shaft are compared to the hydrodynamic parameters of the potential flow code OrcaWave. Environmental and geometric properties of the rotor shaft for model validation are shown in Table 8.

Wave type	Airy waves	-	Water depth	d	infinite
Wave height	H_s	1 m	Period	T_p	10 s
Gravity	g	9.81 $\mathrm{m/s^2}$	Water density	rho	1025 $\mathrm{kg/m^3}$
Submergence	h	10 m			
Length	h	20 m	Rotor radius	R_r	1.5 m

Table 8: Environmental and geometric parameters for rotor shaft model validation

5.2.2 Validation

Figures Figure 37 to Figure 41 shows the hydrodynamic parameters obtained with the global model and OrcaWave.

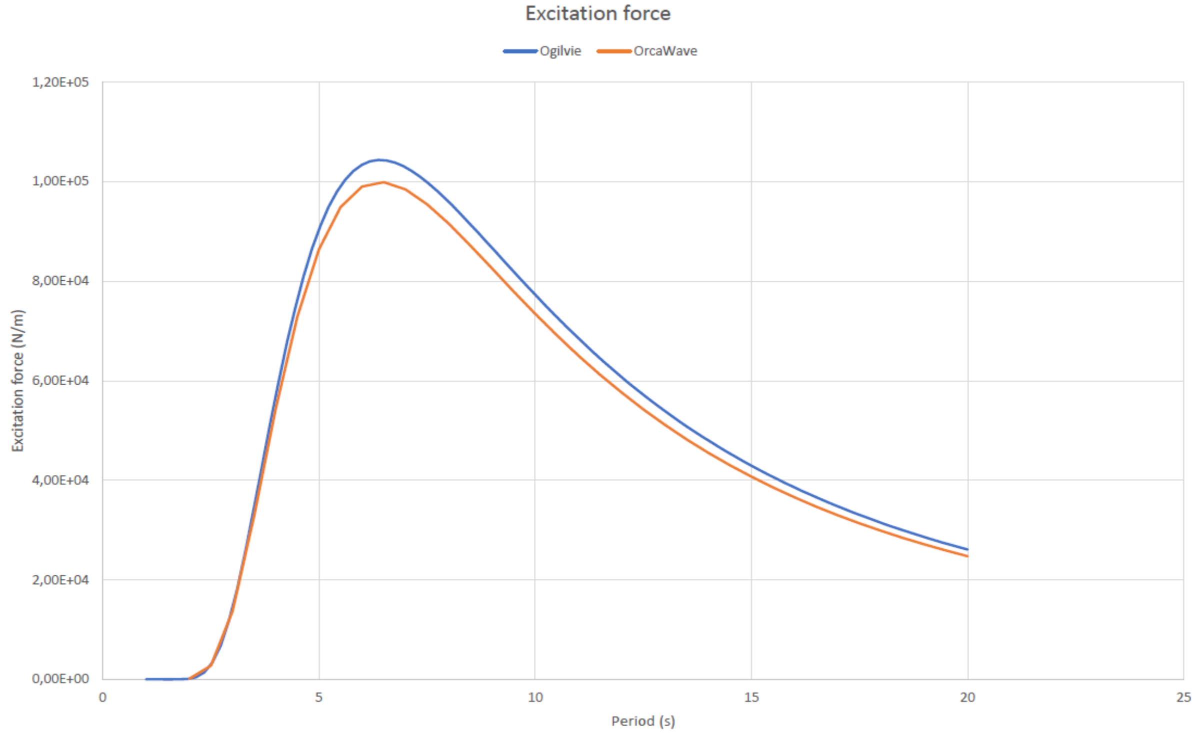

Figure 37: Excitation force amplitude of a submerged horizontal cylinder. In blue, global model results based on (Ogilvie, 1963)*, in orange, OrcaWave results*

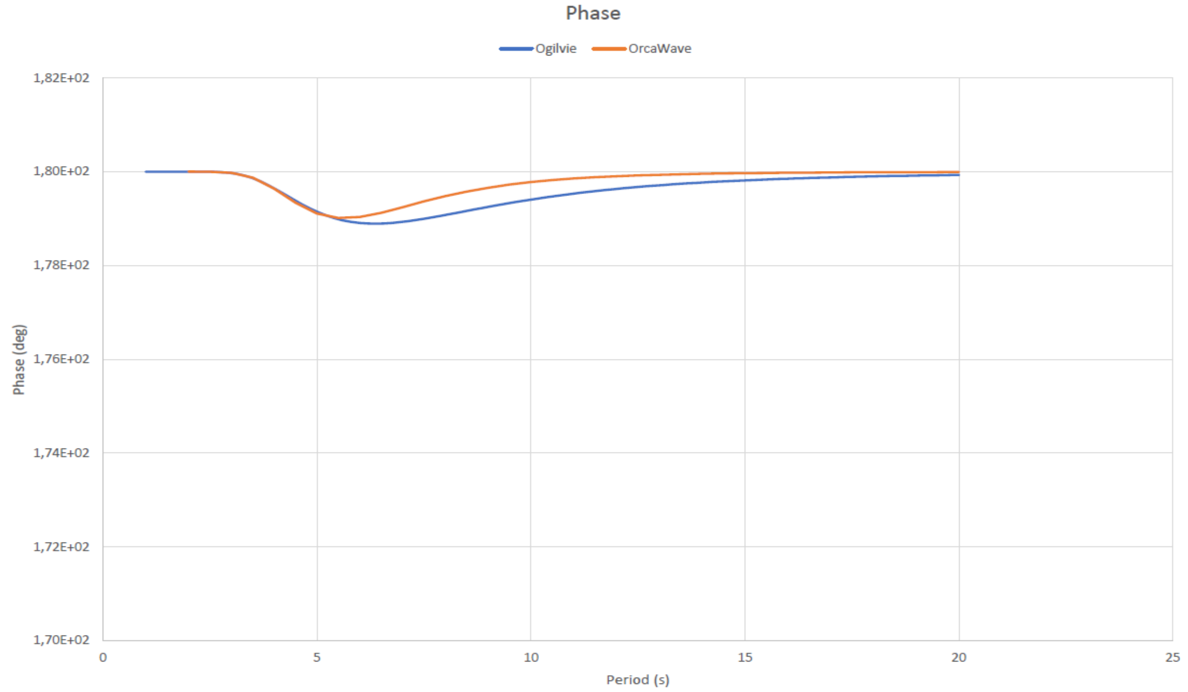

Figure 38: Excitation force phase of a submerged horizontal cylinder. In blue, global model results based on (Ogilvie, 1963)*, in orange, OrcaWave results*

This project has received funding from the European Union's Horizon 2020 research and innovation programme under grant agreement No 851885. This output reflects the views only of the author(s), and the European Union cannot be held responsible for any use which may be made of the information contained therein.

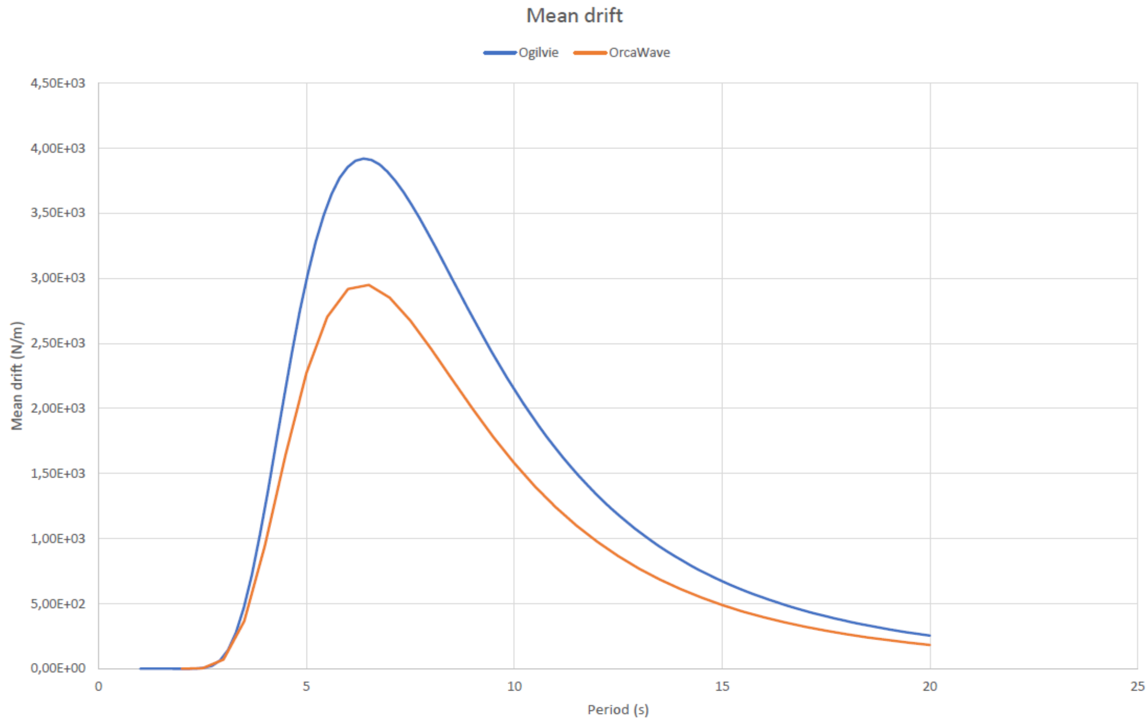

Figure 39: Mean drift of a submerged horizontal cylinder. In blue, global model results based on (Ogilvie, 1963)*, in orange, OrcaWave results*

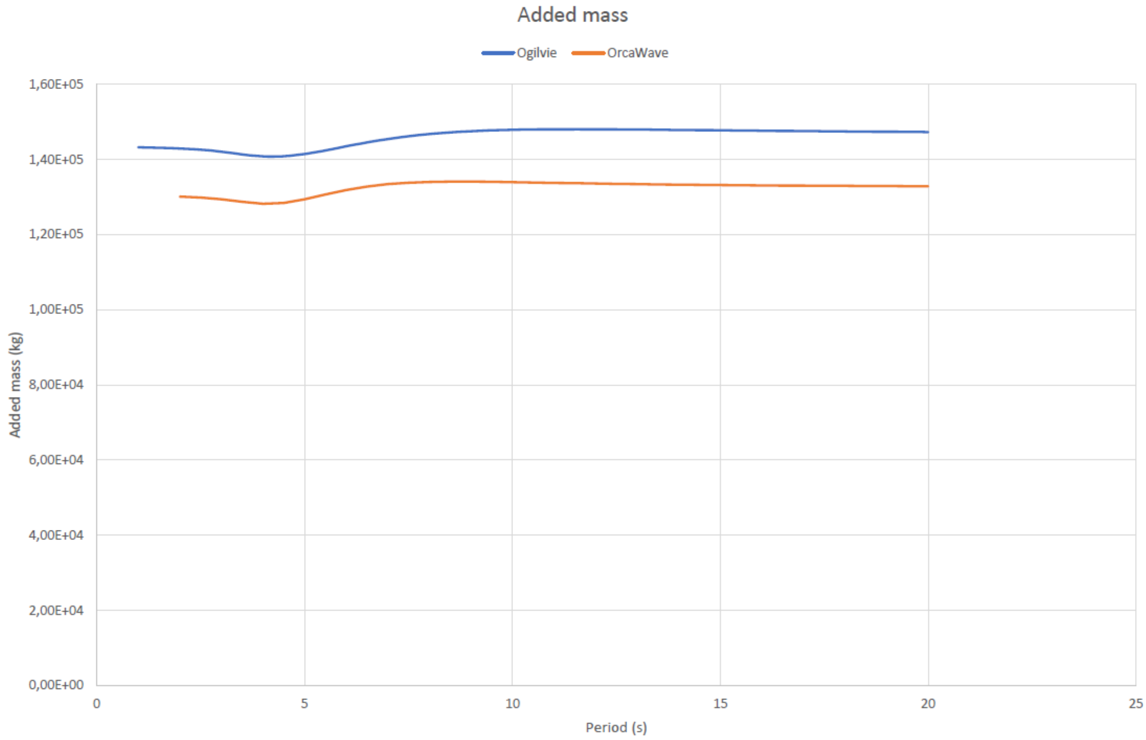

Figure 40: Added mass of a submerged horizontal cylinder. In blue, global model results based on (Ogilvie, 1963)*, in orange, OrcaWave results*

This project has received funding from the European Union's Horizon 2020 research and innovation programme under grant agreement No 851885. This output reflects the views only of the author(s), and the European Union cannot be held responsible for any use which may be made of the information contained therein.

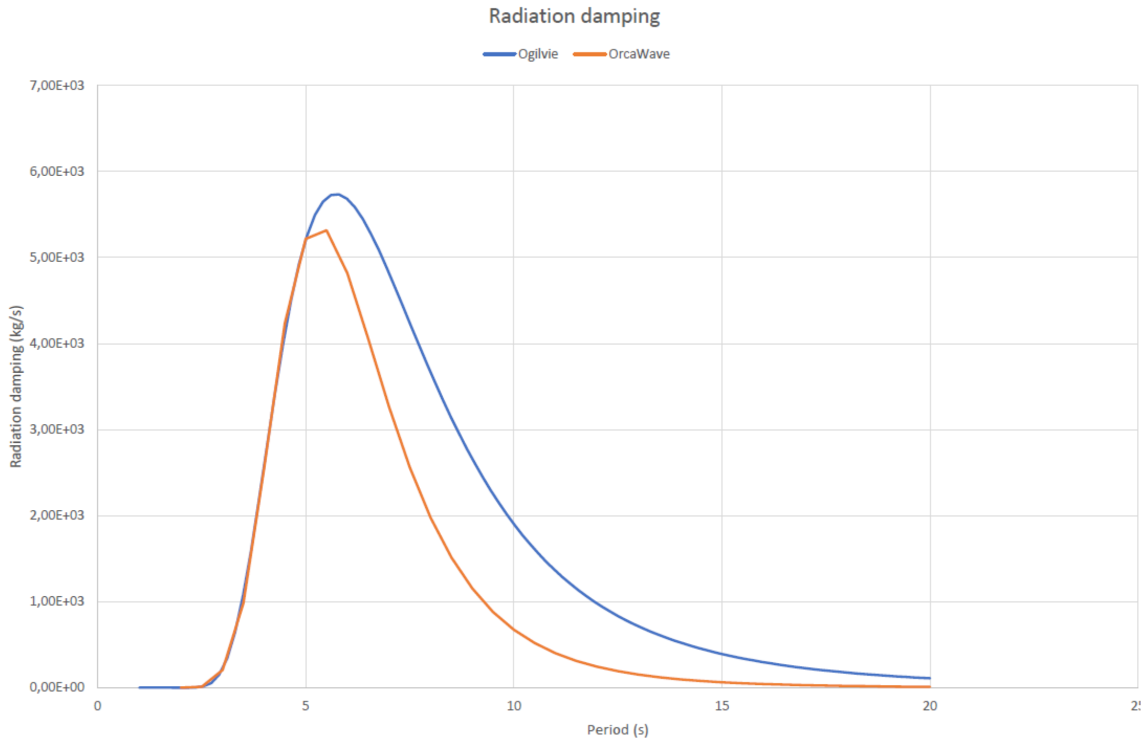

Figure 41: Radiation damping of a submerged horizontal cylinder. In blue, global model results based on (Ogilvie, 1963)*, in orange, OrcaWave results*

The 2D model analytical model tends to overestimate hydrodynamic parameters over the 3D potential code results. There are some differences regarding the added mass, radiation damping and mean drift, but there is still a good agreement between 2D and 3D models. On the other hand, the excitation force amplitude and phase fit well. The analytical 2D model computation is very fast - a hydrodynamic database for a given rotor shaft diameter and submergence is available in a few seconds - and appears to be accurate enough for the global model.

6 VALIDATION OF CFD MODEL

The validation of the CFD model is divided into five sections, which present results for 5 studies conducted during the test campaign:

1. A single foil rotor in calm water at constant rotational speed
2. A single foil rotor in calm water at varying rotational speed
3. A double foil rotor in calm water at constant rotational speed
4. A single foil rotor in regular waves at constant rotational speed
5. A double foil rotor in regular waves at constant rotational speed

This project has received funding from the European Union's Horizon 2020 research and innovation programme under grant agreement No 851885. This output reflects the views only of the author(s), and the European Union cannot be held responsible for any use which may be made of the information contained therein.

6.1 EXPERIMENTAL INVESTIGATIONS OF ROTOR IN CALM WATER

6.1.1 Wave radiation of single foil rotor

In this setting, a single foil is attached to the rotor. In this experimental series, the pitch angle of the respective foil is fixed on a run-basis. No incident waves are present in these cases. Since no external wave is generated and hence no energy can be absorbed, the rotor is driven by the torque motor in all of these tests. Due to the interaction with the free surface, a fluctuation of the inflow angle experienced by the foil is induced over each cycle. The pitch is varied in between test runs, leading to different magnitudes and signs of tangential and radial loading.

6.1.1.1 Constant rotational velocity

In these tests runs, the rotor is spun at constant rotational velocity. In both the numerical simulation, as well as in the experimental test, the rotor is accelerated from zero velocity up to the target rotational velocity over several rotation cycles.

A comparison of experimental and numerical runs is done based on the force sensor measurements of the experiment and the integral of surface forces over the foils in the numerical simulations. In all force signals, it can be observed that an oscillation of the force signals at rotation frequency occurs. With increasing time, the influence of this oscillation decreases and the time-varying force measurements indicate an increasingly chaotic inflow as experienced by the foil. Figure 42 shows a synchronized time series of the tangential forces for case 102, of a single foil at $\varphi = 0°$, rotated at $\omega = 2\frac{rad}{s}$. As can be seen, the mean values of both forces coincide will, while both signals show strong high-frequent oscillations (see also Figure 44 and Figure 45). The peaks measured during the experiment (blue) show stronger fluctuations than the numerical results (orange).

Figure 43 shows the radial force time series for run 102. While both time series exhibit strong cyclical oscillations of the force, the amplitudes of the numerical results are larger. The mean values are of opposite sign. However, the pitch angle in this case is $\varphi = 0°$ and when converted into non-dimensional values, radial force coefficients are in the order of magnitude of $O(c_{rad1}) = 0.01$. Differences of this magnitude can be expected to be within experimental uncertainty. This hypothesis is supported by other measurements of a single foil at zero-pitch in calm water, which also resulted in negative mean radial force values (e.g. case 61).

The higher amplitude of force fluctuations in the RANS model is likely due to disturbances of foil inflow. The source of these disturbances lies in the build-up of vortex structures in the foil wake. Small disturbances in the foil boundary layer lead to an asymmetric development of the foil wake. This causes the wake to form small vortex structures. During the next passage of the foil, these structures induce a momentary change in inflow on the foil, causing a deflection of the wake, which leads to a reoccurrence of the effect in subsequent motion cycles.

This project has received funding from the European Union's Horizon 2020 research and innovation programme under grant agreement No 851885. This output reflects the views only of the author(s), and the European Union cannot be held responsible for any use which may be made of the information contained therein.

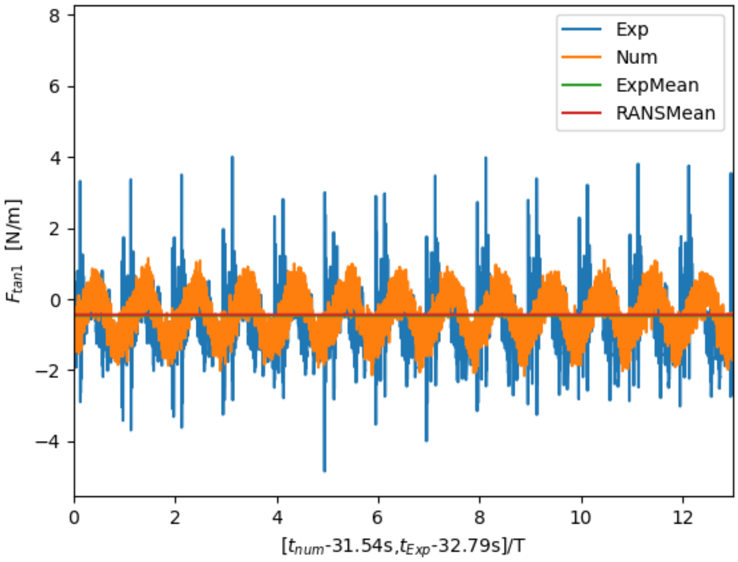

Figure 42: Case 102, Tangential force on foil No°1 at 0.25c over time, $\varphi = 0°, \omega_r = 2\frac{rad}{s}$

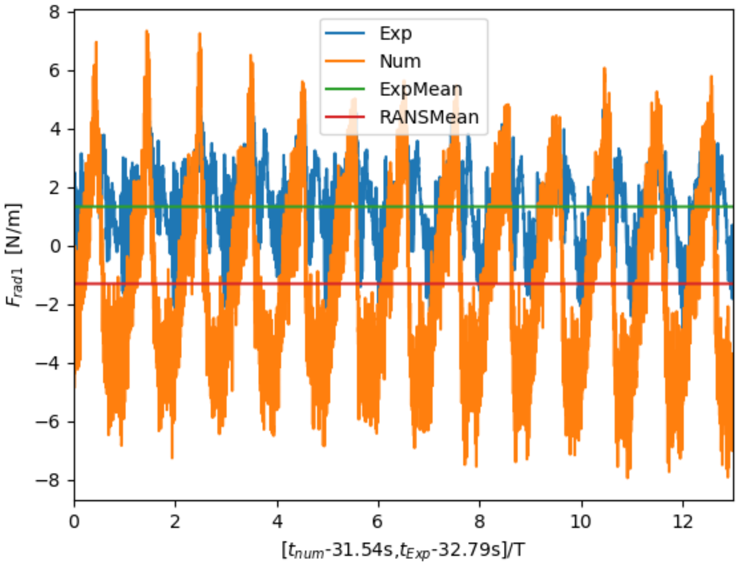

Figure 43: Case 102, Radial force on foil No°1 at 0.25c over time, $\varphi = 0°, \omega_r = 2\frac{rad}{s}$

This project has received funding from the European Union's Horizon 2020 research and innovation programme under grant agreement No 851885. This output reflects the views only of the author(s), and the European Union cannot be held responsible for any use which may be made of the information contained therein.

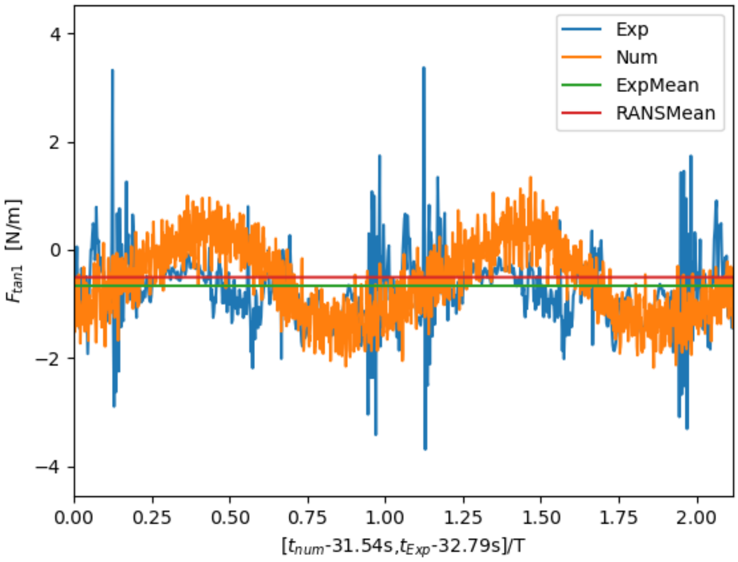

Figure 44: Case 102, Tangential force on foil No°1 at 0.25c over time, focus on single rotation cycle. $\varphi = 0°, \omega_r = 2\frac{rad}{s}$

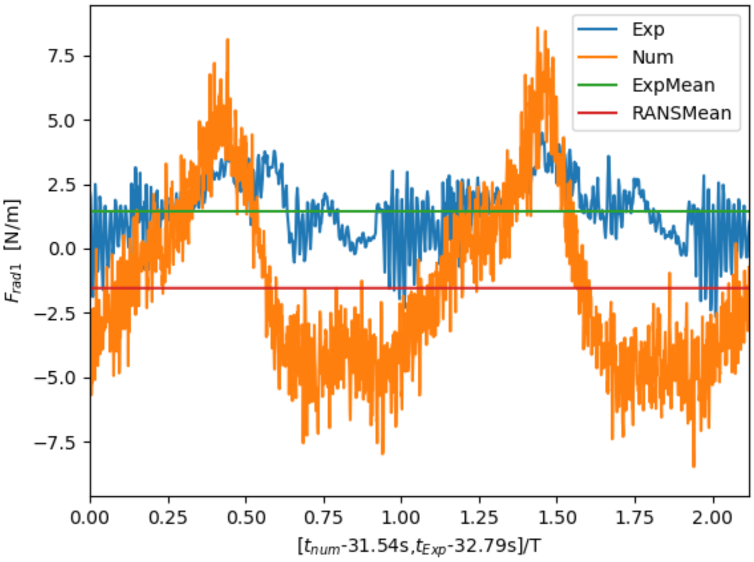

Figure 45: Case 102, Radial force on foil No°1 at 0.25c over time, focus on single rotation cycle. $\varphi = 0°, \omega_r = 2\frac{rad}{s}$

The strength of this effect increases until an equilibrium between the creation of these vortices by the foil and the dissipation of the vortex structures due to the accumulation of turbulent kinetic energy is reached. For most cases it was found, that the strength of the vortices and the corresponding induced fluctuations of foil forces seemed significantly larger in the numerical simulation. This is likely due to the 2D nature of the simulation and the quasi-2D nature of the experiment. In a pure 2D-environment, vortex structures are significantly more stable than in 3D.

These fluctuations of the force signals, despite showing significant influence on instantaneous forces, seem to have only a small effect on the mean forces in radial and tangential direction. Figure 46 and Figure 47 show the mean forces in radial and tangential direction for different rotation rates over different pitch angles in the experimental coordinate system. It can be seen that when considering forces at mid-chord position, the mean tangential force can become positive, which might be wrongly interpreted the rotor being driven through the interaction with the free surface. However, the shaft torque is the sum of tangential force times radius and foil pitch moment, which depends on the point of evaluation. If the evaluation point is far from the centre of circulation (typically close to quarter-chord), the moment becomes large and can offset the apparently positive tangential force.

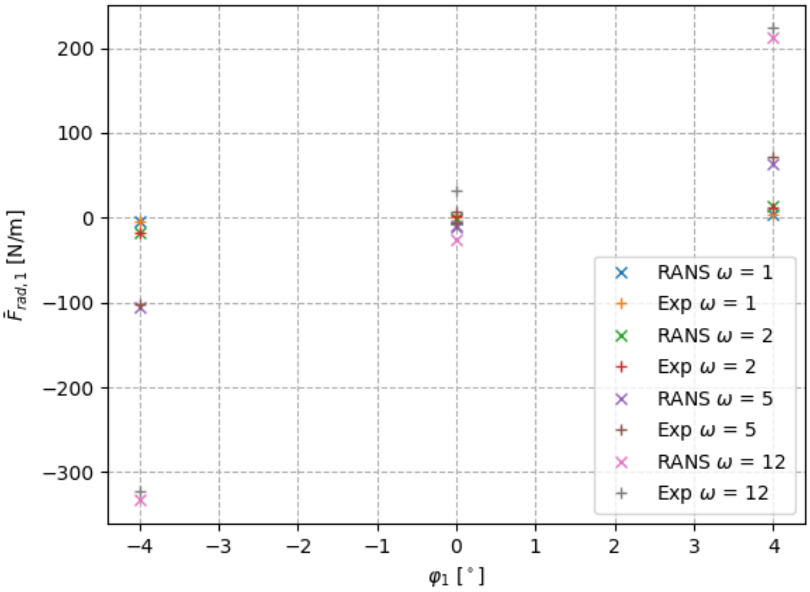

Figure 46: Mean radial forces on foil No°1 for different rotation rates over varying pitch angles. Values given in experimental frame of reference.

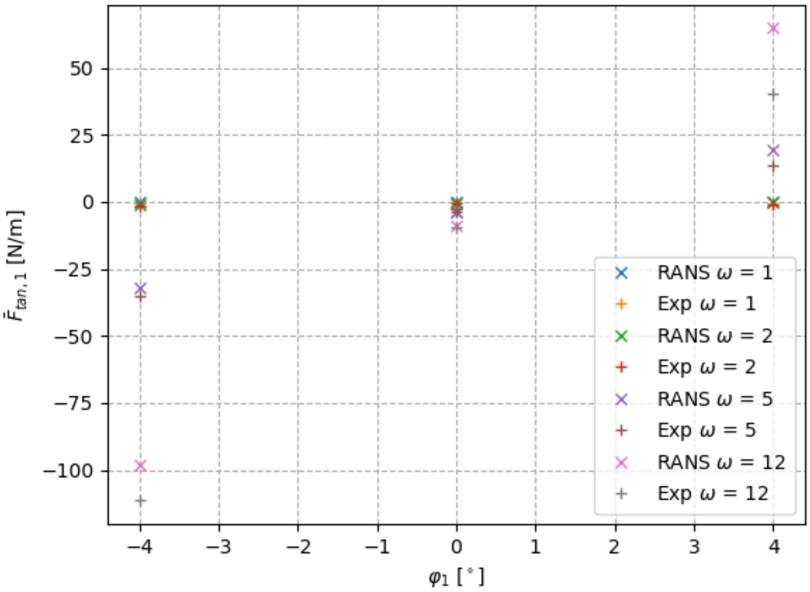

Figure 47: Mean tangential forces on foil No°1 for different rotation rates over varying pitch angles. Values given in experimental frame of reference.

When comparing the numerical and experimental values, the results show good agreement of mean radial forces measured at half-chord position for all rotation rates and pitch angles, with deviations $< 10\%$ across all test runs. For the tangential force results, it can be seen that deviations become larger for cases with non-zero pitch angles. This effect becomes more apparent when plotting the results in terms of force coefficients over ω, as shown in Figure 48 and Figure 49.

$$c_{tan} = \frac{F_{tan}}{\frac{1}{2}\rho(\omega r)^2 c}, \qquad c_{rad} = \frac{F_{rad}}{\frac{1}{2}\rho(\omega r)^2 c} \tag{35}$$

These results show that for non-zero pitch angles, the deviation between experimental and numerical tangential force coefficient appears systematic. One possible explanation lies in the correction for the centrifugal force. As shown in section 3.2, due to the definition of experimental coordinate system and location of CoG and attachment point, the influence of centrifugal effects on the half-chord tangential force is non-zero. The correction for this non-zero influence is conducted based on dry testing at $0°$ pitch. Although theoretically, the change in centrifugal effects introduced by a change in pitch by $\pm 4°$ should be small, it is possible that secondary effects due to removal and reinstallation of the device may be the cause of this effect. Unfortunately, no dry tests for non-zero pitch angles are available for direct comparison.

In Figure 48 it can also be observed that the sign of the radial force coefficient differs between experimental and numerical results for $0°$ pitch angle, as was previously discussed for the force signal time series of case 102. This is likely within the experimental uncertainty, since total radial forces are close to zero. This effect is also observed for foils in straight flight, where small deviations from zero lift occur for zero pitch settings of a symmetrical foil.

This project has received funding from the European Union's Horizon 2020 research and innovation programme under grant agreement No 851885. This output reflects the views only of the author(s), and the European Union cannot be held responsible for any use which may be made of the information contained therein.

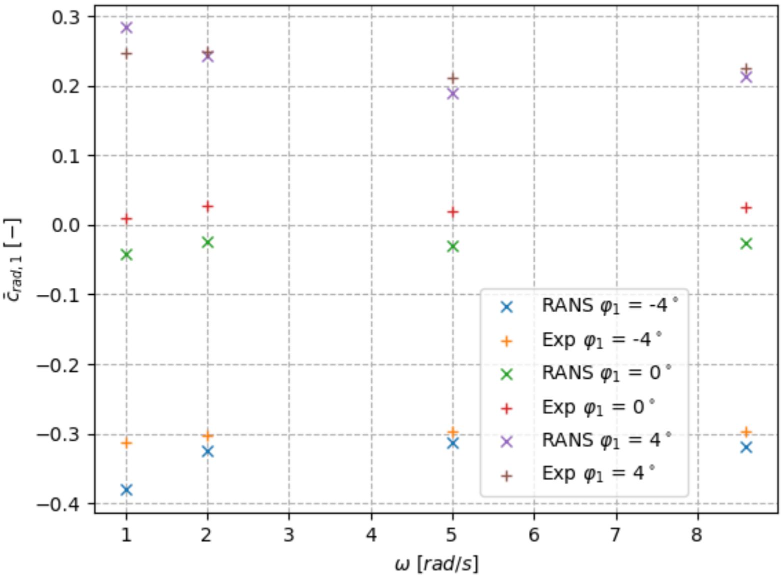

Figure 48: Mean radial force coefficient of foil No°1 for different varying pitch angles over rotation rates. Values given in experimental frame of reference.

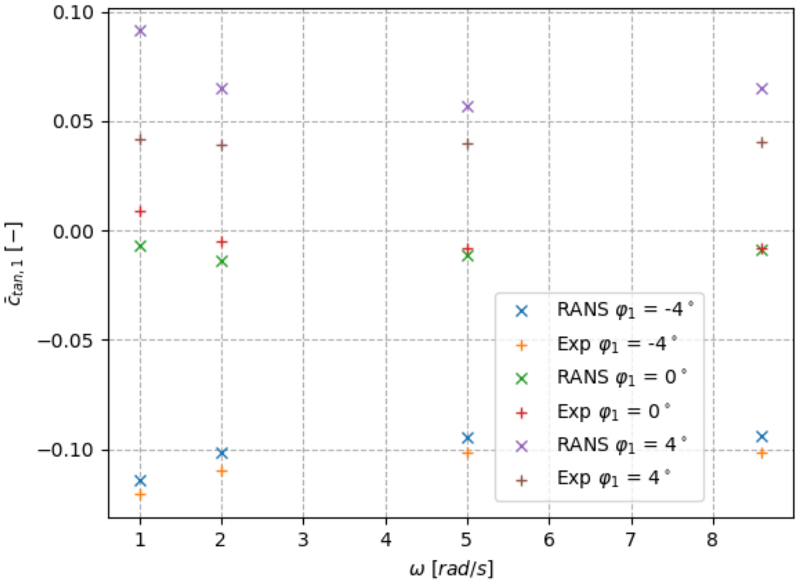

Figure 49: Mean tangential force coefficient of foil No°1 for varying pitch angles over different rotation rates. Values given in experimental frame of reference.

This project has received funding from the European Union's Horizon 2020 research and innovation programme under grant agreement No 851885. This output reflects the views only of the author(s), and the European Union cannot be held responsible for any use which may be made of the information contained therein.

6.1.1.2 *Wave radiation with superposed oscillation*

In these cases, a single foil rotor was rotated at non-constant velocity. For each run, an oscillating angular velocity signal was superposed onto a fundamental motion of constant rotational velocity. This type of testing is often done in rotor applications such as propeller design, since it allows to quantify the influence of added mass and viscous damping on device motion. Herein, the force related to added mass may be determined from the force with oscillated synchronous with device acceleration, whereas the damping force is synced with device motion velocity for the respective degree of freedom. Again, evaluations of forces as well as FFT analysis were applied to a time window of 15 wave periods, in this case referring to the period of the fundamental motion. The first 4 wave periods after $t = 0s$ were not considered in the evaluation. This also applies to the experimental tests, where rotor motion was initialized before $t = 0s$.

The following table shows an overview of all tests conducted using this type of superposed motion. For the sake of brevity, three exemplary cases are analysed here: 170, 173, 150.

Table 9: Overview of cases of wave radiation in calm water with superposed oscillatory angular motion.

Case no	Fundamental frequency [rad/s]	Superposed frequency [rad/s]	Amplitude [°/s]	Pitch angle [°]
149	3.927	2.454	12.272	4
150	3.142	4.241	21.206	4
151	3.142	1.963	9.817	4
152	1.571	0.982	4.909	4
170	3.142	1.963	9.817	-4
173	3.142	1.963	9.817	-8

Case 170

In this test run, the rotor was spun at an angular velocity of $\omega = 3.142 rad/s$, corresponding to a rotational period of 2s and a frequency of $f = 0.5Hz$. The rotational velocity was modulated using a second signal with a period of approximately 3s and an amplitude of 9.8°, meaning that at maximum deflection from the path resulting in constant motion, a difference of 9.8° in rotor position would be obtained. In this case, foil pitch was set to 4°.

The resulting rotor position obtained during these tests was comparatively smooth. This comes at the cost of a more ragged velocity signal, as shown in Figure 48. However, amplitude and frequency of rotation are well matched to the defined values.

This project has received funding from the European Union's Horizon 2020 research and innovation programme under grant agreement No 851885. This output reflects the views only of the author(s), and the European Union cannot be held responsible for any use which may be made of the information contained therein.

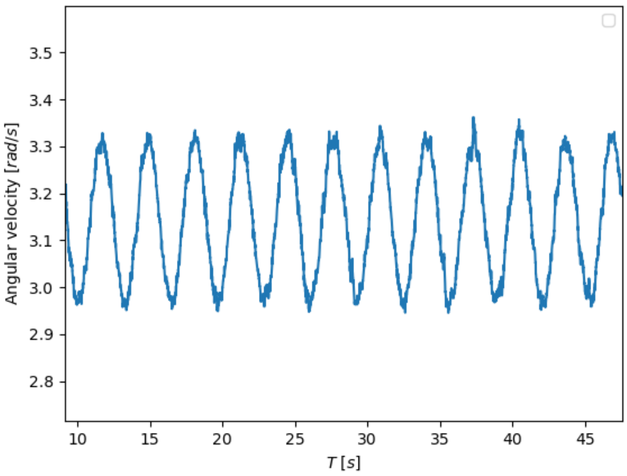

Figure 50: Experimental measurement of angular velocity of single foil rotor in superposed rotational motion in calm water (Case ID 170)

The evaluation of these cases is conducted using a Fast-Fourier Transformations (FFT) of the force time series. This allows to distinguish the foil force responses between fundamental motion velocity, i.e. interaction with the free surface, and the added force signal, for which added mass and viscous damping force oscillate with the acceleration and velocity of the superposed signal.

The time windows of radial and tangential force signal used to conduct the FFT analysis are shown in Figure 48. As can be observed, the mean forces also agree reasonably well. Similar to the constant-velocity wave radiation cases, the forces are subject to strong and chaotic oscillations.

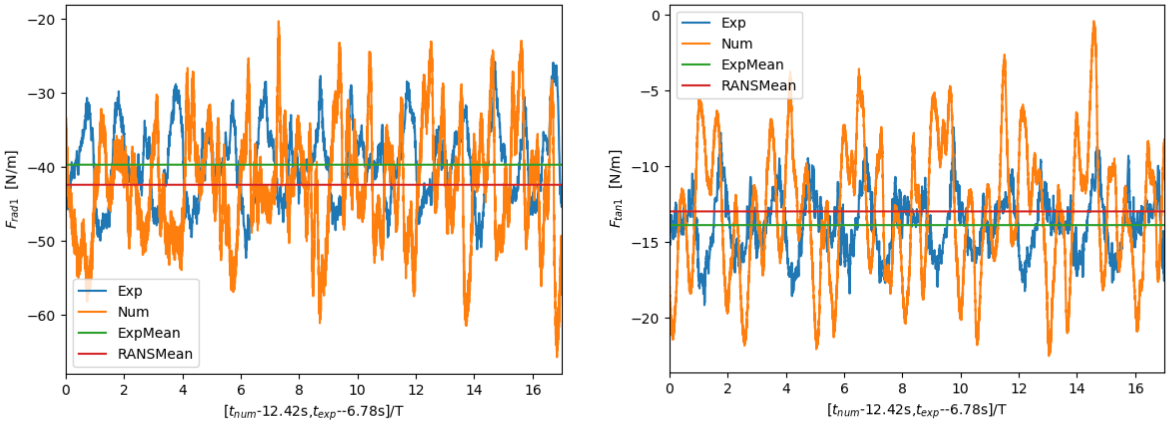

Figure 51: Radial and tangential force per unit span length over time for single foil rotor at non-constant rotational velocity, case 170.

The FFT results for radial and tangential forces as measured during the experiment and computed in the CFD simulation for case 170 are shown in Figure 52 and Figure 53. The fundamental free surface response is visible at $f = 0.5Hz$, while the response of the foil to the superposed motion signal is visible at $f = 0.31Hz$. The radial force results show amplitudes of similar magnitude for fundamental response and the corresponding first order peak ($f = 1Hz$). While the numerically determined value for the fundamental response $f = 0.5Hz$ is slightly lower than the experimental result, one can observe a higher amount of leakage as well as a higher amount of energy for the first order motion response. The radial force response amplitude to the superposed rotation shows a reasonable agreement as well. A similar picture can be found for the tangential force signal.

In both images, the numerical results display distinct peaks at $f = 0.2Hz$ and $f = 0.8Hz$ of similar magnitude for radial and tangential forces. The reason for this is unknown, but might be an error in the correction of hydrostatic forces. The occurrence of these peaks was found for all single-foil superposition simulations but not for simulations at constant rotational velocity or in free motion conditions. Since these did not seem to affect mean forces and since these could not be found in

This project has received funding from the European Union's Horizon 2020 research and innovation programme under grant agreement No 851885. This output reflects the views only of the author(s), and the European Union cannot be held responsible for any use which may be made of the information contained therein.

simulations of constant rotational velocity, including those with external waves, this phenomenon was not further investigated.

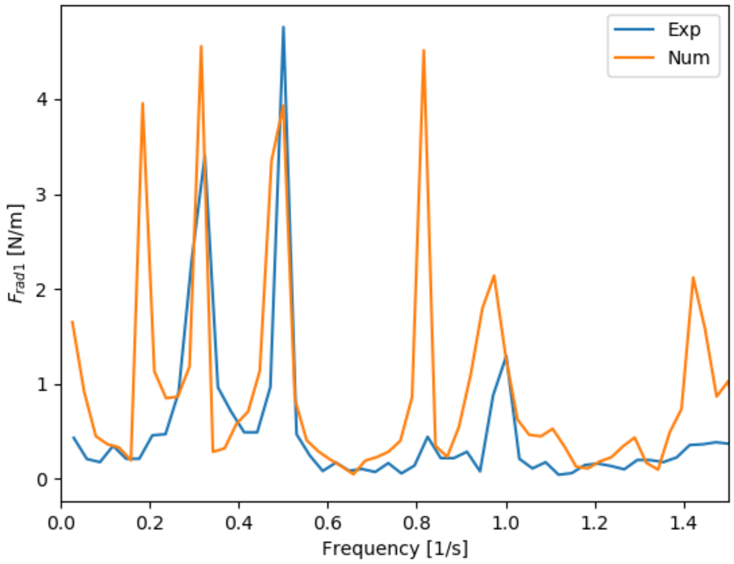

Figure 52: Excerpt of FFT of radial force signal for case 170

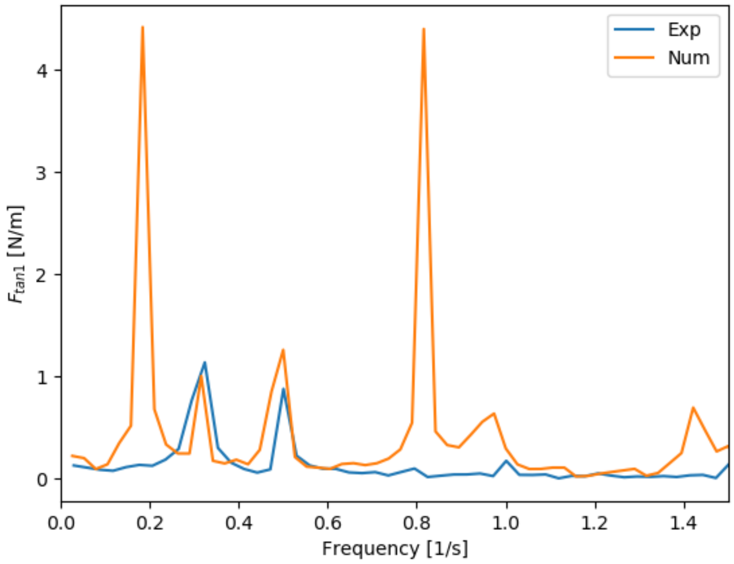

Figure 53: Excerpt of FFT of tangential force signal for case 170

Case 173

The experimental settings applied in case 173 correspond to those used in 170, except for the pitch angle, which has been increased from $\varphi = -4°$ to $\varphi = -8°$.

This project has received funding from the European Union's Horizon 2020 research and innovation programme under grant agreement No 851885. This output reflects the views only of the author(s), and the European Union cannot be held responsible for any use which may be made of the information contained therein.

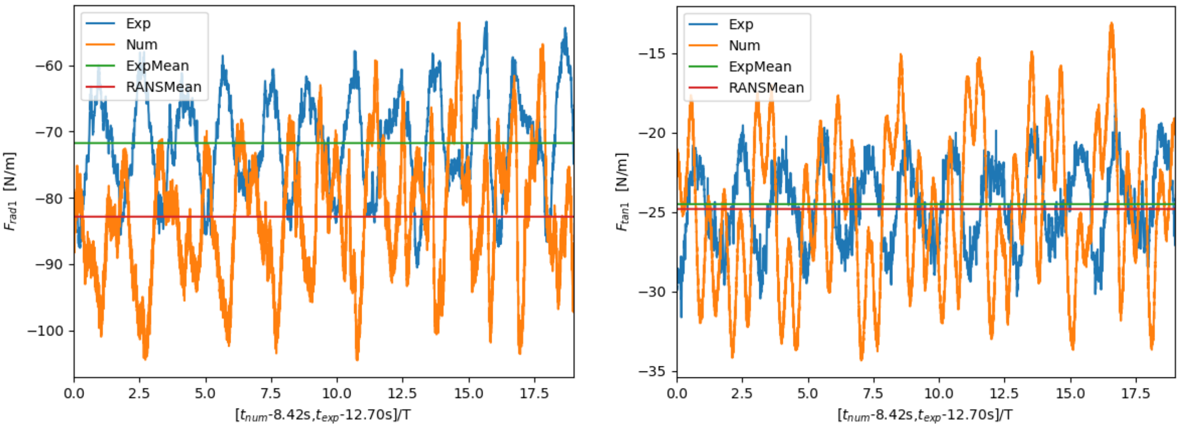

Figure 54: Radial and tangential force per unit span length over time for single foil rotor at non-constant rotational velocity, Case 173.

This results in a duplication of the force amplitude for the superposed motion signal in both radial and tangential direction. The fundamental response due to free surface interaction seems to be of similar magnitude in both cases.

As in the previously discussed case, the discrepancies between the experimental measurement and the numerical simulation results are of acceptable nature when considering the fundamental responses to free surface interaction and superposed oscillation. One further observation is the similarity is the presence of the peaks at $f = 0.2Hz$ and $f = 0.8Hz$. The amplitude of these peaks seems to be identical to the previous case, which might be an indication for the hypothesis that these are a result of an imperfect static lift correction.

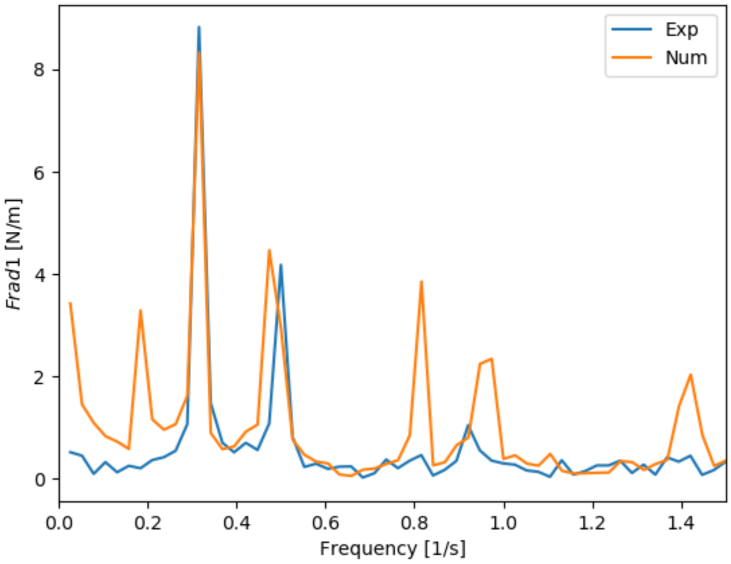

Figure 55: Excerpt of FFT of radial force signal for case 170

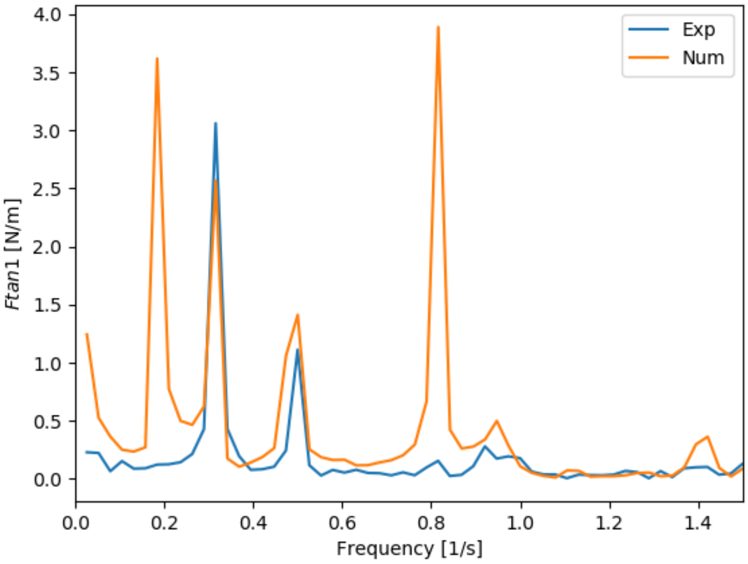

Figure 56: Excerpt of FFT of tangential force signal for case 170

Case 150

The results obtained for case 150 show larger deviations than the previously discussed simulation cases. Figure 57 shows the radial and tangential force signal over time. It can be observed that the mean value of the radial force differs by approximately 20% between numerical and experimental result. A slightly smaller difference is found for the tangential force signal. However, in both images a strong high-frequent oscillation of the experimental force signal is visible.

This may arise due to the higher frequency of the superposed oscillation, which leads to a stronger fluctuation of the velocity signal. This is visible in Figure 58, which shows the angular velocity of the rotor over time. Instead of displaying a smooth sinusoidal shape, the velocity profile shows non-linearities, which likely affect the integral force values.

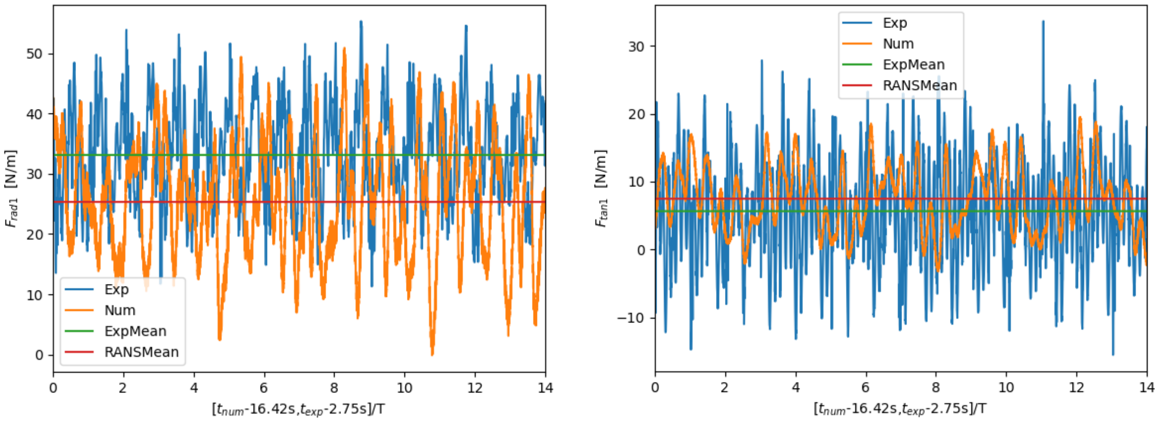

Figure 57: Radial and tangential force per unit span length over time for single foil rotor at non-constant rotational velocity, Case 150.

This project has received funding from the European Union's Horizon 2020 research and innovation programme under grant agreement No 851885. This output reflects the views only of the author(s), and the European Union cannot be held responsible for any use which may be made of the information contained therein.

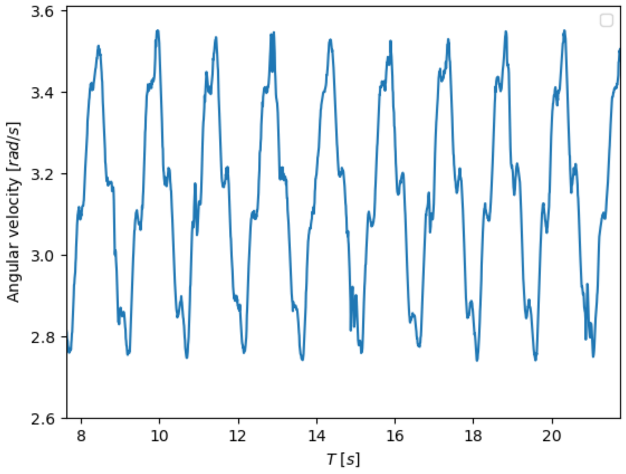

Figure 58: Angular velocity measured during experimental test run 150.

This deviation in velocity may also result in the obtained differences when comparing the FFT-analysis of experimental and numerical force results. The numerically determined force response to the fundamental rotation, at a frequency of $0.5Hz$, has the same magnitude as in previous tests at the same rotation rate. The response measured during the experiment is significantly lower (Figure 59). The response amplitude measured for the superimposed motion ($f = 0.675Hz$) agrees well.

The fundamental rotation response shows a similar behaviour when comparing the tangential force results, with experimental force amplitude being significantly lower than in runs 170 and 173 despite operating at the same rotational velocity (Figure 60). The response to the superimposed motion is larger than predicted by RANS. One possible explanation is again the non-harmonic motion velocity of the rotor, which leads to a large spread of forces when applying an FFT routine. As a consequence, the uncertainty due to post-processing may become significantly larger.

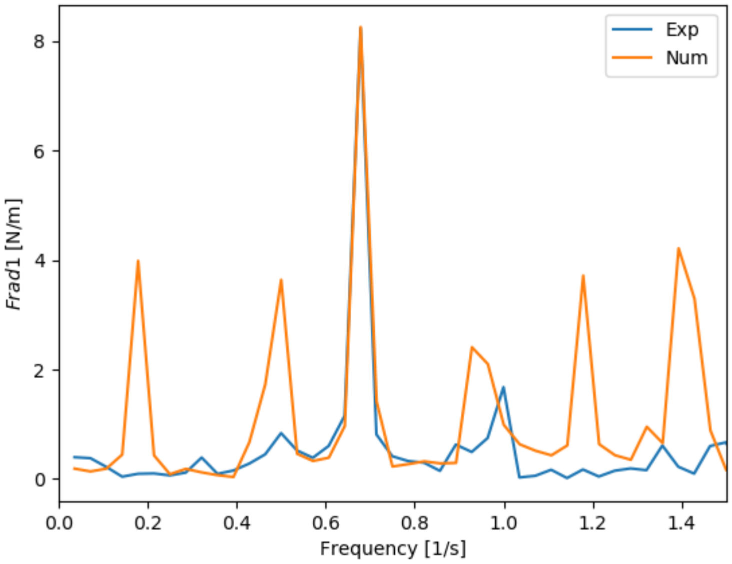

Figure 59: Excerpt of FFT of radial force signal for case 170

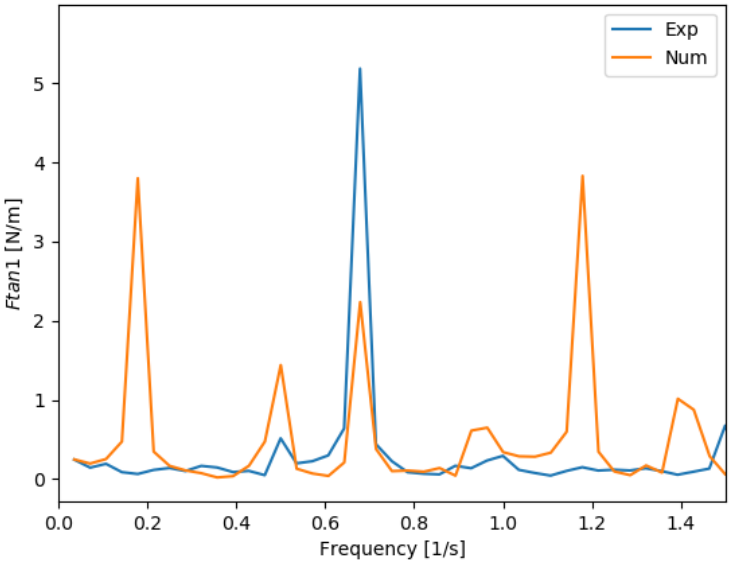

Figure 60: Excerpt of FFT of tangential force signal for case 170

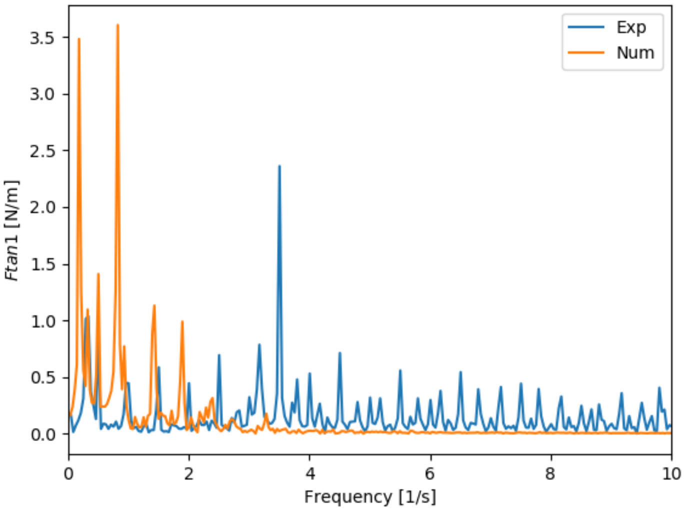

Figure 61: Full FFT of tangential force signal for case 170

This project has received funding from the European Union's Horizon 2020 research and innovation programme under grant agreement No 851885. This output reflects the views only of the author(s), and the European Union cannot be held responsible for any use which may be made of the information contained therein.

6.1.2 Wave radiation of two-foil rotor

In this configuration, a double foil rotor is driven at constant velocity in calm water. The motion of the double-foil rotor causes a deformation of the free surface and thereby a fluctuation of forces. As shown previously, forces are evaluated based on the resulting mean forces in radial and tangential direction, as well as the amplitude of the force at rotation frequency (fundamental response). As in the previous section on single foil rotation in calm water, forces are presented in terms of coefficients, non-dimensionalized using equation (35). This allows to compare the forces over different rotational velocities.

The pitch angle of the foils and the rotation rate of the rotor were varied in between runs. With regard to the pitch angles it should be noted that during each run, the pitch of the two foils is of opposite sign. In all plots of this section pitch angle value is given for foil No°1.

Mean Forces

Foil No°1

The experimentally determined radial force coefficient for foil No°1 shows a nearly constant value across all rotational velocities. The numerically computed values reflect this behaviour for zero-pitch conditions, as is shown in the bottom graph of Figure 62. In all figures referring to mean forces, markers indicate mean values averaged over 15 wave periods, while error bars indicate standard deviation from these mean values.

For a pitch angle of $\varphi = -4°$, the numerical solutions seems to converge to the experimental value for large rotational velocities and deviate for smaller velocities.

This effect may be related to the high relative fluctuation of the force signal, indicated by the error bars shown in the plot. As the mean values are evaluated over a limited number of cycles, the increased presence of vortex structures in the numerical simulations and the corresponding fluctuation of radial forces might lead to a shift of the mean value.

The mean tangential force coefficient (Figure 63) displays a similar behaviour, with nearly constant values across the range of tested angular velocities ω. In this case, the experimentally determined force coefficient for zero-pitch shows a decreasing value with decreasing rotational velocity. As was shown in Table 1, the accuracy of the centrifugal force correction decreases with decreasing rotational velocity. This might be a source of error in this case. One other possible explanation would be an increased coupling with the free surface and hence a stronger wave-induced drag on the foil. This seems unlikely, as the foil-induced circulation at zero-pitch is smaller than at $\varphi = -4°$, where this effect is not visible.

This project has received funding from the European Union's Horizon 2020 research and innovation programme under grant agreement No 851885. This output reflects the views only of the author(s), and the European Union cannot be held responsible for any use which may be made of the information contained therein.

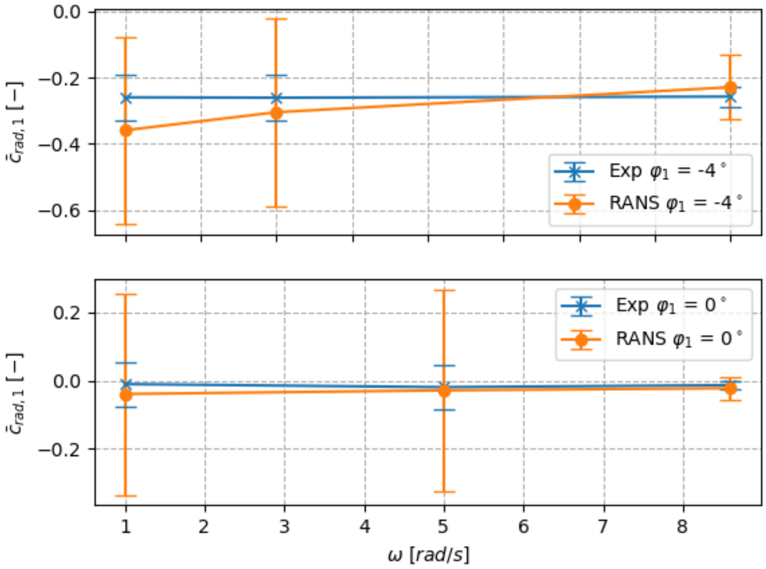

Figure 62: Mean radial force coefficient for foil No°1 in double-foil rotor configuration rotating in calm water over rotation rate for different pitch angles.

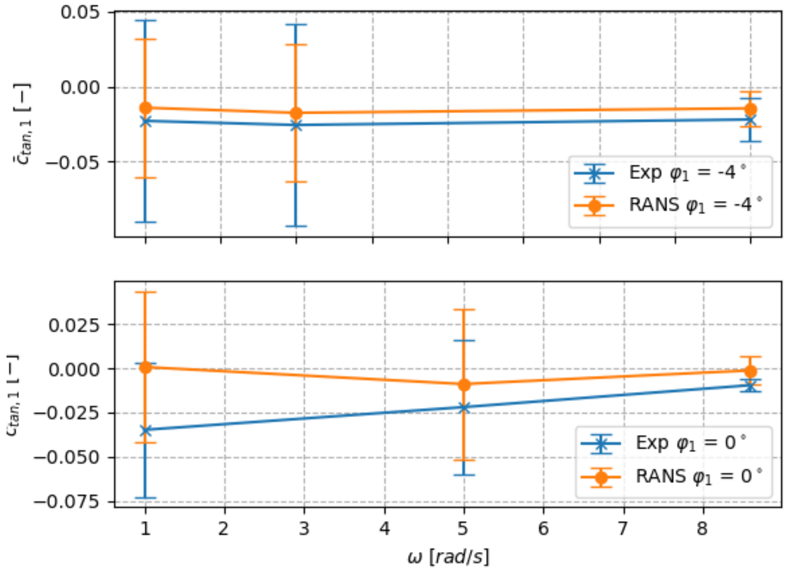

Figure 63: Mean tangential force coefficient for foil No°1 in double-foil rotor configuration rotating in calm water over rotation rate for different pitch angles.

Foil No°2

Similar to foil No°1, the mean radial force measured and computed for foil No°2 agree well over all tested angular velocities and for the two tested pitch angles (Figure 64). The tangential force signal however shows a considerable shift, with numerical forces displaying positive values, indicating that at the centre of the local coordinate system, the foil experiences a driving force (Figure 65).

Despite no external excitation force being present, this is not physically impossible as the rotor torque might still be positive (indicating that rotor is driven by motor) if the local pitch moment is considered. However the reliability of these numerical results still seem insufficient, as the experimental results for the tangential force acting on foil No°1 and foil No°2 show similar values, as might be expected when considering the foil to be symmetric relative to its orbital path and the opposite pitch angles of the two foils.

This deviation roughly corresponds to the order of magnitude of differences between experimental and numerical results found for a single foil in rotation. As indicated in the corresponding section on tangential force results, the shift in forces might indicate either a systematic under prediction of the CFD model or a systematic error in the post-processing. The under prediction of forces in RANS could be due to too low surface roughness height of the model. Another possible explanation for a modelling error would be the full two-dimensional nature of the CFD simulation domain. As was observed during post-processing, this seems to cause vortex structures to be more stable, which could influence turbulence levels causing them to be rather low compared to the experiment. An increase in turbulence could cause a more slender boundary layer shape around the foils, which would lead to an increased velocity gradient in the vicinity of the surface and hence higher friction forces.

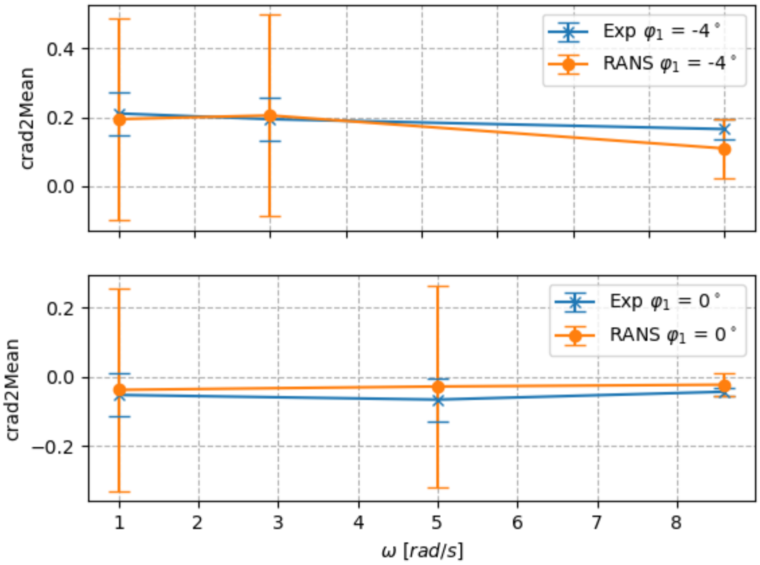

Figure 64: Mean radial force coefficient for foil No°2 in double-foil rotor configuration rotating in calm water over rotation rate for different pitch angles.

This project has received funding from the European Union's Horizon 2020 research and innovation programme under grant agreement No 851885. This output reflects the views only of the author(s), and the European Union cannot be held responsible for any use which may be made of the information contained therein.

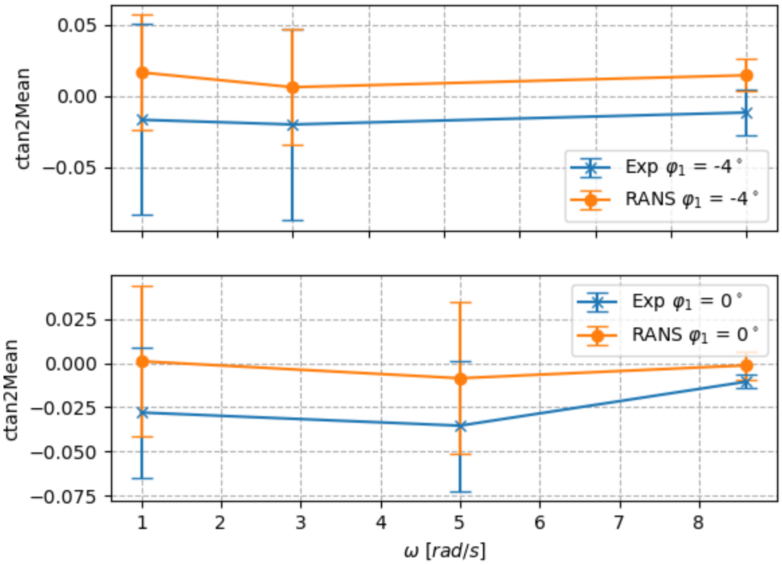

Figure 65: Mean tangential force coefficient for foil No°2 in double-foil rotor configuration rotating in calm water over rotation rate for different pitch angles.

Amplitudes

Foil No°1

The amplitudes considered here refer to the amplitude of both force signals oscillating at rotation frequency as determined by means of an FFT analysis. In all figures referring to force amplitudes, these were evaluated over a time window of 15 wave periods, not considering the initial 10 wave periods of simulation and experiment. Markers indicate amplitude obtained for the fundamental wave frequency, while error bars indicate standard deviation of the force signal from a sinusoidal approximation using wave frequency and mean amplitude.

It can be seen that the amplitudes of the non-dimensional force signals, shown in Figure 66 and Figure 67, converge to zero with increasing velocity. This would be expected given that the main source of force fluctuations is the interaction with the free surface and the hereby induced fluctuations of the inflow angle which may result in shed vortices which affect the hydrofoils during the next cycle.

Free surface interaction corresponds to a wave radiation effect, which is typically proportional to the velocity. With regard to the aspect of vortex shedding, an increased foil velocity will result in smaller relative inflow angles and hence smaller variations of the inflow angle. This will also decrease the relative strength of the vortices which are shed during one motion cycle. As a consequence, the fluctuations will become smaller compared to the mean force, which is proportional to the velocity squared.

The amplitude of the lift force for slow rotational velocities differs significantly between the experimental and numerical results. An explanation for this was provided in section 6.1.1 on the basis that the stronger preservation of vortex structures in the perfectly two-dimensional numerical domain

This project has received funding from the European Union's Horizon 2020 research and innovation programme under grant agreement No 851885. This output reflects the views only of the author(s), and the European Union cannot be held responsible for any use which may be made of the information contained therein.

leads to a strong fluctuation of foil lift when the foil passes these structures during the subsequent cycle.

The amplitude of the tangential force shows rather good agreement for both investigated pitch angles and across the range of tested angular frequencies (Figure 67). This implies that the previously explained foil-free surface coupling and the related wave-induced drag is well reproduced by the numerical model. The sole outlier in this comparison if the tangential force amplitude for $\omega = 1$ and $\varphi = -4°$. The RANS-results indicate an increase in amplitude, which seems reasonable, as the non-zero pitch angle should lead to an increased circulation (also visible in Figure 63), which should also lead to a stronger effect on the free surface. By contrast, the amplitude of induced drag measured during the experiment seems to have decreased for the non-zero pitch angle which seems counter-intuitive. One possible explanation would again be the strong fluctuation of the signal, which renders the FFT procedure rather sensitive to the selection of window start and length, especially with regard to the distribution of energy among the fundamental and first order response frequencies.

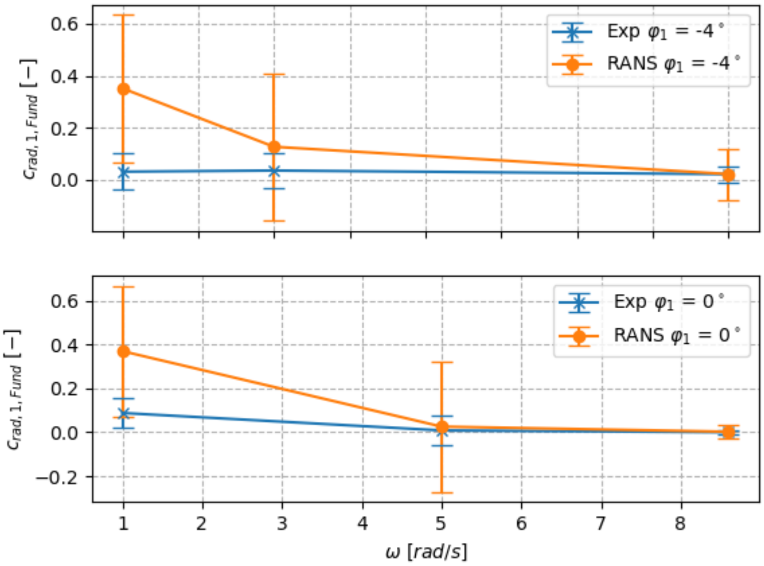

Figure 66: Fundamental amplitude of radial force on foil No°1 of double foil rotor in calm water over rotation rate for different pitch angles

This project has received funding from the European Union's Horizon 2020 research and innovation programme under grant agreement No 851885. This output reflects the views only of the author(s), and the European Union cannot be held responsible for any use which may be made of the information contained therein.

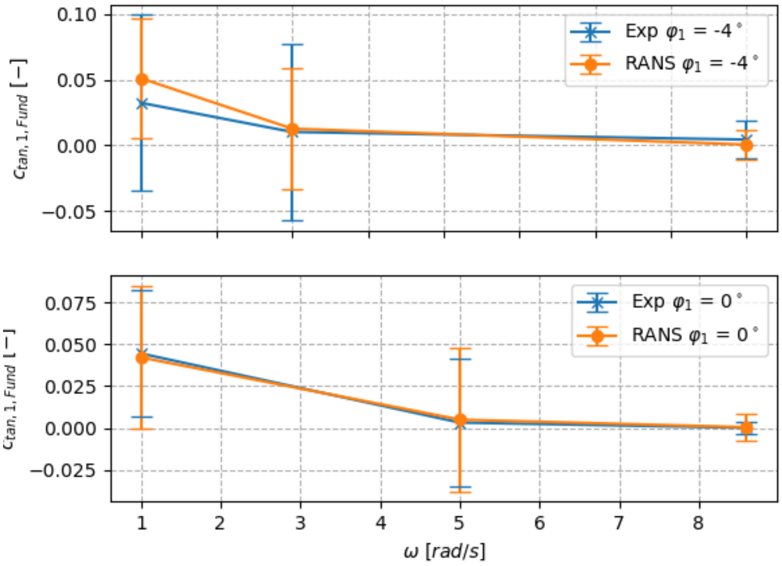

Figure 67: Fundamental amplitude of tangential force on foil No°1 of double foil rotor in calm water over rotation rate for different pitch angles

Foil No°2

The behaviour of mean radial force amplitude of foil No°2 is similar to foil No°1. As shown in Figure 68, the amplitudes decrease with increasing rotation rate, with the effect being significantly more pronounced for the numerical results. The source of this effect has been discussed in section 6.1.1.1.

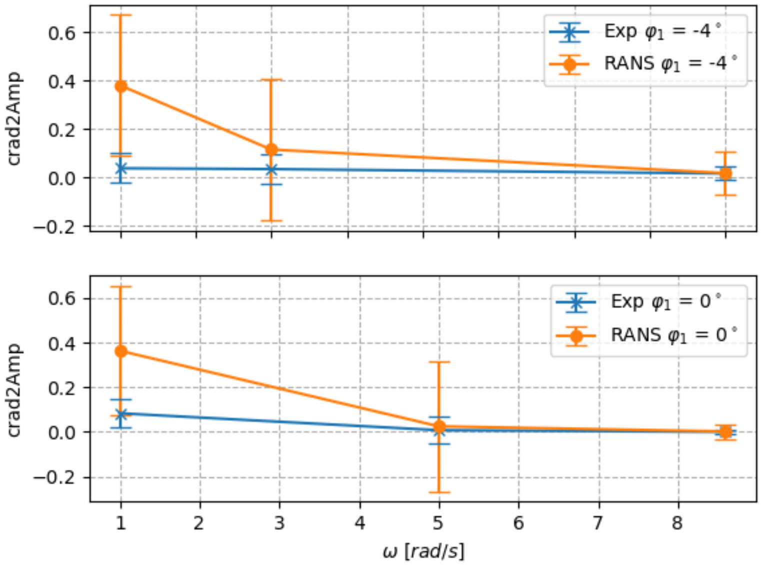

Figure 68: Fundamental amplitude of radial force on foil No°2 of double foil rotor in calm water over rotation rate for different pitch angles

This project has received funding from the European Union's Horizon 2020 research and innovation programme under grant agreement No 851885. This output reflects the views only of the author(s), and the European Union cannot be held responsible for any use which may be made of the information contained therein.

The mean tangential force amplitudes again show rather good agreement, with the exception of the previously discussed outlier at $\omega = 1, \varphi = -4°$. This implies that the added drag due to wave radiation is well captured in these tests.

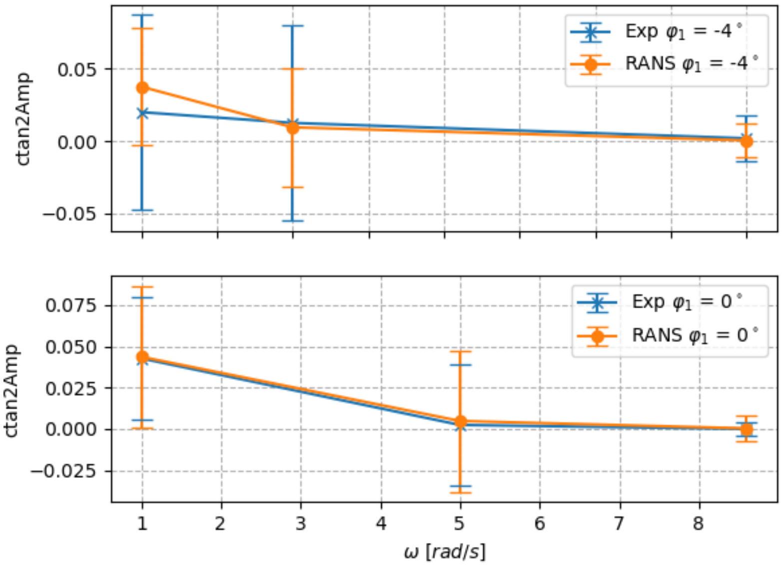

Figure 69: Fundamental amplitude of tangential force on foil No°2 of double foil rotor in calm water over rotation rate for different pitch angles

This project has received funding from the European Union's Horizon 2020 research and innovation programme under grant agreement No 851885. This output reflects the views only of the author(s), and the European Union cannot be held responsible for any use which may be made of the information contained therein.

6.2 EXPERIMENTAL INVESTIGATIONS OF ROTOR IN REGULAR WAVES

In the tests described in this section, the foil is exposed to an incoming regular wave train. Depending on the wave period, the wave height is altered in accordance with the values of waves 13-17 described in Table 2 in section 3.3.

In all cases described in this section, the angular frequency of the rotor and the wave are identical. Variations of the foil forces over time are therefore a result of foil-free surface interaction and wake effects, as shown in the previous section, or due to depth-dependency of wave induced velocities. The phase shift between wave and rotor is 75.5° in all cases presented in this report, referring to the angle between a line connecting pivot point, located at quarter-chord, and centre of rotation, and the z-axis at an instant when the wave crest is located directly above the axis of rotation. This scenario corresponds to an angle of 90° between wave crest and mid-chord position, i.e. the orientation of the struts which hold foil No°1 in position.

As described in section 3.3, the presence of the sub-channel induced wave reflections, starting at an early phase of the test. The result of these reflections is a non-negligible local variation of wave height and wave induced velocity. Due to the complexity of the numerical model, these were not modelled numerically and instead, the target wave height was used, since it represented an acceptable approximation when considering the mean value of wave height across all wave gauges. However, due to the different phase shift between incoming and reflected wave, a shift in mean force is to be expected. This will be discussed in the following.

Results are presented in terms of mean forces, averaged over a window of 15 wave periods and, as in the previous section, fundamental wave amplitudes. First order wave amplitudes are not taken into account, due to the presence of significant wave reflection in the experimental sub-channel region. Due to the direction of rotor rotation, the encounter frequency with these reflected waves is expected to correspond to the first order wave frequency. This leads to strong peaks in the experiment at first order wave frequency which do not occur in the numerical simulation, since the level of wave reflection is significantly lower. Therefore, a comparison of these results is deemed unsuitable for validation purposes.

6.2.1 Single foil rotor in regular waves at 75.5° phase shift

Mean Forces

Figure 70 and Figure 71 shown the mean forces on a single foil rotor blade in radial and tangential direction, averaged over 15 wave periods. Results are provided for 3 different pitch angle settings, over the range of wave frequencies tested. While for a pitch angle of $\varphi = -4°$, only a single experimental test result was available, the a distinct trend can be observed for a pitch angle of $\varphi = 0°$ and $\varphi = 4°$. The radial force coefficient increases in magnitude between $T = 1.6s$ and $T = 2.0s$ and remains at a close-to-constant level then. This effect is well visible for the experimental results, whereas the experimental results are not as consistent, although results seem to agree well in general.

Lift and drag coefficients of lifting bodies are typically firstly a function of angle of attack. The effect observed here reflects the change in angle of attack obtained in different wave conditions. Wave induced velocities are proportional to both wave frequency and wave height. In these tests, changes in wave frequency are met by a corresponding adjustment of rotor frequency, which leads to a compensation of the increase in wave induced velocity. The wave period also has a secondary influence on the induced velocity through its wave number k, with induced velocity being proportional to e^{-kz}, but this effect seems comparatively small. Therefore, the observed trend in induced radial force coefficient can be assigned to the impact of wave height, which is increased between $T = 1.6s$ and $T = 2s$ and then remains constant for higher wave periods. The corresponding trend is also found in the tangential force coefficient results, shown in Figure 71. This indicates, that the wave-induced lift, providing a positive thrust on the foil, is well captured by the numerical method.

The results also show that the variance of forces over time of CFD calculations is significantly smaller than during pure wave radiation cases, while the variance of experimental results has increased. The reduced oscillation of the numerical results is likely due to the wave-induced flow motion in the rotor region, which leads to a stronger dissipation of vortex formations or a convection of these vortices out of the foil path.

The increase in experimental force fluctuation is likely due to the non-homogenous wave climate, resulting as a consequence of the sub-channel induced reflections. The overall increase in mean pitch value for negative pitch angles is due to the larger resulting angle of attack when the leading edge is pitched away from the wave induced incoming velocity.

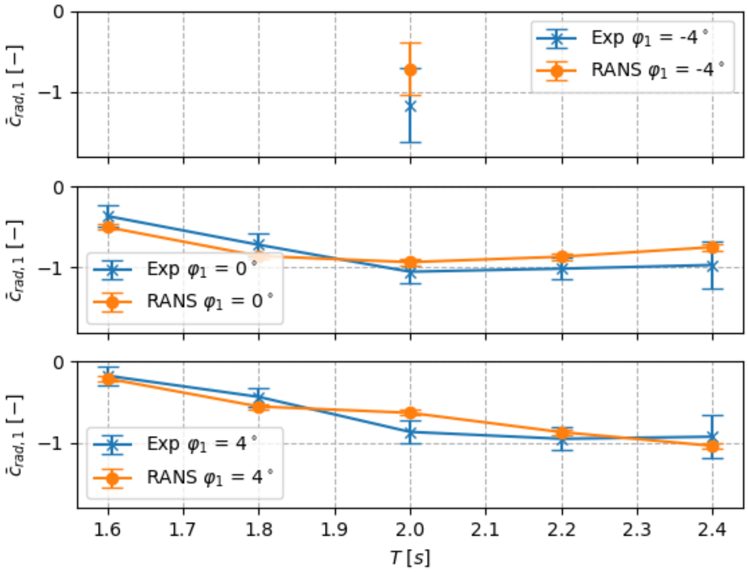

Figure 70: Mean radial force coefficient for foil No°1 in single-foil rotor configuration rotating in regular waves over wave period for different pitch angles.

This project has received funding from the European Union's Horizon 2020 research and innovation programme under grant agreement No 851885. This output reflects the views only of the author(s), and the European Union cannot be held responsible for any use which may be made of the information contained therein.

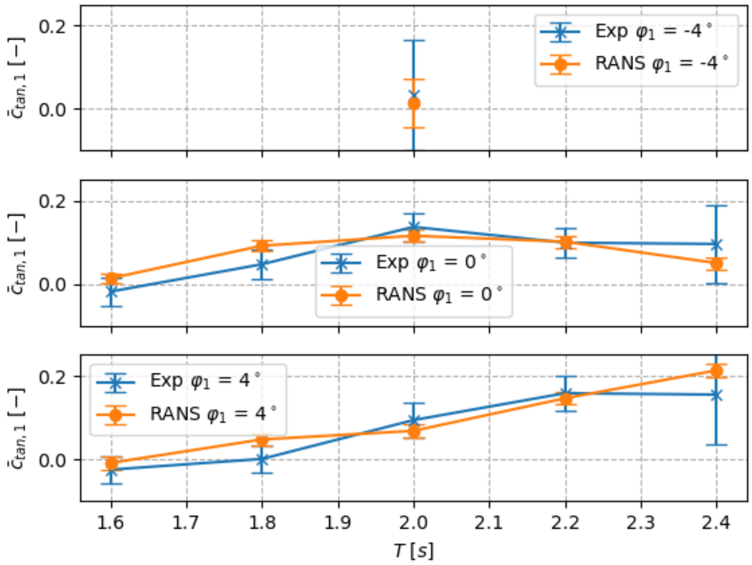

Figure 71: Mean tangential force coefficient for foil No°1 in single-foil rotor configuration rotating in regular waves over wave period for different pitch angles.

Force Amplitudes

Relative to the respective mean radial forces, the force amplitudes of the radial force are comparatively small. For a foil rotating under a monochromatic wave, this would be expected. If depth effects on wave induced velocity were neglected, the resulting force over time should theoretically be a constant value, since rotor-induced and wave induced velocities are always in phase and hence the angle of attack would not change over time.

As can be seen in Figure 72, the amplitudes decrease with increasing pitch angle value. As indicated by the three plots, a negative pitch angle increases overall angle of attack. For an angle of $\varphi = -4°$, first stall effects appear. This results in a strong cyclic fluctuation of radial force.

Overall, the results obtained for the radial force show a reasonable agreement, except for two values of significant deviation which can be observed for zero-pitch and wave periods $T \geq 2.2s$. The reason for this deviation is unclear, but seems to be related to the modelled flow and not to the post-processing. One possible explanation would be an earlier onset of flow separation in the numerical model, which leads to this comparatively large force fluctuation. As can be seen from the result, the experimental error bars, which represent the standard deviation of the force from its mean after subtracting fundamental and first order amplitude, increases considerably for the experiment, while the numerical error interval remains small. This could also be interpreted as an indication that the order of magnitude of fluctuations in both experiment and simulation is similar, but due to too high noise levels, the energy is not assigned to the fundamental wave frequency when post-processing the radial force time series obtained from the experiment.

This project has received funding from the European Union’s Horizon 2020 research and innovation programme under grant agreement No 851885. This output reflects the views only of the author(s), and the European Union cannot be held responsible for any use which may be made of the information contained therein.

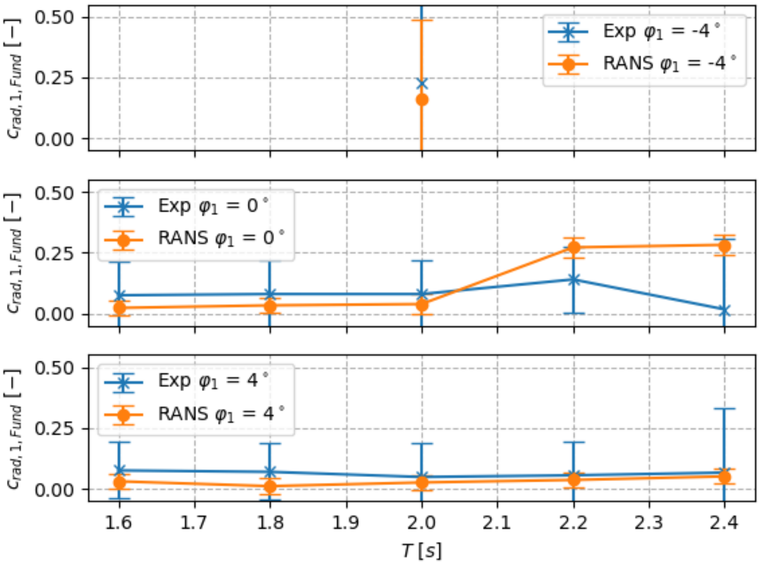

Figure 72: Fundamental radial force amplitude coefficient for foil No°1 in single-foil rotor configuration rotating in regular waves over wave period for different pitch angles.

The fundamental amplitude of the tangential force (Figure 73) shows very good agreement for all tested wave periods for a zero-degree pitch. For a pitch of $\varphi = 4°$, the experimental measurement indicates an increase in fundamental force amplitude for a wave period of $T = 2.0s$ and $T = 2.4s$. For the latter, the increase in amplitude is accompanied by a strong increase in overall force fluctuation. Due to the low angle of attack, which should result for the given monochromatic wave and the positive pitch angle, this increase is unlikely to be the result of flow separation due to foil interaction with the incoming regular wave. However, it may be the result of interaction with the reflected wave. Due to the relatively low rotational velocity of the rotor for this high wave period, the velocity induced by a reflected wave can be expected to show a larger impact on foil forces.

This project has received funding from the European Union's Horizon 2020 research and innovation programme under grant agreement No 851885. This output reflects the views only of the author(s), and the European Union cannot be held responsible for any use which may be made of the information contained therein.

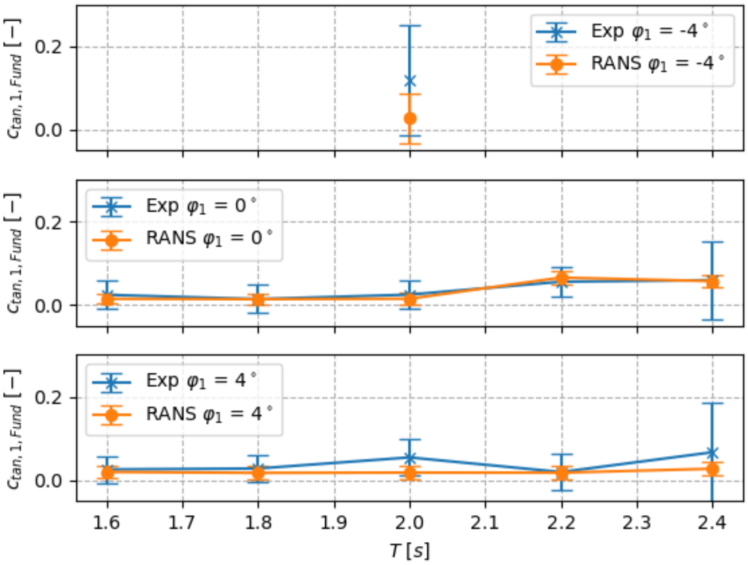

Figure 73: Fundamental tangential force amplitude coefficient for foil No°1 in single-foil rotor configuration rotating in regular waves over wave period for different pitch angles.

6.2.2 Two-foil rotor in regular waves

This study concludes the RANS-based validation part of the 2D experimental study. A rotor with two foils was rotated in regular waves. As in the single foil rotor study, the rotation period was matched with the respective wave period. Experimental and numerical results are again compared using the mean values and fundamental amplitudes of radial and tangential forces measured at quarter-chord position. During this test series, a number of experimental tests were run several times in order to derive an understanding for the repeatability of the measurements. This is indicated by several markers for discrete wave periods in the plots shown in this section.

Mean radial force

Figure 74 and Figure 75 show the mean radial force for foil No°1 and foil No°2. In accordance with the single foil testing and analytical predictions, mean radial forces are highest for a positive pitch angle of $\varphi = 4°$ and lowest for a negative pitch angle of $\varphi = -4°$. Further coherence with theoretical considerations is confirmed by the opposite sign of mean radial force of the two foils. In general, the trend and magnitude of radial forces shows similar results for experimental measurements and numerically predicted forces. Where differences occur, numerical results seem to be lower than the experimental values. Analysis of the time series shows, that several numerically predicted radial forces show a considerable decrease of mean value over the first few wave periods. This is likely due to an acceleration of the flow in the direction of rotor rotation. As discussed in previous sections, the experimental setup is likely to show a stronger decay of induced velocities due to imperfections of the two-dimensionality of the setup. This may be a reason for a reduced impact of flow acceleration on mean force values.

Upon reassessment of single foil test runs in regular waves, a similar trend was found, but significantly less pronounced so that the effect on mean forces was comparatively low.

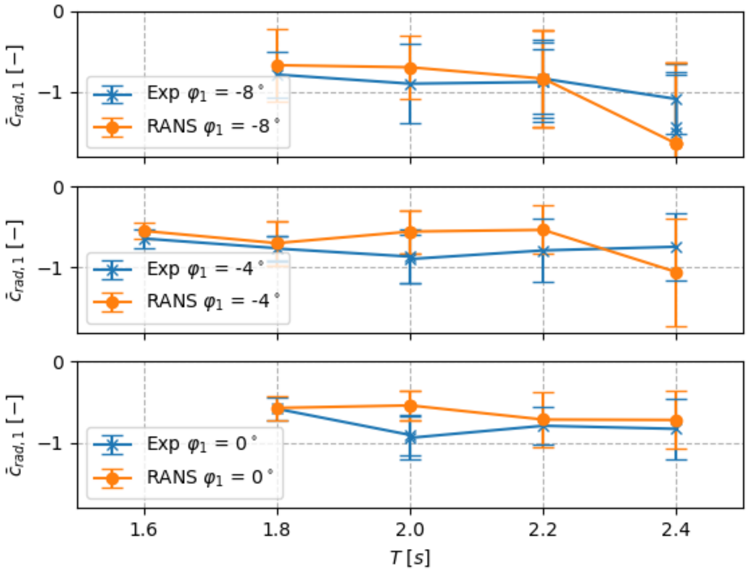

Figure 74: Mean radial force coefficient for foil No°1 in double-foil rotor configuration rotating in regular waves over wave period for different pitch angles.

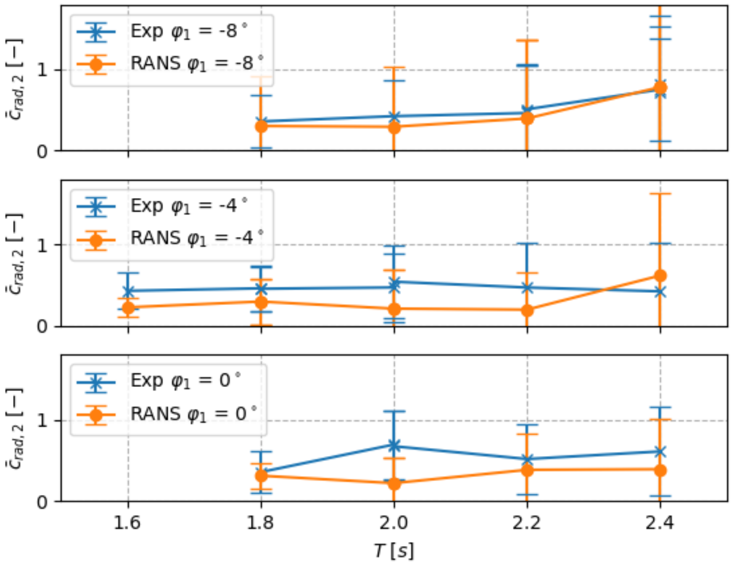

Figure 75: Mean radial force coefficient for foil No°2 in double-foil rotor configuration rotating in regular waves over wave period for different pitch angles.

Mean tangential force

The overall agreement of mean tangential forces is also relatively high (Figure 76, Figure 77). Exceptions are those cases for which the mean radial forces also show decreased agreement, i.e. a

This project has received funding from the European Union's Horizon 2020 research and innovation programme under grant agreement No 851885. This output reflects the views only of the author(s), and the European Union cannot be held responsible for any use which may be made of the information contained therein.

wave period of $T = 2.0s$ and non-zero pitch angles of the hydrofoils. For a pitch angle of $\varphi = -4°$. The agreement of forces is good for foil No°1 and shows slight deviations for foil No°2. For zero-pitch conditions, shown in the last graph of Figure 77, mean force values are similar for foil No°1, but show noticeable differences for foi No°l2, which again corresponds to the observed differences in radial forces.

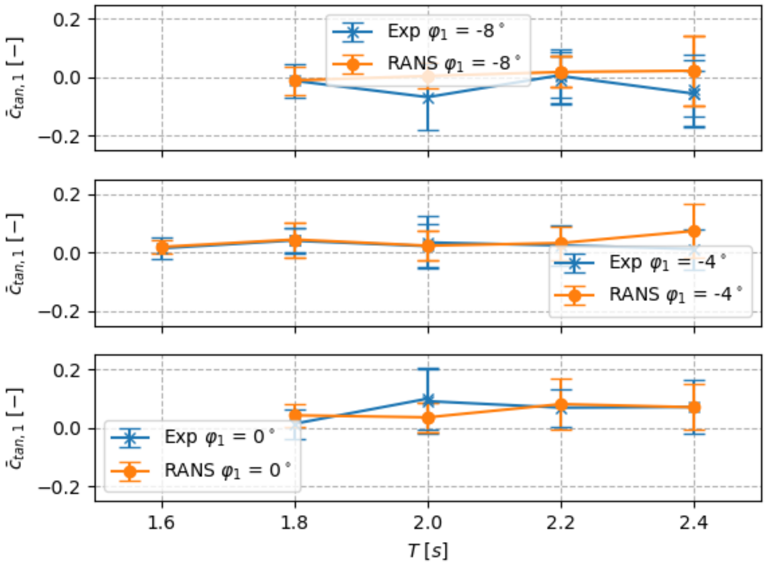

Figure 76: Mean tangential force coefficient for foil No°1 in double-foil rotor configuration rotating in regular waves over wave period for different pitch angles.

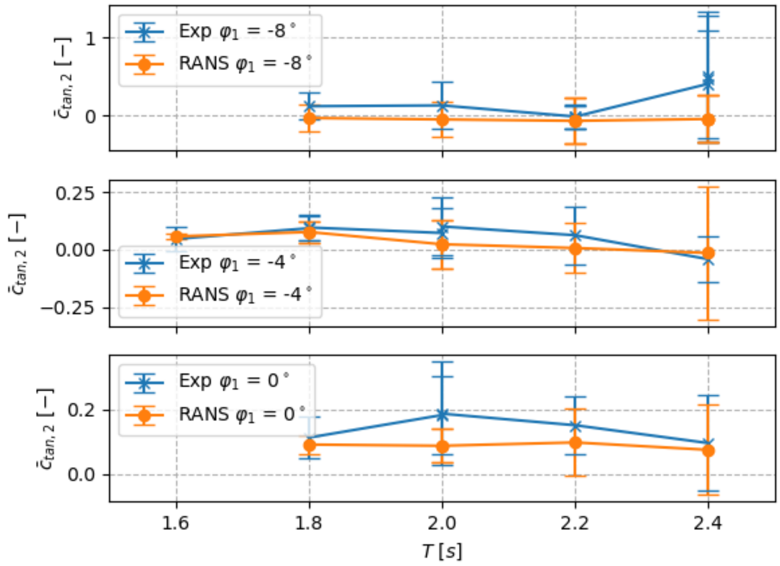

Figure 77: Mean tangential force coefficient for foil No°2 in double-foil rotor configuration rotating in regular waves over wave period for different pitch angles.

This project has received funding from the European Union's Horizon 2020 research and innovation programme under grant agreement No 851885. This output reflects the views only of the author(s), and the European Union cannot be held responsible for any use which may be made of the information contained therein.

Force Amplitudes

Radial Force Amplitude

For short waves periods, the fundamental amplitude of the radial force of foil No°1 shows a similar behaviour when analysing the results of the experiment and the numerical simulation (Figure 78). Largest amplitudes are obtained for a pitch angle of $\varphi_1 = -8°$. Smallest amplitudes are obtained for short wave periods and low pitch angles. As discussed previously, the high rotor velocities in combination with the lower induced velocities at rotor depth results in lower inflow angles and variations of inflow angle on the foil. Significant differences in force amplitude for Foil No°1 are found for a regular wave period of $T = 2.4s$. For a pitch angle of $\varphi_1 = -8°$ and $\varphi_1 = -4°$, these differences are also found for the mean forces, as was discussed previously. For this wave period, a strong increase in force fluctuation is predicted by the numerical simulation for non-zero pitch angles. The experimental results show a rather strong variance of evaluated force amplitudes, as indicated by the blue markers on the top right of Figure 78, where one experiment resulted in an amplitude of $c_{rad,1,Fund} \approx 0.5$ and two test repetitions in an amplitude of $c_{rad,1,Fund} \approx 0.9$.

These differences might indicate an increased uncertainty for this test case. However, the corresponding force results for foil No°2 show rather good agreement and experimental repeatability. One reason for this behaviour could be that at negative pitch angles, the foil trailing edge is more susceptible to flow separation due to the increased relative velocities at this point. In case of flow separation, the forces are rather sensitive to small changes in the flow, increasing the uncertainty at these conditions. This could be an explanation for the good repeatability at large positive pitch angles $\varphi_2 = 8°$ and the large variation of force amplitudes at large negative pitch angles $\varphi_1 = -8°$.

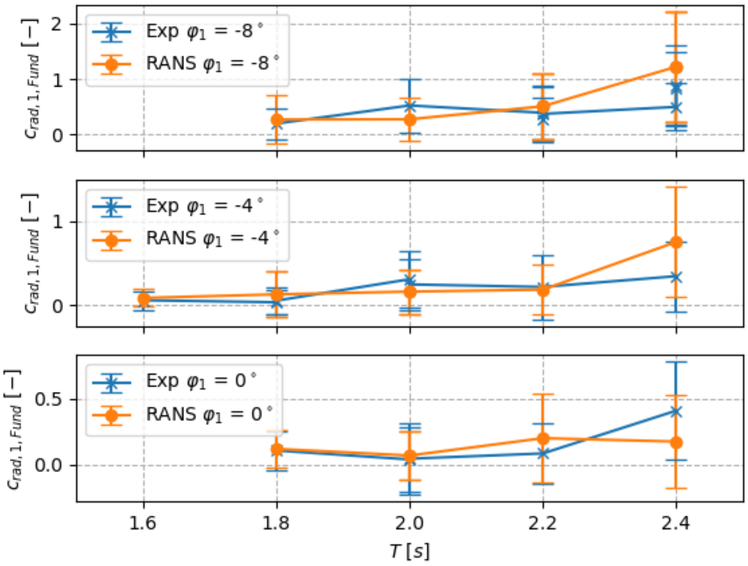

Figure 78: Fundamental radial force amplitude coefficient for foil No°1 in double-foil rotor configuration rotating in regular waves over wave period for different pitch angles.

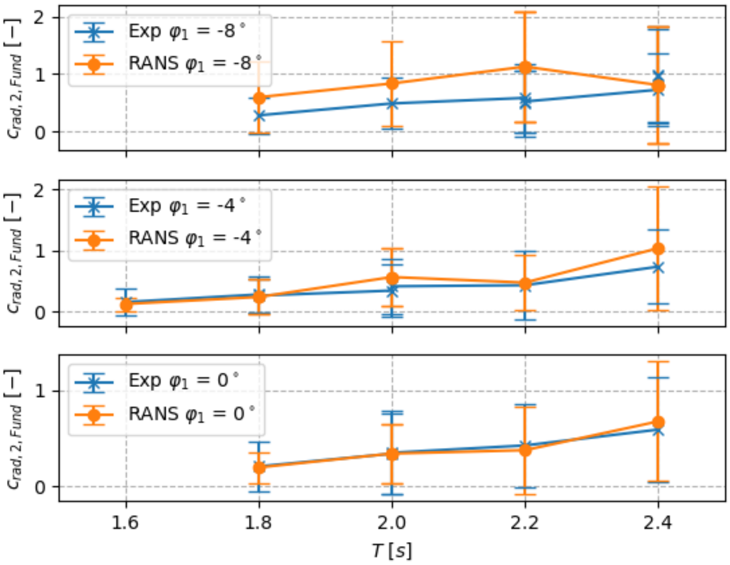

Figure 79: Fundamental radial force amplitude coefficient for foil No°2 in double-foil rotor configuration rotating in regular waves over wave period for different pitch angles

Tangential Force Amplitude

The previously stated hypothesis of an increased uncertainty for large negative pitch angles is supported by the tangential force amplitude results, shown in Figure 80 and Figure 81. While moderate pitch angles of $\varphi_1 = 0°, 4°$ show similar values and trends in fundamental tangential force amplitude, comparatively large differences are found for $\varphi_1 = -8°$. Largest variability both for foil No°1 and foil No°2 is again found for $T = 2.4s$ regular wave, with a fundamental tangential force coefficient amplitude of $c_{tan,2,Fund} \approx 1$ for $\varphi_2 = 8°$. Forces of this magnitude in the direction are deemed improbable from a physical sense due to foil orientation. These results might thus indicate an error in post-processing of the data.

For all regular wave periods $T < 2.4s$, the fundamental force amplitudes of foil No°2 show a good agreement between experiment and numerical simulations. In should be noted that despite the relatively large mean radial forces, which indicate high induced lift and large inflow angles, fundamental amplitudes of tangential forces are of the same order of magnitude as the mean tangential forces. This indicates a reduced applicability of the continuous power extraction, which was deemed to be one of the significant advantages of the cyclorotor concept.

This project has received funding from the European Union's Horizon 2020 research and innovation programme under grant agreement No 851885. This output reflects the views only of the author(s), and the European Union cannot be held responsible for any use which may be made of the information contained therein.

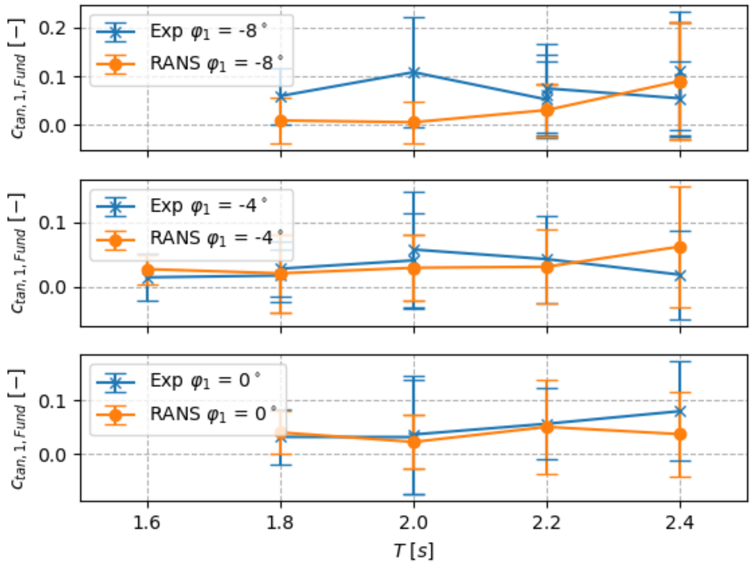

Figure 80: Fundamental tangential force amplitude coefficient for foil No°1 in double-foil rotor configuration rotating in regular waves over wave period for different pitch angles

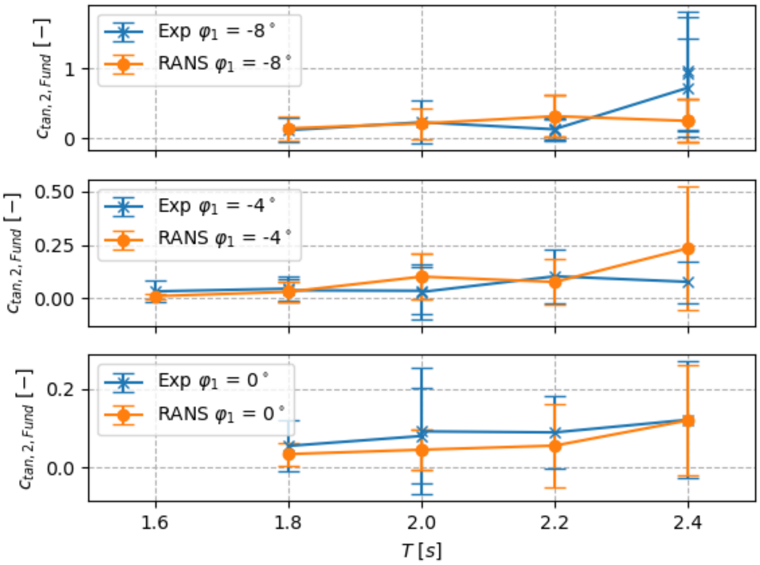

Figure 81: Fundamental tangential force amplitude coefficient for foil No°2 in double-foil rotor configuration rotating in regular waves over wave period for different pitch angles

This project has received funding from the European Union's Horizon 2020 research and innovation programme under grant agreement No 851885. This output reflects the views only of the author(s), and the European Union cannot be held responsible for any use which may be made of the information contained therein.

7 CONCLUSIONS

The presented analysis of the numerical validation study allows us to draw several conclusions regarding current and potential tool performance for design purposes as well as the formulation of several suggestions to further improve the generation of experimental data for validation purposes, which will be presented in the following paragraphs. Overall, it was shown that both tools have the ability to predict the forces acting on a single- or double-foil rotor in calm water and in regular waves.

RANS model

Results generated using the RANS-method have shown reliable predictions of radial and tangential forces for most test scenarios investigated in this study. In calm water tests, deviations of integral values from experimental measurements were typically in the order of $< 10\%$, although a number of outliers were obtained. One central issue for this type of investigation is the susceptibility of the fully two-dimensional consideration to vortex structures in the wake of the foils. Compared to quasi-2D and 3D, these formations show a significantly higher stability, leading to comparatively strong oscillations of the radial forces. Tangential forces seemed to be largely unaffected and indicated a good ability of the method to assess both mean values and oscillation of tangential force induced by free surface interaction.

In monochromatic waves, the influence of vertical wake structures on foil forces was significantly lower than in calm water, likely due to wave-induced convection and dissipation. Here, too, acceptable agreement was achieved for mean values and fundamental amplitudes. Unfortunately, experimental uncertainty for these cases was comparatively high due to wave reflections induced by the presence of the subchannel. One further issue identified for these cases was the increasing acceleration of the flow along with the rotor motion, which led to reduced inflow velocities with increasing simulation time. Both effects are likely to be eliminated in the upcoming 3D test campaign within the LiftWEC project.

Global model

The validation effort of the global model against the tank have demonstrated that the process to numerically reproduce the observed data is not straightforward. The global model relies on the assumptions that at any instant t, it is possible to define and estimate an angle of attack for the foil, and that it is possible to obtain radial and tangential forces acting on the foil from tabulated values of lift and drag coefficients once the AoA and speed of the fluid relative to the foil are estimated.

These assumptions are complicated to validate, as there is no practical means to measure these quantities within the experiment. Attempts have been made in post processing to reconstruct these values from the assessment of the incident and reflected waves and the known position of the rotor, and from there to deduct experimental lift and drag coefficients. These attempts, applied over a series of regular waves of different periods, have shown that the observed lift and drag coefficients do not match the tabulated values available which were used previously. It is also complicated to demonstrate that stable curves are achievable which would be valid for all the experimental conditions. Finally, the experimental conditions do not allow to observe the joint variability of the

This project has received funding from the European Union's Horizon 2020 research and innovation programme under grant agreement No 851885. This output reflects the views only of the author(s), and the European Union cannot be held responsible for any use which may be made of the information contained therein.

coefficients with AoA and Reynolds number. The analysis and determination of the coefficients had to be simplified in that coefficient values are provided independent of the Reynolds number.

Nonetheless, once the coefficients curves derived from the tests are applied to the global model, it was shown that the level of loads estimated on the foil by the global model is in most cases consistent with the experimental measurements. While the model is not able to reproduce wave by wave variation of the forces, the mean levels are comparable and certainly in the right order of magnitude. This level of precision might be sufficient for the estimation of loads on the rotor, and the global model can potentially be used to provide design inputs to the moorings and structural designer. However, the model has not proven yet that it is accurate enough to support the development of the concept from a power production point of view and the assessment of control strategies (submergence, velocity of rotation, pitch angle of the blades).

As described, the results of this validation show that the global model must rely on a set of lift and drag coefficients curves derived from high-fidelity references to achieve some level of accuracy. There are no guarantees as of today that these curves hold true as a function of scale, and/or changes of span of the foils. Therefore, the global model is as of now unable to model with confidence any variation of the rotor (span, profile shape). For any significant variations of the rotor, new coefficients curves would have to be obtain either experimentally or numerically through CFD analysis.

Finally, a separate validation of the global model functionality was completed. The estimation of the loads on a potential cylindrical axis of the rotor in rotation was concluded by comparison of the global model results with the literature. It shows that the current modelling implemented in the global model should be adequate.

Experiment

Despite the novelty of the cyclorotor concept and the limited amount of literature on experimental testing of this type of device, the experimental measurements represented a valuable source of data for validation purposes of the numerical models. A sufficient number of calibration tests has been conducted to develop suitable post-processing routines to remove hydrostatic and centrifugal force effects.

For those cases where this has been tested, good reproducibility of experimental results could be achieved. This indicates that despite the occurrence of wave reflection in the sub-channel, good agreement can be obtained with a suitable model if these reflected waves are modelled. This is supported by the results obtained using the global model, as shown in section 5.1.

However, since this significantly increases efforts with regard to post-processing of experimental and pre-processing of numerical data, is it still desirable to reduce wave reflection in future test campaigns. Reflections as found in most regular wave test cases in this study lead to a shift in mean force values and higher fluctuation of forces, which reduces the informative value of the data with regard to performance under design conditions.

One further finding during validation was the limited meaningfulness of tangential force data when assessing rotor performance. It is recommended to measure foil pitch moment in future tests, whenever it cannot be guaranteed that the measurement point is close to the centre of circulation of the foil, where the moment becomes zero. If this is not possible due to design constraints, shaft torque should be measured. In case measurements are based on shaft torque, a sufficient number of calibration tests should be conducted to assess influence of struts, fairings and other equipment attached to the shaft.

The consistency of experimental and numerical rotor motion is crucial for the purpose of validation. In this study, experimental measurements of rotor position show high precision in all tests. However, due to the strongly fluctuating forces in some cases, this led to strong and high frequent oscillations in rotor velocity and acceleration, which are proportional to radiation and inertial forces. These oscillations reduce the ability to compare force measurement time series and render signal analysis routines such as FFT-based post-processing susceptible to errors. In future tests, it might be advisable for the model tests to include a reliable control function with lower stiffness, which should reduce the impact of force fluctuations on rotor motion.

This project has received funding from the European Union's Horizon 2020 research and innovation programme under grant agreement No 851885. This output reflects the views only of the author(s), and the European Union cannot be held responsible for any use which may be made of the information contained therein.

8 REFERENCES

DNVGL. (2017). *RP-C-205 Environmental conditions and environmental loads*.

Durbin, P. A. (1996). On the k-ε Stagnation Point Anomaly. *International Journal of Heat Fluid Flow*, (17), 89–90. https://doi.org/https://doi.org/10.1016/0142-727X(95)00073-Y

Fenton, J. D. (1985). A fifth-order stokes theory for steady waves. *Journal of Waterway, Port, Coastal and Ocean Engineering*, *111*(2), 216–234. https://doi.org/10.1061/(ASCE)0733-950X(1985)111:2(216)

Ferziger, J. H., & Peric, M. (2002). *Computational Methods for Fluid Dynamics* (3rd ed.). Springer.

Hadzic, H. (2005). *Development and application of Finite Volume Method for the Computation of Flows Around Moving Bodies on Unstructured, Overlapping Grids*. Hamburg University of Technology.

Hirt, C. W., & Nichols, B. D. (1981). Volume of fluid (VOF) method for the dynamics of free boundaries. *Journal of Computational Physics*. https://doi.org/10.1016/0021-9991(81)90145-5

Larsen, B. E., & Fuhrman, D. R. (2018). On the over-production of turbulence beneath surface waves in Reynolds-averaged Navier-Stokes models. *Journal of Fluid Mechanics*, *853*, 419–460. https://doi.org/10.1017/jfm.2018.577

Menter, F. R. (1994). Two-Equation Eddy-Viscosity Turbulence Models for Engineering Applications. *AIAA Journal*, *32*, 1598–1605.

Morison, J. R., Johnson, J. W., & Schaaf, S. A. (1950). The force exerted by surface waves on piles. *Journal of Petroleum Technology*, (2 (05)), 149–154.

Ogilvie, F. O. (1963). *First and second-order forces on a cylinder submerged under a free surface*.

Orcina. (n.d.). OrcaFlex manual. Environment: Data for time history waves. Retrieved from https://www.orcina.com/webhelp/OrcaFlex/Content/html/Environment,Datafortimehistorywaves.htm

Perić, R., & Abdel-Maksoud, M. (2016). Reliable damping of free-surface waves in numerical simulations. *Ship Technology Research*, *63*(1), 1–13. https://doi.org/10.1080/09377255.2015.1119921

Sheldahl, R. E., & Klimas, P. C. (1981). *Aerodynamic characteristics of seven symmetrical airfoil sections through 180-degree angle of attack for use in aerodynamic analysis of vertical axis wind turbines.* Albuquerque, New Mexico, United States of America.

Siemens PLM Software. (2016). *Star-CCM+ 14.06 User Manual*. Granite Parkway: Elsevier Ltd.

Wilcox, D. C. (2006). *Turbulence Modeling for CFD* (3rd ed.). La Canada CA: DCW Industries.

This project has received funding from the European Union's Horizon 2020 research and innovation programme under grant agreement No 851885. This output reflects the views only of the author(s), and the European Union cannot be held responsible for any use which may be made of the information contained therein.